Developing a global fluid-structure interaction model of the aortic root

Hossein Mohammadi
Department of Mechanical Engineering
McGill University
Montreal, Québec, Canada

A thesis submitted to McGill University in partial fulfillment of the requirements of the degree of Doctor of philosophy

Abstract

According to statistics released by the Public Health Agency of Canada, circulatory system disease accounted for one-third of all deaths in Canada (71,749 deaths) in 2005. It remains the leading cause of hospitalization in the country, accounting for 14 per cent of the total. In Canada, the total costs for three types of circulatory disease (coronary heart disease, stroke, and hypertensive heart disease) were estimated to be $21 billion in 2005. Since more than 80 percent of circulatory system deaths in Canada and high income countries are due to diseases of the aortic valve, coronary arteries and the blood vessels supplying the brain, greater attention should be put on the function of the aortic root and its adjacent structures. The decline in the mortality rate associated with the circulatory system diseases is attributed to medical and engineering advances to develop new diagnostic and prognostic tools using in-vivo, in-vitro and numerical studies. However, as the numerical methods are less expensive and more flexible in applying geometrical and hemodynamic variations, they have gained considerable attention in assessing the hemodynamic conditions associated with cardiovascular diseases.

In recent clinical studies, it was established that regional pathologies of the aortic valve can alter the structural and hemodynamic function of the valve and coronary arteries. However, due to limitations either with medical imaging modalities or numerical simulation, the impact of hemodynamic effects is not yet fully elucidated for disease initiation and progression. Numerous clinical and numerical studies are done on the aortic root and the coronary arteries individually. However, only a limited number of them have incorporated both these adjacent structures into one numerical global model. Due to the large deformations that leaflets experience during the cardiac cycle, numerical modeling of fluid–structure interaction of the aortic valve has proven to be a challenging task. Adding the coronary arteries to the aortic valve model increases this complexity which constitutes the limitation of previous studies and all of the developed models so far have either ignored the natural aortic root structure by using simplified geometry of the valve or the coronary vessels or neglected the interaction between the fluid and solid domains. The objectives of these studies were: to reproduce the valve dynamics to study alteration to geometrical and hemodynamic parameters and derive the stress patterns. A few studies have been done for making these engineering results meaningful for physicians in terms of disease prognostic tools. The main goal of this study is to address this particular aspect.

Hypothesis

It is possible to develop a global model of the aortic valve region with inclusion of the coronary vessels and the aorta to derive a global index to assess the regional hemodynamic conditions in the aortic root based on surrogate variables and investigate the possible interaction between coronary artery pathologies and aortic valve pathologies.

Objectives

The main objective of this study is to develop a 3D global fluid-structure interaction of the aortic root with inclusion of anatomically inspired coronary vessels and their critical small branches as well as the aorta using finite element method. This model is served in derivation of surrogate indices and explaining the possible interactions between the regional pathologies and global variations in the structure as well as providing a better insight into the hemodynamic of coronary multi vessel lesions the and hemodynamic of the aortic valve region as well as the coronary arteries. Eventually, the model could potentially be used in the clinical setting as a diagnostic tool to guide the cardiac surgeons and cardiologist by providing data in terms of disease prognostic tools including the anatomical and hemodynamic data called surrogate variables.

Résumé

Selon les statistiques publiées par l'Agence de santé publique du Canada, les maladies du système circulatoire représentaient un tiers de tous les décès au Canada (71 749 décès) en 2005. Au Canada, les coûts totaux pour les maladies du système circulatoire (maladie coronarienne, d'AVC et la cardiopathie hypertensive) ont été estimés à 21 milliards en 2005. Depuis, plus de 80 pour cent des décès système circulatoire au Canada et dans les pays à revenu élevé sont dus à des maladies de la valve aortique, artères coronaires et vaisseaux sanguins qui alimentent le cerveau, plus de recherche sur ces régions du système cardio-vasculaire est nécessaire. La baisse du taux de mortalité associeé aux maladies du système circulatoire est attribuée à l'ingénierie médicale et aux développement de nouveaux outils diagnostiques et pronostiques utilisant des données in vivo, in vitro et des études numériques. Cependant, comme les méthodes numériques sont moins couteuses chers et plus souples pour l'utilisation de plus de variations géométriques et hémodynamiques, ils ont gagné une attention considérable dans l'évaluation des conditions hémodynamiques associées aux maladies cardio-vasculaires.

Dans des études cliniques récentes, il a été établi que les pathologies régionales de la valve aortique peuvent altérer la fonction hémodynamique et structurelle et de la valve et des artères coronaires. Toutefois, en raison des limitations soit avec les modalités d'imagerie médicale ou la simulation numérique, l'impact des effets hémodynamiques n'est pas encore complètement élucidé pour l'initiation et la progression de la maladie. De nombreuses études cliniques et numériques ont été effectuées pour la racine de l'aorte et des artères coronaires. Toutefois, seul un nombre limité d'entre eux ont intégré ces deux structures adjacentes dans un seul modèle global numérique. En raison des grandes déformations que les feuillets expériencent pendant le cycle cardiaque, la modélisation numérique des interactions fluide-structure de la valve aortique s'est avéré être une tâche difficile. L'ajout des artères coronaires au modèle de la valve aortique augmente cette complexité ce qui constitue une limitation des études antérieures et tous les modèles développés jusqu'à présent ont soit ignoré la structure de la racine aortique naturelle à l'aide de la géométrie simplifiée de la vanne ou les vaisseaux coronaires ou négligé l'interaction entre les domaines fluide et solide. Les objectifs de ces études étaient les suivants: reproduire la dynamique de la valve soupape pour étudier la modification des paramètres géométriques et hémodynamiques et d'en tirer les causes de stress. Quelques études ont été faites pour rendre ces résultats d'ingénierie

significatifs pour les médecins en termes des outils pronostiques. L'objectif principal de cette étude est de répondre à cet aspect particulier.

Hypothèse

Il est possible de développer un modèle global de la région de la valve aortique avec inclusion des vaisseaux coronaires et de l'aorte et obtenir un indice global pour évaluer les conditions hémodynamiques régionaux dans la racine de l'aorte en fonction des variables de remplacement et d'enquêter sur l'interaction possible entre les pathologies coronariennes et pathologies de la valve.

Objectifs

L'objectif principal de cette étude est de développer un modèle d'interaction fluide-structure 3D globale de la racine aortique avec inclusion des vaisseaux coronaires anatomiquement inspirés et de leurs petites branches critiques ainsi que l'aorte en utilisant la méthode des éléments finis. Ce modèle est utilisé pour la dérivation des indices de remplacement et d'expliquer les interactions possibles entre les pathologies et les variations globales de la structure ainsi que de fournir une meilleure description de l'hémodynamique des vaisseaux coronariens les lésions hémodynamiques et de la région de la valve aortique ainsi que les artères coronaires.

Acknowledgments

I would like to first thank my supervisor, Professor Rosaire Mongrain, for his continuous guidance, immense knowledge and positive research attitude provided to me during the course of the research involved in this thesis. This project would have never been accomplished without his supports and invaluable advices.

I would also like to thank Dr.Raymond Cartier and my advisory committee members for their useful insight and suggestions during the Ph.D. meetings. I would like to acknowledge the financial support from McGill University, through the McGill Engineering Doctoral Award (MEDA). Natural Sciences and Engineering Research Council of Canada (NSERC) and Montreal Heart Institute (MHI) are acknowledged for providing funding for this research work.

This work was made possible by the facilities of the Shared Hierarchical Academic Research Computing Network (SHARCNET: www.sharcnet.ca) and Compute/Calcul Canada. Administrative and technical support from staff in Mechanical Engineering office, especially from Joyce Nault, Mary Fiorilli, and Kevin Mitchell is greatly appreciated. I would like to thank my friends and colleagues for their unsparing collaboration and invaluable input throughout these years

Special thanks goes to my parents, brother and sisters. They were always encouraging me with their best wishes. I am eternally grateful to my loving parents for their incredible support, endless love, and patience throughout my life. They have truly made the sacrifices on my behalf which I would never be able to pay back.

Table of Contents

List of Figures

List of Tables

Chapter 1: Introduction

In this chapter, the clinical aspect of the aortic valve, coronary arteries and the aorta morphology, physiology and functionality is presented. The most prevalent pathologies of these regions as well as the clinical indices for assessing them is discussed. Following this section, in order to provide a tool for understanding and finding a solution to the clinical pathologies, engineering background including different numerical methods used in modeling the main components of the circulatory system is presented.

1.1 Clinical background

1.1.1 The Circulatory system

The heart is a two-sided pump composed of four chambers: the upper two chambers called atria and the lower two called the ventricles (Figure 1.1). The right side of the heart is separated from the left side by the septum. In order to overcome the pressures existing in the two circuits and pump the blood out for circulation; the ventricles must generate enough force. Hence, they are more muscular than atria. Similarly, because the pressure in the systemic circuit is higher than the pulmonary circuit, and also the traveled distance by blood in the systemic circulation is longer (higher resistance), the muscular walls of the left ventricle are thicker than those of the right ventricle.

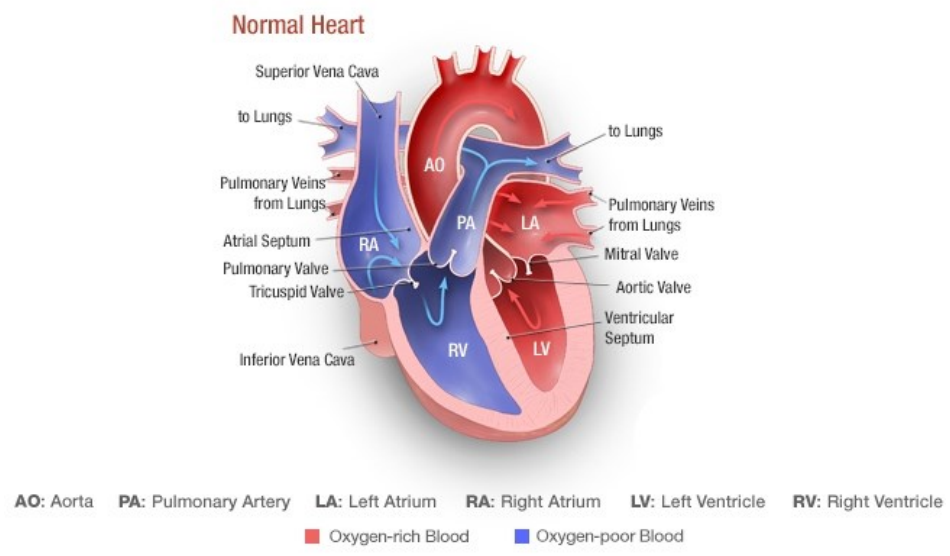

Figure 1.1: The basic anatomy of the human heart including the chambers, the attached major blood vessels, and the two types of heart valves [adapted from CHOP (downloaded April 2014)].

To prevent blood from flowing in the wrong direction, unidirectional valves are located at the inlet and outlet of each ventricle. Each valve is composed of flaps to allow forward flow of blood in opening and to prevent backward flow by closing. The atrioventricular valves (AV) including the tricuspid valve and mitral valve separate the right and left atria from their corresponding ventricles, respectively. Semilunar valves including the pulmonary valves and the aortic valve are positioned at the outlet of right and left ventricles, respectively, where the blood leaves the heart into circulation. These valves and their proximity to each other are represented in Figure 1.2.

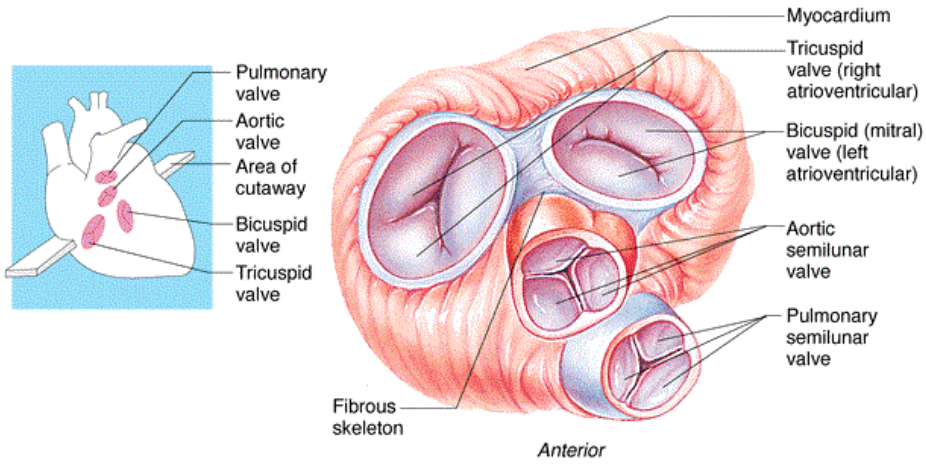

Figure 1.2: Schematic diagram illustrating the four valves of the heart and their orientation within the heart [adapted from benjamin cummings (downloaded April 2014)]

The heart is the central component of the human circulatory system that pumps blood throughout the body due to periodic stimulation and contraction of its muscles. The circulatory system is composed of a closed network of vessels arteries, veins, and capillaries. To supply all of the body's tissues with the blood, the heart pumps oxygen and nutrient-rich blood around the network of vessels through two separate circuits: The pulmonary circuit and the systemic circuit.

In the pulmonary circuit, the returned blood from the body through the superior and inferior vena cava flows into the right atrium then by passing the tricuspid valve it enters the right ventricle then is pumped into the pulmonary artery and the lung to exchange carbon dioxide in the blood with oxygen from the lungs. Then, the freshly oxygenated blood flows from the pulmonary veins into the left atrium, and through the mitral valve into the left ventricle, whose contraction ejects the blood into the aorta to be delivered to all organs and cells through the systemic circuit. In both circuits, the blood passes through a network of blood vessels. It is pumped out of the heart into

large muscular arteries branching into smaller arteries, then arterioles, followed by complex networks of small capillaries. The exchange between the blood and nearby cells happens in the capillaries. After leaving the capillaries, the blood is collected into venules and then veins of increasing size, before being returned to the heart. In both systems, take blood is took away the heart by arteries and is brought toward the heart by veins [1]. A schematic representing these two circulations is shown in Figure 1.3.

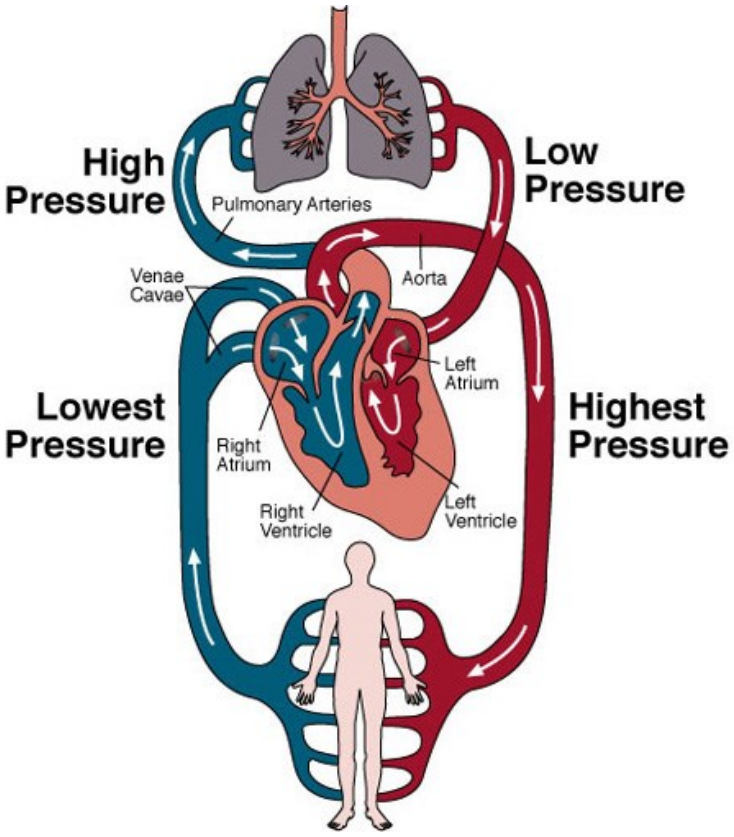

Figure 1.3: An overview of the circulatory system in the human body [©2014, WebMD, LLC. All rights reserved]

As discussed previously, Circulatory system diseases are the leading causes of hospitalization in Canada accounting for one-third of all deaths in Canada (71,749 deaths) in 2005. There are many types of circulatory diseases. But More than 80 percent of circulatory system deaths in Canada are due to diseases of the aortic valve coronary arteries and the blood vessels supplying the brain [3]. Hence, the main focus in the following sections will be on parts of the circulatory system which are affected by those diseases.

1.1.2 The natural aortic valve

1.1.2.a Morphology

The aortic valve situated at the outlet of the left ventricle just prior to the ascending. This valve has a complex structure with three relatively equal-sized crescent-shaped cusps known as leaflets. The leaflets are the most mobile parts of the valve. In the open position, they are displaced outward toward the aorta while, in the closed position the leaflets come together to seal the aortic orifice and withstand pressure differentials (up to 120mmHg). The anatomical geometry of the leaflets is presented in Figure 1.4. The supporting structure for the aortic valve is known as the aortic root which forms a connection between the left ventricle and the aorta.

The cavities behind the leaflets are called the sinuses of Valsalva, which have a bulbous shape. The coronary arteries, that provide blood flow to the heart itself, branch off the aorta and their blood inlets are located into two of these sinuses. The right coronary artery exits the right sinus, the left coronary artery exits the left sinus, and the third sinus is known as the non-coronary sinus. The configuration of the normal aortic sinuses including the LCC (Left coronary cusp), RCC (Right coronary cusp) and the NCC (Non-coronary cusp) and valve is shown in Figure 1.4.

Some other anatomical structures are the commissures, sino-tubular junction and the aortic root. The commissures refer to the part of the attachment between the leaflets and the wall adjacent to the leaflets. The sinuses meet the ascending aorta in a portion of the valve called the sino-tubular junction (Figure 1.5). The aortic root is the entire region that begins at the bottom of the sinuses and ends at the Sino-tubular junction.

The term “aortic valve” refers to the part of the aortic root consisting of the leaflets and the sinus walls, bounded by the left ventricle out flow tract on ventricular side and the aortic ring at the aortic side (Figure 1.5) [2].

Each leaflet has two functional areas. The area near the free edge is known as the coaptive area that is also called the lunulea due to its semilunar shape. During the closure phase of the valve they come in contact with each other and create the necessary sealing. The remaining, non-coaptive area of the leaflet surface has a belly shape that is known as the load bearing portion. As the aortic valve opens and closes, the valve leaflets undergo very large displacements under physiological loads in each cardiac cycle. The structure and the elastic properties of the leaflets play a key role in their ability to work during such a large amount of flexion associated with opening and closing of the leaflets. The aortic valve leaflet structure is composed of three layers known as ventricularis,

spongiosa, and fibrosa. These layers are primarily composed of collagen, elastin, and a glycosaminoglycan-rich ground substance but to create proper mechanical properties, the amount and orientation of these components are different at each layer.

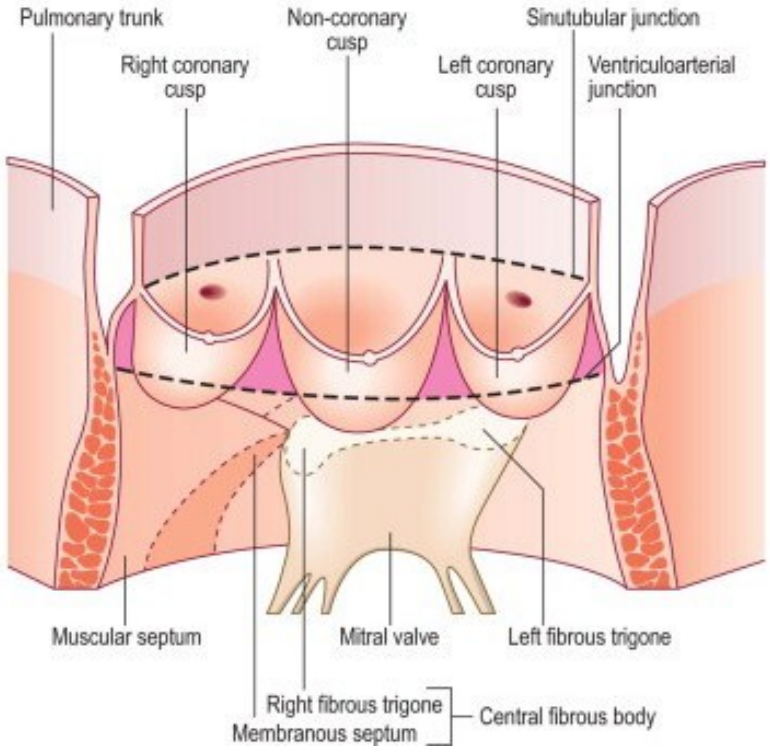

Figure 1.4: Cut open and distended aortic valve showing its components and the insertion of the semilunar cusps. [Reprinted from Gray's Anatomy: The Anatomical Basis of Clinical Practice, 40th Edition, Susan Standring, Ph.D., D.Sc., editor, Churchill Livingstone, Chapter 56: Heart and great vessels, Copyright (2008), with permission from Elsevier and Professor RH Anderson, Institute of Child Health, University College, London]

At the ventricular surface (*ventricularis*), the tissue contains elastin and collagen fibers. In the central layer (*spongiosa*), acid mucopolysaccharides and some collagen fibers are dominant while at the aortic surface (*fibrosa*) contains a dense network of collagen fibers that is essential for the mechanical strength of the leaflets. Originating at the commissures these collagen fibers run circumferentially like the free edge and spread out over the whole leaflet. A similar layered structure present in the lunulea has a similar architecture.

1.1.2.b Functioning of the aortic valve

The aortic valve is thought as a passive structure where the motion of all of its mobile components is the result of the blood flow driven by the pressure gradient between the left ventricle and the aorta. However, It is shown that the expansion of the commissures in a passive response

to pressure gradient and moreover, the decrease in the ventricular valve radius in an active response to myocardial contraction during ejection of the blood flow play a key role in the functioning of the valve. Without the aortic root dilation, valve function and geometry become abnormal and irregular leaflet deformations occur that might cause calcification, and ultimately leading to a diseased valve [2, 3].

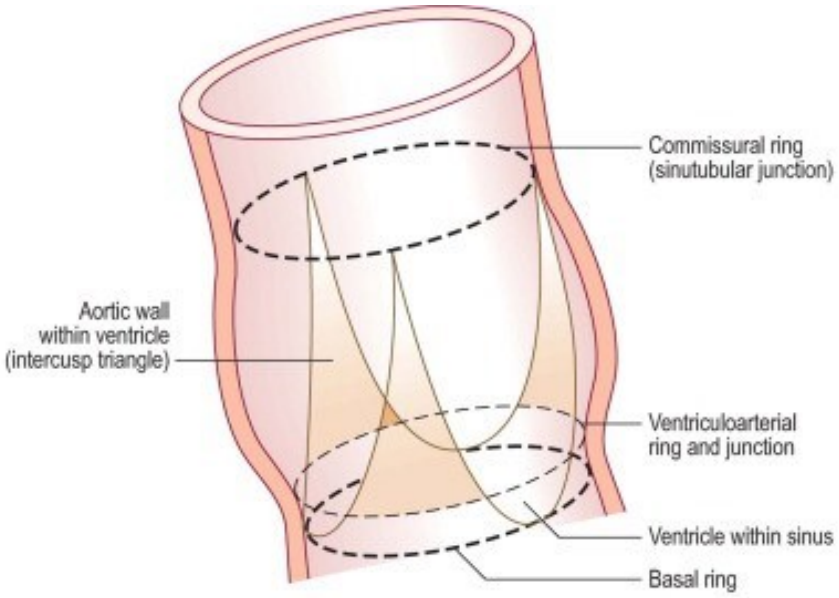

Figure 1.5:The structure of the aortic valve including their three rings [Reprinted from Gray's Anatomy: The Anatomical Basis of Clinical Practice, 40th Edition, Susan Standring, Ph.D., D.Sc., editor, Churchill Livingstone, Chapter 56: Heart and great vessels, Copyright (2008), with permission from Elsevier and Professor RH Anderson, Institute of Child Health, University College, London]

The pattern of the principal events that occur in the cardiac cycle is presented in Figure 1.6. As the pressure of the atria exceeds that of ventricles, the A-V valves open and the blood flows from the atria into ventricles then the generated pressure filed due to the deceleration of the blood stream close the valves between the atria and the ventricles to start the next cardiac cycle. Therefore the leaflets of the aortic valve experience high rate large deformation deform during systolic while they are closed in diastole to seal the aortic orifice withstand the pressure differentials between the left ventricle and aorta.

The healthy valve opens very fast. The bulging of the leaflets towards the aorta begins just before ventricular ejection begins and become completely open when the flow in the ascending aorta reaches 75% of its maximum. As the aortic flow decelerates, due to formation of vortices in the sinuses behind the leaflets, the valve gradually closes. By progression of the adverse pressure

gradient during flow deceleration, it reaches to 80% closure at the end of systole when the flow in the aorta is zero. Ultimately, complete closure coincides with back flow in the ascending aorta [4].

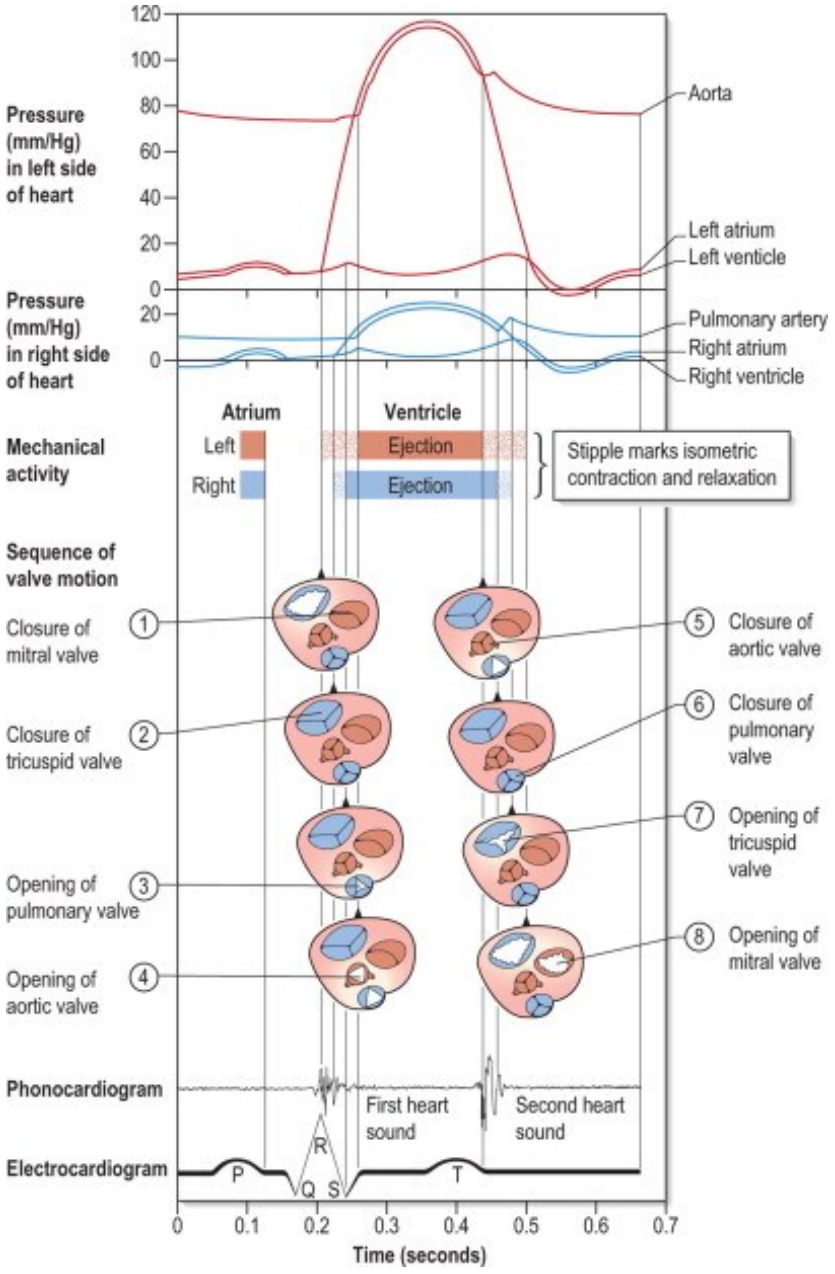

Figure 1.6: The pattern of the principal events that occur in the cardiac cycle. Systole begins at the onset of the first heart sound which corresponds to the beginning of systole while the second sound is heard when the systolic phase ends. [Reprinted from Gray's Anatomy: The Anatomical Basis of Clinical Practice, 40th Edition, Susan Standring, Ph.D., D.Sc., editor, Churchill Livingstone, Chapter 56: Heart and great vessels, Copyright (2008), with permission from Elsevier and Professor RH Anderson, Institute of Child Health, University College, London]

1.1.2.c Aortic valve pathologies

The valvular diseases are highly prevalent and are a public-health problem. Among them, the aortic valve diseases are the most frequent forms accounting for >14,000 deaths in the USA making it the second-leading cause of cardiovascular mortality. Therefore greater importance should be put on the function of this valve and its abnormality [4]. Pathologies of the aortic valves essentially fall under two categories: stenotic valves and incompetent (regurgitant) valves.

Stenotic valve is a major contributor to cardiovascular morbidity and mortality. In this pathology, the caused geometrical and mechanical changes in the aortic valve microstructure due to aging and some pathologies such as arterial hypertension, diabetes, and hyperglycemia, leads to cuspal thickening and loss of extensibility (increasing stiffness). Therefore the leaflets cannot open widely enough. Consequently, the valve imposes significant obstruction to the forward blood flow. In order to compensate the reduced ejected blood flow at each cardiac cycle, the heart must work harder which eventually leads to its abnormal enlargement and heart failure if untreated [5, 6].

Aortic regurgitation (AR) happens when some of the diastolic blood flow leaks back to the left ventricle due to improper sealing of the aortic orifice during diastole. In a normal valve, the integrity of the aortic orifice during is provided by an intact aortic root and tight apposition of the leaflets. AR is a common disorder throughout the world which may be caused by a variety of disorders affecting the aortic root or the leaflets (or both). It is a common disorder throughout the world. This disorder may be due to a variety of diseases of the aortic valve and/or the aortic root. In patients with AR, the total left ventricular stroke volume is the sum of the forward and the backward stroke volume. To maintain the normal cardiac output, the forward stroke volume is increased by progressive dilatation of the left ventricle with increased end-diastolic and end-systolic volumes. This increase will cause higher wall stress and consequently ventricular hypertrophy [7].

1.1.2.d Assessment of the aortic stenosis

Angina, effort syncope, and congestive heart failure are the associated symptoms with aortic stenosis (AS). But, even with a severe aortic obstruction, many patients will remain asymptomatic for years. The onset of these symptoms is linked to a dramatic increase in the mortality rate with an average survival of 2–3 years for patients with AS. Sudden death happens rarely in patients with AS, occurring at a rate of less than 1% per year. Onset of the symptoms is a critical point in the natural history of patients with aortic stenosis. Hence, It is important to assess the severity of

the AS based on hemodynamic measurement to determine the optimal timing of the surgery. According to the American College of Cardiology/American Heart Association (ACC/AHA) guidelines, grading the AS is based on the definition of the aortic jet velocity, mean pressure gradient, and valve area as Table 1.1 [6, 8].

Table 1.1: Classification of the Severity of AS

Severity of aortic stenosis	**Aortic valve area (cm^2)**	**Mean gradient (mmHg)**	**Peak velocity (m/s)**
Mild	>1.5	<25	<3.0
Moderate	1-1.5	25-40	3.0-4.0
Severe	<1.0	>40	>4.0
Critical	<0.6	>60	>6.0

AS can be assessed both noninvasively and invasively with typically similar results. The noninvasive methods use the imaging modalities to assess the hemodynamics data while in noninvasive method, Cardiac Catheterization is used to measure the pressure drop across the aortic valve and the cardiac output. Both noninvasive and invasive assessments may be impacted by inherent assumptions in both techniques. According to the current guidelines, when there is discrepancy between the clinical symptoms and noninvasive findings, invasive assessment of AS severity should be undertaken [9].

Electrocardiography and Chest Radiography are used to diagnose the AS by visualization of the left ventricular hypertrophy and left atrial enlargement. But this imaging modality is not sufficient to fully assess the pathology. For diagnosing and quantification of aortic stenosis, echocardiography is usually used. The presence of aortic stenosis can be reliably detected by two-dimensional echocardiography visually and Doppler echocardiography must be used to assess the severity of AS. The pressure gradient across the aortic valve is related to the obtained velocity by continuous wave Doppler across the valve (v) by application of modified Bernoulli equation as:

$$\text{Pressure gradient(mmHg)} = 4v^2 \tag{1.1}$$

where v stands for the peak Doppler velocity (m/s). By using continuous wave Doppler velocity, it is possible to measure both the maximal instantaneous gradient and the mean aortic valve gradient. However, one of the most important disadvantages of using this imaging modality is the underestimation of the pressure gradient when the Doppler beam is not parallel to the stenotic jet which happens regularly.

Using the continuity equation to calculate aortic orifice area is another routine method in the clinical setting to assess the AS employing the following equation:

$$Aortic\ Orifice\ Area = (LVOT_{TVI}) \times (LVOT_{Area}) / AV_{TVI} \tag{1.2}$$

where LVOT refers to the left ventricular outflow tract and subscript TVI stands for time–velocity integral . All of the parameters on the right hand side of the equation (1.2) are measured by Doppler echocardiography. Since any small error in velocity and diameter measurement using the echocardiography may lead to significant errors in the valvular orifice area calculation, the accuracy of these mentioned non-invasive methods depends on the echocardiographer's skill and expertise.

When there is a discrepancy between the clinical and echocardiographic findings in the AS severity assessment, the invasive method should be employed. In this method, heart catheterization is employed for determination of the for pressure drop across the valve and the cardiac output. Then, the Gorlin equation is used to calculate the aortic valve area as the following equation:

$$Aortic\ Orifice\ Area\ (cm^2) = Flow(ml/s) / 44.3\, C\sqrt{\Delta p} \tag{1.3}$$

In equation (1.3), Flow refers to absolute forward flow across the valve during systolic ejection period expressed in millimeters per second, Δp is the mean transvalvular pressure gradient (mmHg) and C is an empirical constant [6].

1.1.2.e Treatment of the aortic valve pathologies

Unfortunately, pharmacological treatments for aortic valve pathologies are not sufficient, and in some instances medication may be deleterious. Balloon valvotomy, valve débridement, and valve replacement are the current treatments for aortic valve pathologies.

Aortic balloon valvuloplasty relies on fracturing the calcium deposits in the leaflets and stretching the aortic annulus by inserting a large-bore balloon into the stenotic aortic valve and inflating it. The increased valve area stops the left ventricular hypertrophy progression. Although this procedure produces temporary hemodynamic and clinical benefit, the long-term outcomes are

disappointing. Therefore, this procedure should be considered as an alternative method in patients with unacceptably high estimated surgical risks. Similarly, valve debridement involves removing the calcium deposits in the leaflets either by ultrasound or surgery. Surgical debridement usually leads to significant residual stenosis. Ultrasonic debridement, uses sound waves for decalcification of aortic valve stenosis. Although it reduces the aortic valve gradient dramatically, unfortunately, due to impairment of leaflets coaptation, aortic regurgitation develops in many patients.

Aortic valve replacement is the most efficient treatment of aortic valve diseases providing substantial improvements in symptoms and life expectancy. The patient's own pulmonic valve, a bioprostheses and mechanical prostheses are the possible substitutes for replacement of the aortic valve. The ideal prosthetic valve should mimic the characteristics of a healthy native valve such as long durability, high thromboresistance, excellent implantability as well as providing excellent hemodynamics. Unfortunately none of the current substitutes are ideal and each has its own set of risks and benefits [10, 11].

Heterografts and homografts are two general types of the bioprostheses (Figure 1.8.d). In heterografts, porcine or bovine aortic valve leaflets are used. The major advantage of heterografts replacement is its simplicity as well as the low risk of tissue rejection and thromboembolism. The disadvantage is their limited durability. Approximately 50% of valves have failed within 15 years which limits their application for younger patients with longer life expectancy than their durability. Homografts which are constructed from aortic valve of human donors are more durable and resistant. The disadvantages of homografts are the complexity of the peration and their limited availability [7].

In the pulmonic valve transplantation (Ross procedure), the impaired aortic valve is replaced by the patient's native pulmonary valve (autograft). Then, in the pulmonic position a prosthetic valve or a pulmonic homograft is used. Using a durable native pulmonic valve in the high-pressure, high-stress, left side of the valve where prostheses can fail improves the patient's condition. In addition, the bioprosthesis or homograft placed in the pulmonic position, experiences lower pressure making it more durable than if it would be placed into the aortic position. Since this procedure is a complicated technical surgery, it is not applicable to every hospital's surgical program. A schematic drawing showing the procedure is illustrated in Figure 1.7.

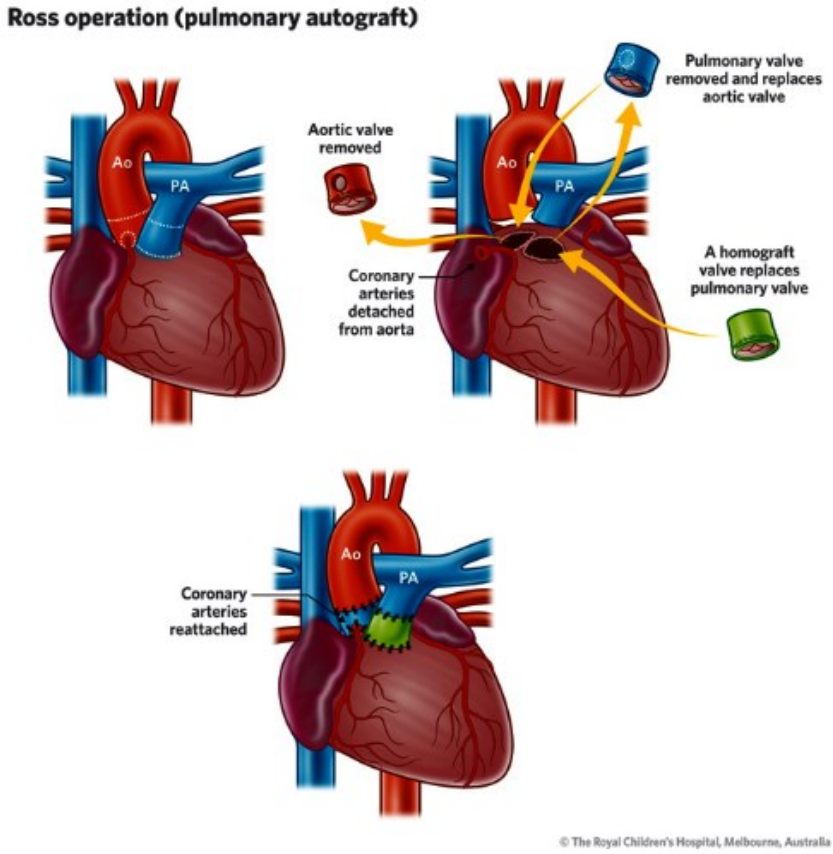

Figure 1.7: Schematic of the pulmonic valve transplantation [Adapted from The Royal Children's Hospital, Melbourne, (downloaded April 2014)]

Mechanical implants are the oldest of the surgical options and still used. Caged ball valves, bileaflet, monoleaflet, are three basic types of mechanical valves. Caged ball valve (Figure 1.8.a) is composed of a silastic ball with a circular sewing ring and a cage formed by 3 metal arches. This type of the mechanical valves is no longer implanted. Monoleaflet valves (Figure 1.8.b) consist of a single disk secured by lateral or central metal struts. The opening angle of the disk relative to valve annulus ranges from 60° to 80°, resulting in 2 distinct orifices of different sizes. In bileaflet valves (Figure 1.8.c), 2 semilunar disks are attached to a rigid valve ring by small hinges. The opening angle of the leaflets relative to the annulus plane varies from 75° to 90°. The full opening of the leaflets in this valve provides little resistance. Although this valve corrects the problem of central flow, it allows some backflow. The main disadvantage of the mechanical implants is that they cause an appreciable amount of damage to the blood itself potentially causing clots. Accordingly, patients with mechanical valves should take blood-thinning medication [12].

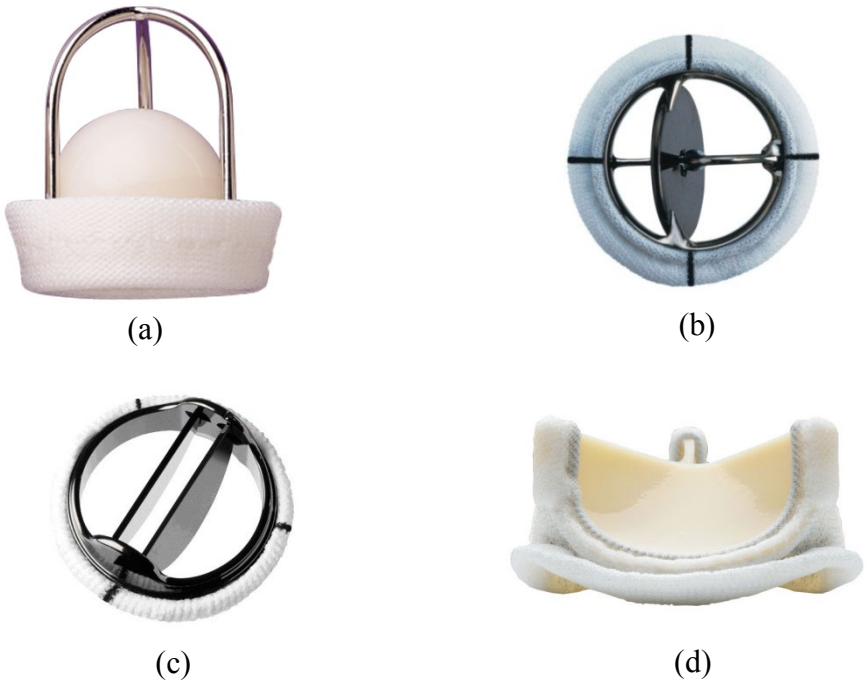

Figure 1.8: (a) Ball and cage aortic valves [adapted from Edwards life science (downloaded April 20140], (b) monoleaflet valve [adapted from Medtronic (downloaded April 2014)], and (c) bileaflet valve [adapted from St.Jude Medical (downloaded April 2014)] (d) bio-prosthetic aortic valve [adapted from Edwards life science (downloaded April 2014]

1.1.3 The coronary arteries

1.1.3.a Anatomy of the coronary arteries

The heart is composed of cardiac muscle tissue which needs to be supplied by oxygen-rich blood to function properly. The coronary arteries supply the myocardium with blood. There are two main coronary arteries that are called the left and right coronary arteries. The left coronary artery (LCA) arises from the left coronary sinus while the right coronary artery (RCA) branches off the left coronary sinus (Figure 1.4). As, after leaving the aorta they circle the heart in the manner of a crown, they are called "coronary" arteries. The LCA circles the left side of the heart while the RCA circles the right side.

The left main and right coronary arteries encircle the heart along the atrioventricular groove placed between the ventricular and atrial chambers of the heart. By reaching the atrioventricular groove, the left main coronary artery bifurcates into two major branches: left anterior descending artery (LAD) and left circumflex artery (MCx). The LAD heads down along the interventricular groove overlying the interventricular septum which is considered as a part of the left ventricle,

therefore blood supply to it is particularly important. The MCx circles the left side of the heart giving rise to a number of small and larger ranches. The small branches head up to perfuse the right atrial region, while the larger branches down to perfuse the lateral and posterior walls of the left ventricle (Figure 1.9).

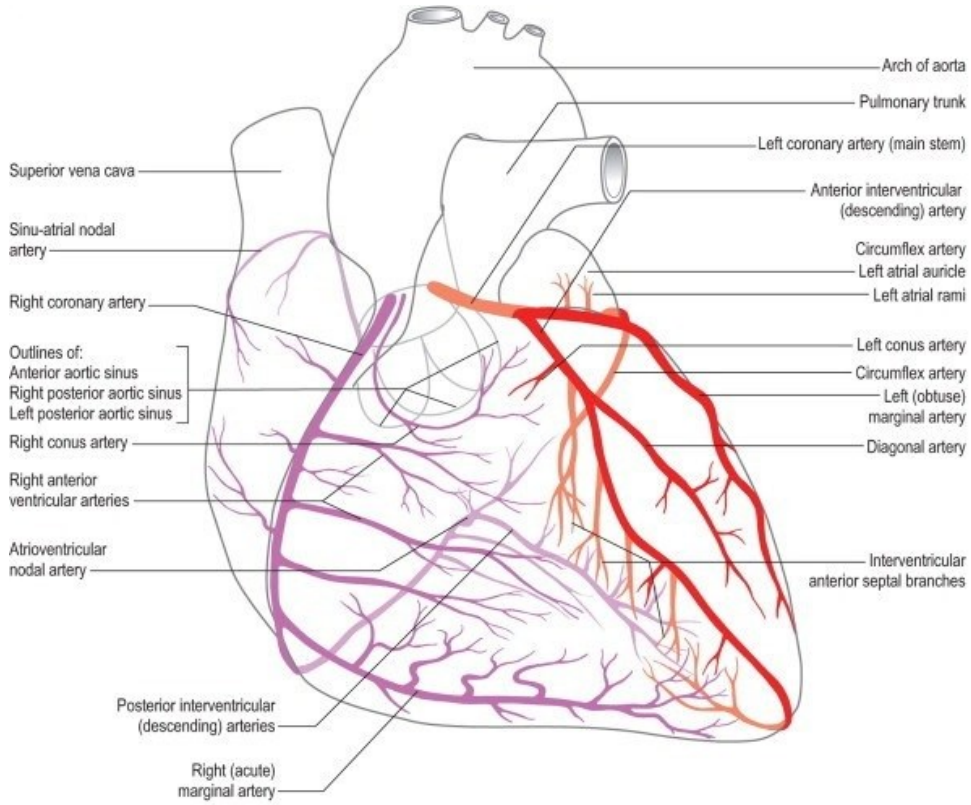

Figure 1.9: Anterior views of the coronary arterial system, [Reprinted from Gray's Anatomy: The Anatomical Basis of Clinical Practice, 40th Edition, Susan Standring, Ph.D., D.Sc., editor, Churchill Livingstone, Chapter 56: Heart and great vessels, Copyright (2008), with permission from Elsevier]

The right coronary artery, after reaching the atrioventricular groove, encircles the right side of the heart to course along the groove. Along its path, it bifurcates to various branches heading up to feed the right atrial region and down to supply the blood to the anterior and posterior walls of the right ventricle (Figure 1.9) [13]. The coronary arteries that run on the surface of the heart, are called epicardial coronary arteries and those which run deep within the myocardium are referred to as subendocardial coronary arteries.

The myocardium perfusion is unique because it mostly occurs in diastole instead of in systole. In other organs, pressure gradient from the arterial source drives the blood flow through the resistance of the arterioles into the capillary bed and finally venous return. In the heart, during

systole due to the compression of the vasculature by its surrounding muscle the subendocardial flow is impeded and only small amount of blood is driven into the epicardial coronaries. During diastole, when the myocardium relaxes the coronary flow resumes to circulate. Therefore, while the maximum pressure gradient happens in systole, flow is maximum in diastole. Hence, myocardial flow phenomena does not fully follow the simple "vascular waterfall" model in which flow moves from highest to lowest pressure [14].

The coronary flow is primarily determined by difference between the aortic diastolic pressure and left ventricular end-diastolic pressure, perfusion time and vasomotor tone which regulates vessel wall diameter to maintain a constant blood flow despite changes in perfusion pressure. Under resting conditions, coronary flow depends only on pressure gradient. Myocardial metabolism, nervous control, humoral control, vascular endothelium are the influencing factors of vasometer tone which will lead to vasodilation (increasing the vessel wall diameter) or vasocontraction (decreasing the vessel wall diameter) to maintain the necessary coronary blood supply in parallel with pressure gradient.

1.1.3.b Pathologies of the coronary arteries

Coronary artery disease (CAD) is the most common type of heart disease and the leading cause of death in Canada and the United States [15, 16]. It is a chronic, progressive disease which might be asymptomatic for a long time. Independent risk factors include smoking, diabetes, hypertension, hyperlipidemia, sedentary lifestyle, genetic factors and obesity. Coronary artery disease is characterized by atherosclerosis in the epicardial coronary arteries which begins with development of fatty streaks, a white/yellow linear discoloration containing lipoproteins and macrophage foam cells. Over time, this develops into a mature atherosclerotic plaque composed of an extracellular lipid core and layers of smooth muscle and connective tissue matrix particular collagen. Cellular interactions in development and progression of atherosclerosis are presented in Figure 1.10.

Although, atherosclerotic lesions are prevalent in most adults, they are largely asymptomatic. As atherosclerotic arteries can remodel to accommodate increasing flow to the artery downstream, the plaque growth does not always results in lumen stenosis. Therefore, even large atherosclerotic lesions may be clinically silent. Depending on the composition of the fibrous cap a lesion can be either stable or vulnerable for which symptoms are different (Figure 1.10).

Stable plaques, due to a thick fibrous cap are more able to resist local mechanical stresses. Therefore, over time they become sufficiently large (stenosis) to restrict blood flow, such that it cannot respond to the increase in metabolic demand. This will lead to the tissue ischaemia. Vulnerable plaques with large lipid pool and a thin fibrous cap are much more prone to rupture. The rupture will lead to the rapid accumulation of platelets and intravascular thrombosis which will result in acute coronary syndromes and myocardial infarction [17].

1.1.3.c Diagnosis of the coronary arteries diseases

In order to diagnose and manage CAD, different imaging methods are developed which can be categorized into invasive and noninvasive techniques. Noninvasive methods such as B-mode ultrasound, CT and MRI are limited in accessing the coronary bed therefore they are mostly granted for imaging the atherosclerosis in other organs arteries. Invasive method includes X-ray angiography, intravascular ultrasound (IVUS), Angioscopy and Intravascular thermography.

X-ray angiography is the current gold standard imaging technique. This method only visualizes the vessel lumen and fails to detect the lesions that do not protrude into the lumen In addition, by this technique, limited information on atherosclerotic plaque composition can be provided. In Intravascular ultrasound (IVUS), a small ultrasound probe is mounted on the end of a catheter which is passed into the vessel to provide a 2-dimensional cross-sectional image of the entire plaque and vessel wall. In addition, the detected plaques can be categorized as soft, fibrous, or calcified by measuring their acoustic properties. However IVUS demands considerable time, expertise, and expense which has limited its clinical application. Angioscopy is a catheter-based technique by which the arterial surface can be visualized. In this method, some assessment of the plaque composition can be made through color of the plaque, however it is less reliable. Intravascular thermography is the most recent innovation in catheter-based technology to diagnose CAD. In this technique, a highly sensitive thermistor is introduced into an artery. Due to their inflammatory cell content, atherosclerotic plaques emit more heat than a normal vessel wall, and vulnerable plaques emit more heat than stable ones. Therefore this technique can diagnose and measure the plaque metabolism. However, the invasive nature of the catheter based technique makes its application limited.

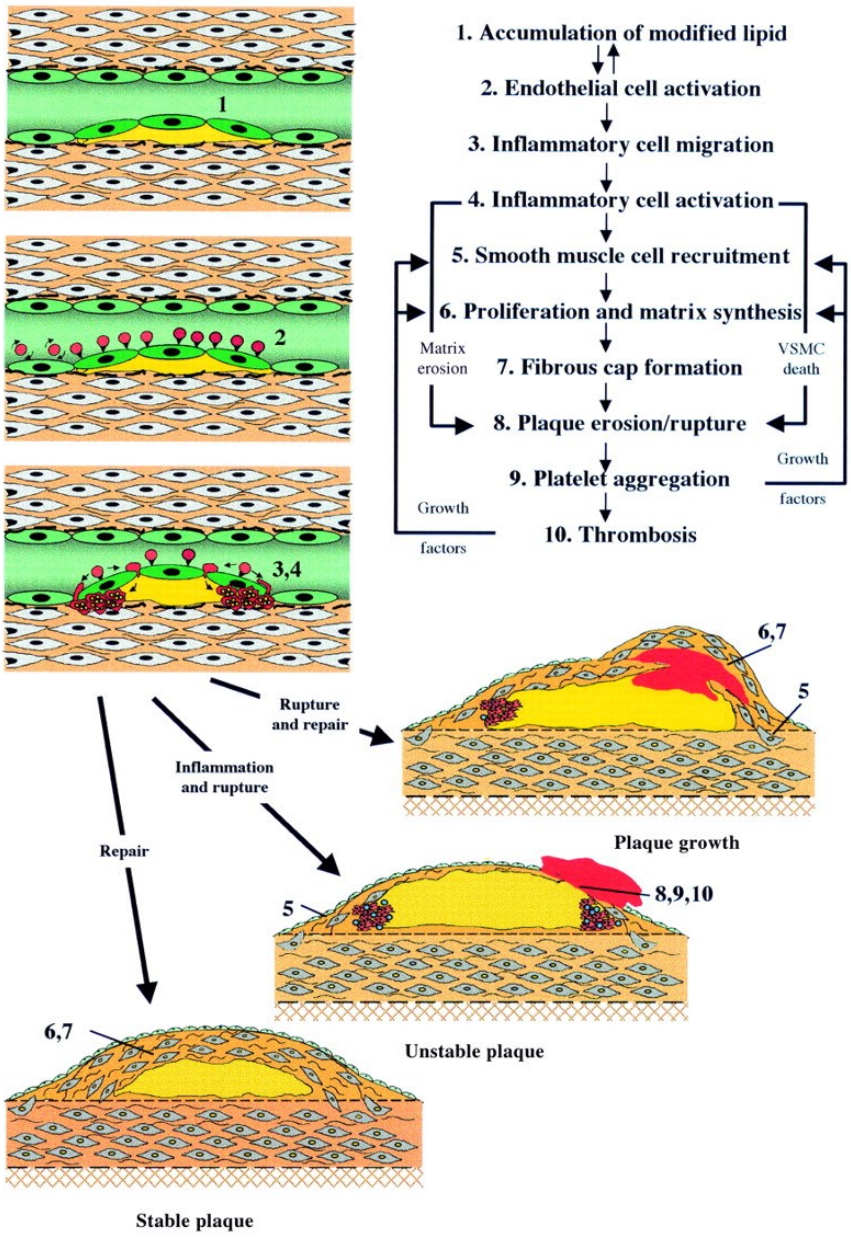

Figure 1.10: Development and progression of atherosclerosis. VSMC, vascular smooth muscle cells. [Reproduced from[17] with permission from BMJ Publishing Group Ltd]

1.1.3.d Clinical index for the assessment of coronary stenosis

As discussed in the previous section, angiography is still the gold standard imaging technique in assessing CAD. Nevertheless, due to its nature, it is a poor tool to establish the functional significance of a given stenosis [18]. Thus, the combination of accurate anatomic assessment and functional information is essential to for the assessment of coronary stenosis (CS). For example,

the combination of coronary angiography and fractional flow reserve (FFR) is proved as the only true “all-in-one” approach since it combines anatomical and hemodynamic assessment.

Fractional flow reserve is defined as the ratio of maximal myocardial blood flow in the case of a diseased artery to maximal myocardial blood flow if that same artery were to be normal at hyperemia. Therefore, it represents the extent to which maximal myocardial blood flow is limited by the presence of CAD. Although FFR is a ratio of two flows, it can be derived from the fraction of mean distal coronary pressure to mean aortic pressure recorded simultaneously during maximal hyperemia. FFR is easily measured during routine coronary angiography by using a pressure wire to calculate the ratio of the pressures. Examples of a typical coronary pressure tracing for FFR measurement during maximal hyperemia are shown in Figure 1.11. FFR has a well-defined cut-off value between 0.75 and 0.80. It has been shown that stenoses with an FFR, 0.75 are able to induce myocardial ischaemia, while stenoses with an FFR .0.80 are shown to exclude ischemia-producing lesions [18, 19].

Figure 1.11: Typical examples of FFR measurement in two patients with coronary stenosis. [Reproduced from [19] with permission from BMJ Publishing Group Ltd]

1.1.3.e Treatment of coronary artery stenosis

Treatment of CAD focuses on taking steps to manage the symptoms and reduce the risk of heart attack and stroke. When the lesion is identified at an early stage, medications such as nitrates, beta blockers, calcium channel blockers, aspirin, or cholesterol-lowering drugs may be prescribed to slow the disease's progress or ease its symptoms. When the artery blockage is severe and the medication therapy is not enough, procedures may be done to improve the myocardium perfusion. These include angioplasty with or without stenting and bypass surgery [20].

Angioplasty is used to open blocked arteries. It is a minimally invasive coronary artery surgery during which the surgeon guides a thin catheter with a balloon at its tip into the narrowed artery. Once in place, the balloon is inflated to compress the plaque against the artery wall. This widens the artery to restore blood flow. Angioplasty is often combined with placement of the stents to keep artery open and decrease its chance of narrowing again. Some stents can be coated with medicine, called a drug-eluting stent which by slowly releasing a drug aids to prevent the growth of new tissue while others are bare-metal stents [21]. Schematic drawing of the coronary angioplasty is presented in Figure 1.12a.

In the case that the arteries are severely narrowed or blocked, Coronary artery bypass grafting may be used. The procedure includes taking a section of a healthy blood vessel from the patient's leg, chest, or arm and grafting it to the coronary artery slightly past the site of the blockage [20]. This creates detours around the narrowed or blocked arteries allowing the coronary circulation (Figure 1.12b).

(a) (b)

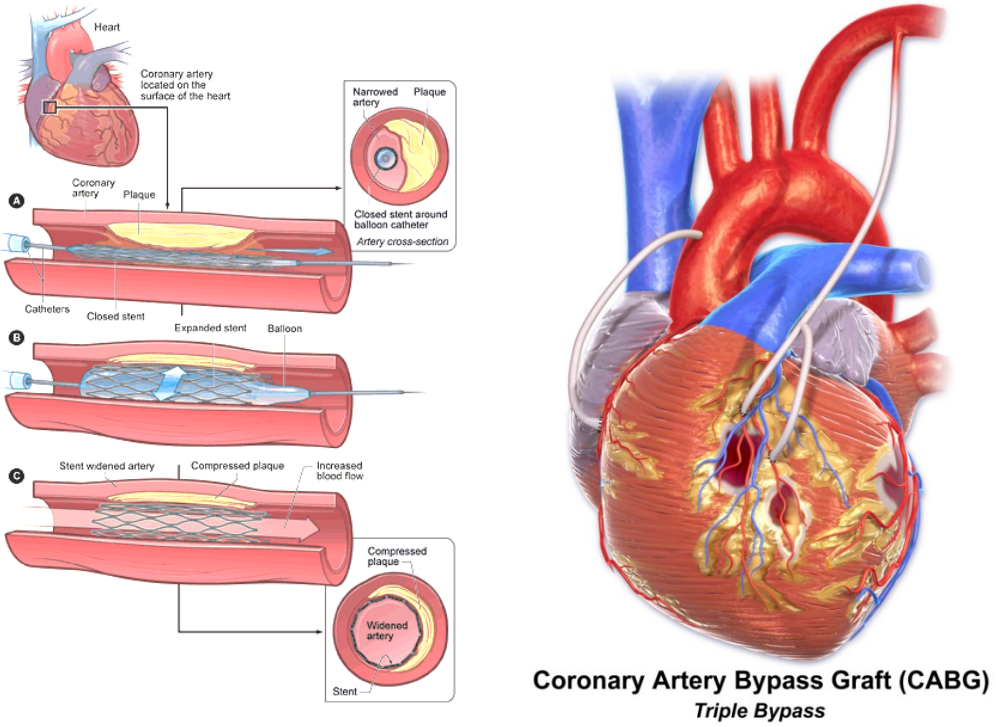

Figure 1.12: Schematic drawing of (a) balloon angioplasty [Source: National Heart, Lung, and Blood Institute; National Institutes of Health; U.S. Department of Health and Human Services] and (b) a coronary bypass graft [Blausen.com staff. "Blausen gallery 2014". Wikiversity Journal of Medicine. DOI:10.15347/wjm/2014.010. ISSN 20018762]

1.1.4 The thoracic ascending aorta

1.1.4.a Anatomy of the thoracic aorta and of its branches

All the blood ejected from the left ventricle, minus that which enters the coronary arteries, is transported through the thoracic aorta to feed the rest of body through the systemic circuit. The thoracic aorta originates at the aortic sinus and then courses upward, slightly to the right up to the level of the second sternocostal joint where it arches obliquely to the left. Subsequently, it descends in the posterior mediastinum and penetrates the aortic hiatus in the diaphragm. Therefore, the thoracic aorta is globally shaped like a candy cane. Due to its three different orientations, the thoracic aorta is subdivided into three sections: the ascending aorta (AA), the aortic arch, and the descending aorta. A schematic of the subsection of the thoracic aorta is presented in Figure 1.13.

The AA is the beginning section of the thoracic aorta which starts at the aortic root. It is the largest artery with a diameter of 2.5 to 3.0 cm. Once the AA exits the pericardium, it gives rise to the aortic arch. The arch of the aorta makes a complete 180º turn giving off three major branches:

First, the innominate (brachiocephalic) artery which feeds the right arm and right portion of head and brain. Next, the left carotid artery through which the blood is transported to the left head and brain. Finally, the left subclavian artery which carries the blood to the left arm. The descending thoracic aorta starts with the last branch vessel off the aortic arch and ends at the first branch in the abdominal aorta; the celiac artery [22].

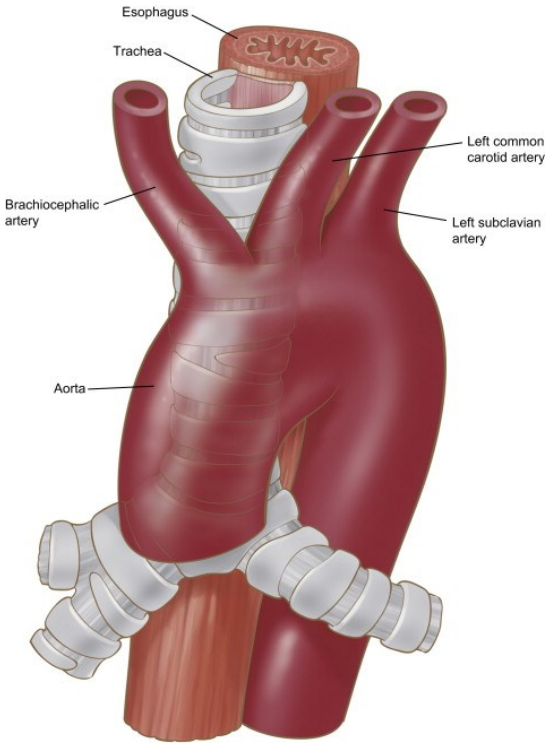

Figure 1.13: Anatomy of the ascending aorta, aortic arch and descending aorta [Reprinted from [22] with permission from Elsevier]

1.1.4.b Pathologies of the thoracic aorta

The permanent localized irreversible dilations of the vessel greater than 50% of the expected normal size of the artery which is known as an aneurysm is the most common disease of the thoracic aorta requiring surgical intervention. The aneurysms developed in the thoracic aorta and abdominal aortas are more lethal than those formed in other blood vessels. They are commonly asymptomatic, and if they are not detected and left untreated, they may grow larger and rupture. Rupture causes fatal bleeding inside the body with very high levels of mortality. It is therefore important that physicians obtain a sufficient knowledge base to evaluate and manage patients with aortic aneurysms and repair them before rupture. Aneurysms are often caused by cystic medial degeneration which degenerates the aortic media. It is characterized by disruption, fragmentation,

and retraction of elastic fibers, the disappearance of smooth muscle cells, and the presence of cysts filled with mucopolysaccharides. This process weakens the aortic wall, allowing for progressive dilation and consequently causes aneurysm [23].

1.1.4.c Diagnosis and treatment of the thoracic aorta aneurysm

Unfortunately, most patients with thoracic aortic aneurysms are asymptomatic. Aneurysms rarely cause symptoms until they rupture. They are accidently discovered on imaging studies when diagnosing other diseases. When the aneurysms involve the root or ascending aorta, they may lead to secondary aortic regurgitation, therefore diastolic murmur that may be detected in physical examination can be a symptom for these kinds of aneurysms. local mass effect, such as compression of the trachea or main stem bronchus that leads to cough, dyspnea, wheezing, or recurrent pneumonitis, compression of the esophagus, or compression of the recurrent laryngeal nerve in tandem with are the symptoms of the large thoracic aortic aneurysms. Rupture of aneurysm which is lethal causes severe pain in the chest, neck, back, and abdomen happen. Most of thoracic aortic aneurysms are evident on chest x-ray films. However, smaller aneurysms and even some large ones may not be clear on chest x-ray films.

In order to define aortic anatomy, Contrast-enhanced CT scanning and MR angiography, which both are accurate in detecting and sizing thoracic aortic aneurysms are recommended imaging modalities. Choosing the optimal one depends on the specific aortic anatomy. For example, when the aneurysms involve the root, since the CT images the root less well and its accuracy in sizing the diameter of the aortic root aneurysms is less than MR, MR is the preferred modality [24].

Surgical procedure of the aneurysm includes cardiopulmonary bypass. In this method, the aneurysm is resected and a prosthetic Darcon graft is used instead of it. When the aneurysm involves the aortic root depending on the leaflets and the aortic sinus a composite aortic repair (Bentall procedure) or a valve sparing root replacement can be performed [25].

1.2 Engineering background

Modeling has become an essential tool for engineering design and analysis. It aims to solve physical problems by applying appropriate simplification. Engineering modeling can be divided into two parts: physical (empirical) modeling and theoretical (analytical) modeling. Physical modeling includes in situ and laboratory model tests from which engineers and scientists obtain useful information to develop suitable algorithms to be used in engineering applications.

Theoretical modeling encompasses at least four steps. The first step is formulating the mathematical description of the corresponding physical problems with appropriate assumptions. The resulting equation is usually in the form of differential or algebraic equations. The second step is the development of a suitable numerical model to approximate the derived mathematical model. The numerical model usually needs to be carefully tested and validated by using the pre-existing data and analytical results. This step also includes error analysis of the numerical model. The third step includes the implementation of the numerical model to obtain solutions. Analysis and interpretation of the numerical results in graphics, charts and tables to support engineering design purposes is the last step in theoretical modeling.

During recent years, in order to describe the behavior of the aortic valve, various approaches have been employed to develop numerical structural models of the aortic valve. The following sections will explain the numerical methods available for modeling the aortic valve region. First, the problem definition and governing equations are given for the fluid and structure computations. Then, after exploring the different numerical methods of solving the governing equations, the solution process will be presented based on the selected method and software.

1.2.1 Governing equations

Due to the interaction between the blood and the vascular tissue in the aortic valve, fluid and solid domains should be established in the model. Figure 1.14 presents a schematic drawing of aortic valve model composed of the vascular tissue and the leaflets in solid domain, Ω_s, and the blood which corresponds to the fluid domain, Ω_f. The entire computational domain is denoted by Ω; i.e., $\Omega = \Omega_f \cup \Omega$ and the fluid-structure interface on which both domains have interaction is defined by $\partial\Omega_s = \Omega_f \cap \Omega_s$.

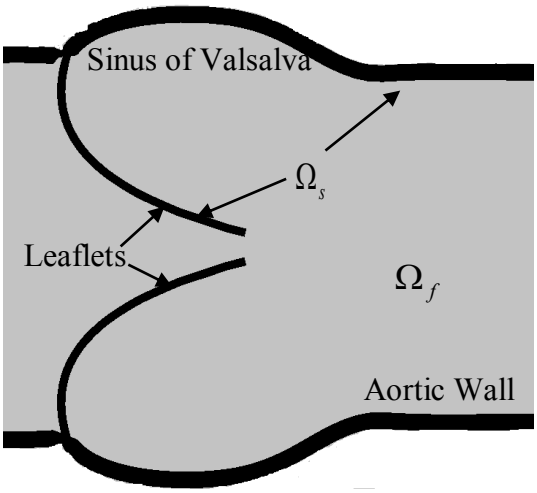

Figure 1.14: Schematic of the fluid and solid domains in the aortic valve model

1.2.1.a Fluid domain

The blood flow is considered to be isothermal and incompressible. The set of equations for the fluid domain read:

$$\rho_f\left(\frac{\partial \boldsymbol{v}_f}{\partial t} + \boldsymbol{v}_f \cdot \nabla \boldsymbol{v}_f\right) = \nabla . \boldsymbol{\sigma}_f + \rho_f \boldsymbol{f}_f \quad \text{in } \Omega_f \tag{1.4}$$

$$\nabla . v_f = 0 \quad \text{in } \Omega_f \tag{1.5}$$

where ρ_f denotes the fluid density, t the time, $\boldsymbol{v}_f$ is the fluid velocity vector , $\boldsymbol{\sigma}_f$ the Cauchy stress tensor, ∇ the gradient operator with respect to the current configuration and $\boldsymbol{f}_f$ the body force applied on the fluid domain. The stress tensor for a Newtonian fluid, can be expressed as:

$$\boldsymbol{\sigma}_f = -p_f \boldsymbol{I} + 2\eta \boldsymbol{D}_f \quad \text{with } \boldsymbol{D}_f = \frac{1}{2}(\nabla \boldsymbol{v}_f + (\nabla \boldsymbol{v}_f)^T) \tag{1.6}$$

with p_f the hydrostatic pressure, $\boldsymbol{I}$ the second-order unit tensor, η the dynamic viscosity of the fluid and $\boldsymbol{D}_f$ the rate-of-deformation tensor.

1.2.1.b Solid domain

The equation of motion and the continuity equation for the incompressible structural domain read:

$$\rho_s \frac{d\boldsymbol{v}_s}{dt} = \nabla . \boldsymbol{\sigma}_s + \rho_s \boldsymbol{f}_s \quad \text{in } \Omega_s \tag{1.7}$$

$$\det(\boldsymbol{F}) = 1 \quad \text{with} \quad \boldsymbol{F} = (\nabla_0 \boldsymbol{x})^T \quad \text{in } \Omega_s \tag{1.8}$$

where ρ_s, v, $\boldsymbol{\sigma}_s$ and $\boldsymbol{f}_s$ denote the density, velocity vector, Cauchy stress tensor and the applied body force, respectively corresponding to the vascular tissue. The vector $\boldsymbol{x}$ denotes the field of structural material points. F describes the material deformation at the current configuration with respect to the reference configuration. $\nabla_\circ$ refers to the gradient operator with respect to the initial configuration while the structural domain behave as a linear elastic and isotropic material according to a Neo-Hookean constitutive law:

$$\boldsymbol{\sigma}_S = -p_S \boldsymbol{I} + G(\boldsymbol{B} - \boldsymbol{I}) \qquad \text{with } \boldsymbol{B} = \boldsymbol{F}\boldsymbol{F}^T \tag{1.9}$$

where p_s denotes the hydrostatic pressure G the shear modulus and $\boldsymbol{B}$ the left Cauchy-Green strain tensor [26]. These equations can be posed regardless of the employed methods to model the interaction. Next, the solution methods for solving the mentioned equations will be presented and after comparing their approaches the suitable one will be selected.

1.2.2 Numerical methods

Engineering analysis of mechanical systems is associated by derivation of differential equations. Once formulated, finding the exact solution of the resulting mathematical models is impossible in most of cases, especially when the resulting equations are nonlinear partial differential equation. Only very simple models with simple geometry such as a rectangle or a circle with a simple boundary conditions can be solved analytically. Therefore solution of the resulting equations requires numerical methods which usually implies the replacement of the continuous equations by ones in which the solution is only obtained at a finite number of points in space and time. With the increase in performance of computational technology, many numerical methods software programs have been developed such as the Finite Element Method (FEM), Finite Difference Method (FDM), Boundary Value Problem (BV), Discrete Element Method (DEM), Material Point Method (MPM), etc. Each method has advantages and limitations for particular problems [27].

The FDM is the oldest which is based upon the application of a local Taylor expansion to approximate the differential equations. The FDM relies on discretization of the PDE by using a topologically square network of lines. This is a potential drawback of the method which limits its accuracy and application to handle complex geometries in multiple dimensions. To address this issue, using of an integral form of the PDEs was suggested which subsequently led to the development of the finite element and finite volume techniques. The use of integral formulations

is beneficial since it leads to a better treatment of Neumann boundary conditions as well as that of discontinuous source terms. Moreover, they are more suitable than the FDM to deal with complex multi-dimensional geometries since the integral formulations is independent of special mesh structure.

In the FVM, the governing equations are integrated over a volume or cell assuming a piece-wise linear variation of the dependent variables. The process includes balancing the fluxes across the boundaries of the all volumes. The flux calculation is quite straightforward in a topologically regular mesh including the same number of divisions in each direction while in an irregular mesh such as tetrahedral mesh, this calculation becomes complicated and expensive as it needs to assure that all the fluxes have been calculated properly.

In FEM method, the dependent variables are represented on the element by a weight function and the governing partial differential equations are integrated over an element or volume. Unlike the FVM, FEM is suitable to deal with irregular geometries as it spends the same time to solve a problem. Hence, for modeling the aortic valve FEM is well-sited as it has an irregular shape [28].

The finite element method (FEM) is the most used discretization technique in structural mechanics. It relies on dividing the domain of the problem into finite number of nonintersecting small elements which together form the mesh. The elements are inter-connected at points common to two or more elements and/or boundary lines and/or surfaces which are referred to as *nodes*. The unknown function is calculated at these nodes in terms of a finite number of degrees of freedom (DOF). Then the values at non-nodal points (that is, in the element interior) is approximated by interpolation of the nodal values.

1.2.3 Fluid-structure interaction

Depending on the phenomena to be studied, the type and the implemented method of the numerical analysis will vary. Structural analysis, computational fluid dynamics and fluid structure interaction (FSI) are the main three categories of the numerical simulations. Each of these methods has its particular application and focus.

Structural analysis is mainly used to determine of the effects of loads on physical structures. Types of analysis include linear statics, nonlinear statics and dynamics, normal modes, dynamic response, buckling and heat transfer. The Lagrangian description is the most frequent methodology in structural analysis. In this approach the elements as well as the material within them deform

under loading. Therefore, the spatial domain and the material domain move as one entity which is the most efficient and accurate method to use for the majority of structural models.

Computational fluid dynamics (CFD) is used to simulate fluid flow, heat transfer, mass transfer, chemical reactions, and related phenomena by solving the governing mathematical equations of the process numerically. Using experimental methods are expensive or in some cases impossible, CFD can provide an insight into flow patterns. Therefore, using CFD will significantly reduce the amount of experiments and the total cost. Since the flowing of a fluid and gas is associated with extreme deformations, in CFD simulation, the elements will become highly distorted as the deformation of the material increases. Therefore in the case of using Lagrangian description for CFD analysis, elements may become ill shaped leading to failure of the simulation process. Therefore, Eulerian method is commonly implemented in solving CFD problems. In an Eulerian reference frame, instead, the material flows through the mesh. This element formulation requires that the volume fractions of the different materials be stored for each element throughout the analysis. Therefore, the mesh does not suffer from distortion problems and large deformations of the material can be processed without failure.

In both structural analysis and CFD, only one medium is considered for simulation while there are many situations in which the fluid is in contact with a rigid structure. These types of problems includes the interactions of the deformable elastic structures with an internal or surrounding fluid flow. An example of these types of problems is the motion of the aortic valve due to hemodynamic loads. Neglecting the interaction between two media will lead to unrealistic results. Fluid-structure interaction (FSI) problems take into account the coupled dynamics of fluid mechanics and structure mechanics. FSI problems play key roles in many scientific and engineering fields. Since for most FSI problems, obtaining analytical solutions is impossible and laboratory experiments are limited, numerical simulation is a good method to investigate the fundamental physics involved in the complex interaction between fluids and solids. FSI simulations are widely used in mechanical engineering and biomedical engineering applications and the dynamics of heart valves is one of the most challenging FSI problems that can be found in the human body [29]. The different types of the FSI problems and the method which is used in this thesis will be presented in the following section.

1.2.4 Classification of the FSI problems

There are two numerical procedures to solve FSI problems 1): The monolithic approach and 2): the partitioned approach. In the monolithic approach, the same framework is used to treat the fluid and structure dynamics therefore, in this method a single system of equation for the entire problem is formed which is solved simultaneously by a unified algorithm. In this approach, the interfacial conditions are implicit during the solution process. Using this approach will lead to a better accuracy for a multidisciplinary problems, but more significant resources and expertise are required to perform this procedure. In contrast, in the partitioned approach the fluid and the structure are considered as two computational fields which can be solved separately with their respective mesh discretization and numerical algorithms. The interfacial conditions are used explicitly to link the information between the fluid and structure solutions. A successful implementation of the partitioned method to solve a FSI problem will lead to a reduction of the code development time. In addition by using this approach, it would be possible to take the advantage of commercial codes for each domain. The challenges of this approach are, linking the algorithms to perform an accurate and efficient FSI solution and dealing with changes in the location of the interface and the related quantities [30].

Another general classification of the FSI solution procedures is based on dealing with meshes: the conforming mesh methods and non-conforming mesh methods (Figure 1.15). During the past years, different methods FSI modeling are proposed, each having its advantages and disadvantages. In the conforming mesh method, the interface conditions are treated as physical boundary conditions. As a result, the interface location is considered as a part of the solution. This procedure, needs the meshes to conform to the interface (Figure 1.15.b). Due to the motion and deformation of the interface, re-meshing is required during the solution process. One of the most well-known methods used to capture the interaction between structure and fluid is the Arbitrary Lagrangian Eulerian method (ALE). On the other hand, the non-conforming mesh methods considers the boundary interface and its associated conditions as constraints to be imposed on the model equations. As a result, the fluid and solid equations can be conveniently solved separately with their respective grids, and re-meshing is not performed in this approach (Figure 1.15.c). Fictitious domain method is the a widely used non-conforming mesh methods for FSI applications [31]. Both methods will be discussed in more detail in the following subsection.

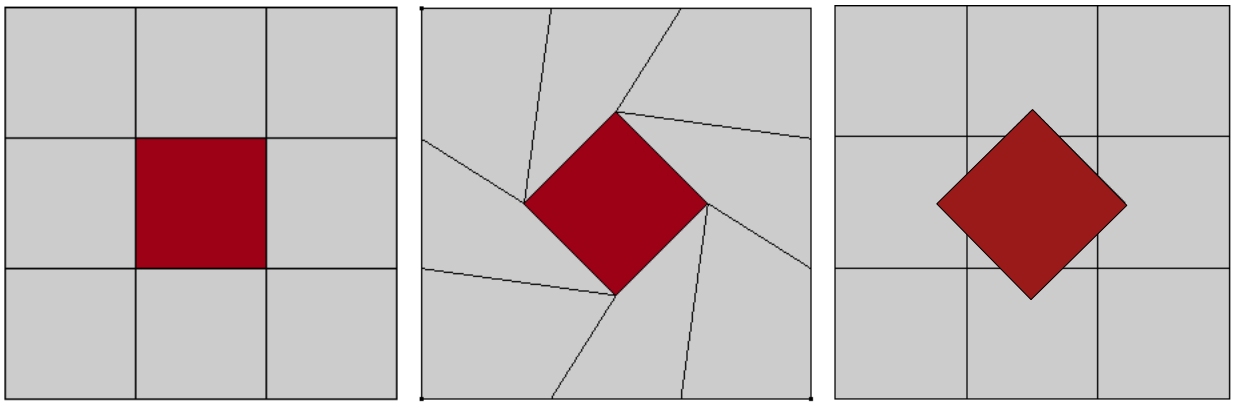

(a) (b) (c)

Figure 1.15: Schematic representation of boundary-fitted (b), and non-boundary-fitted approaches fitted (c) approaches. Rotation of the red block from initial configuration (a) leads to (b) and (c)

1.2.4.a Arbitrary Lagrangian Eulerian method (ALE)

As discussed in section 1.2.3, Lagrangian description and Eulerian description are widely used for non-linear solids and fluids respectively. Large mesh distortions induced by large displacements, rotations, or deformations of the fluid-structure interface makes Lagrangian method and Eulerian method inaccurate unpractical. To address this issue, the ALE algorithm is often employed to implement the coupling an Eulerian description of the fluid domain to a Lagrangian description of the solid domain. As presented in Figure 1.16, this approach is composed of 2 steps. First, a Lagrangian step is performed during which the material (red lines in Figure 1.16) undergoes deformation and translation. Second, the Lagrangian mesh is rezoned (remapped) onto the ALE reference frame at regular intervals to reduce the mesh distortion. The ALE reference frame moves arbitrary in space independently from of the material and spatial references. The element topology (nodal connectivity) remains the same, but the nodes move through the material, changing the mass of each element. A new Lagrangian mesh is created, which again behaves as a normal Lagrangian mesh until the next advection (transport) step takes place [32]. More details about the ALE reference formulation is presented in Appendix A.

The ALE approach is mostly used for FSI problems and its advantage is providing a strong coupling. As long as rotations, translations and deformations of the structure remain within certain limits, this approach works very well. However, for problems in which the solid undergoes extreme deformations such as large deformation and rotation of the aortic valve leaflets within the fluid

domain, the elements become ill-shaped and ALE alone does not suffice and it needs to be combined by re-meshing which can be expensive and complicated process [33, 34].

The strong form of the equation of motion and the continuity equation set for the fluid domain defined on an arbitrary computational grid read (Appendix A):

$$\rho_f\left(\frac{\partial \boldsymbol{v}_f}{\partial t} + (\boldsymbol{v}_f - \boldsymbol{v}_{grid})\cdot\nabla \boldsymbol{v}_f\right) = \nabla.\boldsymbol{\sigma}_f + \rho_f \boldsymbol{f}_f \quad \text{in } \Omega_f \tag{1.10}$$

$$\nabla.v_f = 0 \quad \text{in } \Omega_f \tag{1.11}$$

using the previously defined symbols (section 1.2.1.a). Equation (1.10) represents the (ALE) formulation of the equation of motion in which $\boldsymbol{v}_{grid}$ refers to the velocity vector of the moving fluid grid (Appendix A).

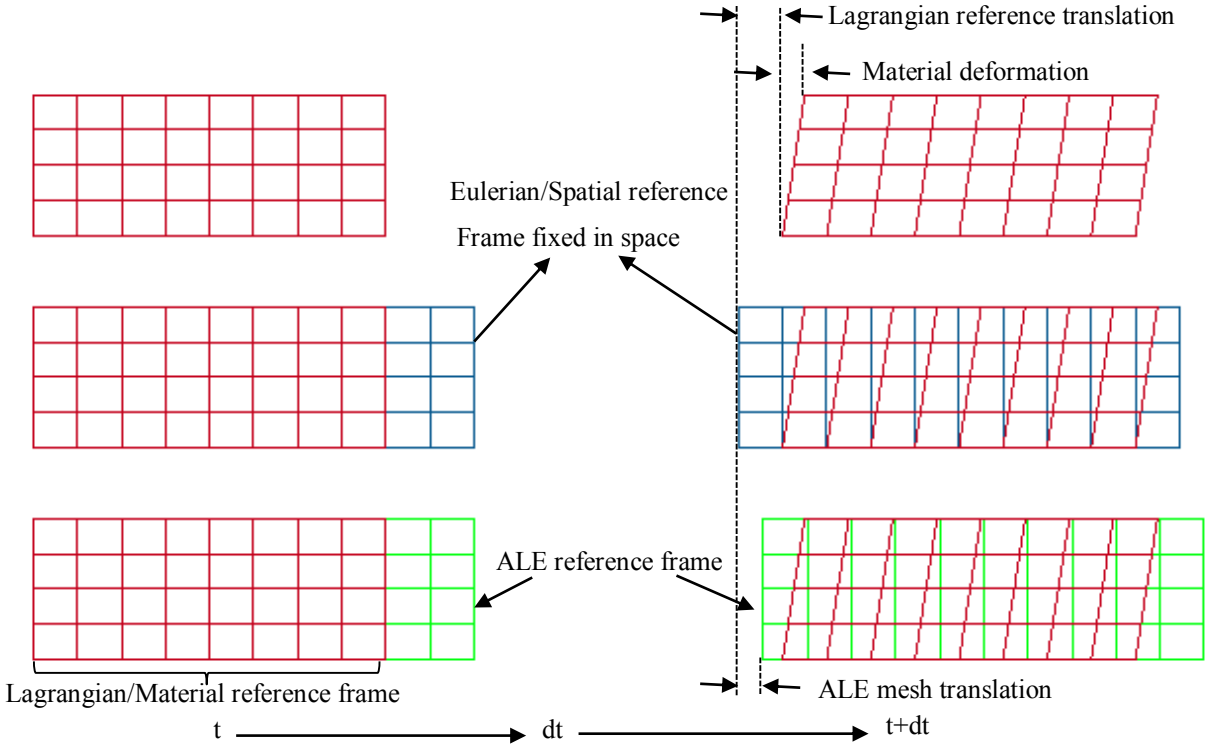

Figure 1.16: Schematic representing of the deformation and translation of Lagrangian vs Eulerian vs ALE reference frames.

1.2.4.b Fictitious domain method (FD)

Contrary to the ALE technique in which fluid–solid interface is accurately captured, other types of methods do not require any adjustment of the fluid mesh/grid. Among the non-boundary-

fitting method for FSI applications, the fictitious domain method (FD) method is the most widely used and was proposed by Glowinski et al. [35, 36] and Bertrand et al.[37]. In this technique, the fluid domain includes an immersed set of non-conforming boundary points. The interaction between this solid boundary with the fluid domain is implemented by imposing a Lagrange multiplier as a kinematic constrain to couple the velocity of each of these solid point to the (interpolated) fluid velocity at that point. The introduction of Lagrange multiplier is the basic idea behind the non-boundary-fitting FSI methods which permits these to be non-conforming and consequently no re-meshing is required in this approach.

The obtained results from FD method in terms of the solid displacement and the general flow behavior are satisfactory. However, as mentioned previously, since in in this approach, solid boundary crosses the fluid mesh, an interpolation to the immersed boundary is required which leads to less precise results in regions near the fluid–solid interface. Hence, the calculated gradients in pressure and velocity fields and consequently the shear stress near the interface are associated with errors. To resolve this issue, FD method need to be combined with re-meshing which will be discussed in the following section.

1.2.5 Combined fictitious method adaptive meshing (ALE) method

The large deformation experienced by the leaflets during each cardiac cycle leads to rapid degeneration of the fluid mesh. Therefore modeling the complete closure phase of the leaflets using the ALE method without re-meshing is impossible. Performing re-meshing to maintain the quality of the computational mesh can be expensive and complicated as it is associated with interpolation techniques to map state variables from the old mesh to the updated one. Conversely, the FD approach is problematic for the shear stresses along the FSI interface. Furthermore, during the diastolic phase of the cardiac cycle, the leaflets are subjected to high pressure gradient, modeling the aortic valve by FD technique will lead to imprecise results for the pressure. As the shear stress and the transvalvular pressure gradient play an important role in the functioning of the leaflets, application of the FD method may not be sufficient for the FSI modeling of the aortic valve. Combination of two approaches which was proposed by Van Loon et al is proven to minimize their drawbacks while keeping their benefits [38]. The approach consisted of FD technique associated ALE time step and local mesh adaptation in order to support the large deformation and motion of the valve.

1.2.5.a Fluid-structure coupling

A schematic drawing of the immersed structure of the aortic valve in the fluid domain is presented in Figure 1.17. The fluid domain and solid domain are denoted by Ω_f and Ω_s respectively, while the fluid-structure interface and the boundary of the fluid domain are defined by $\partial\Omega_s = \Omega_f \cap \Omega_s$ and $\partial\Omega_f$.

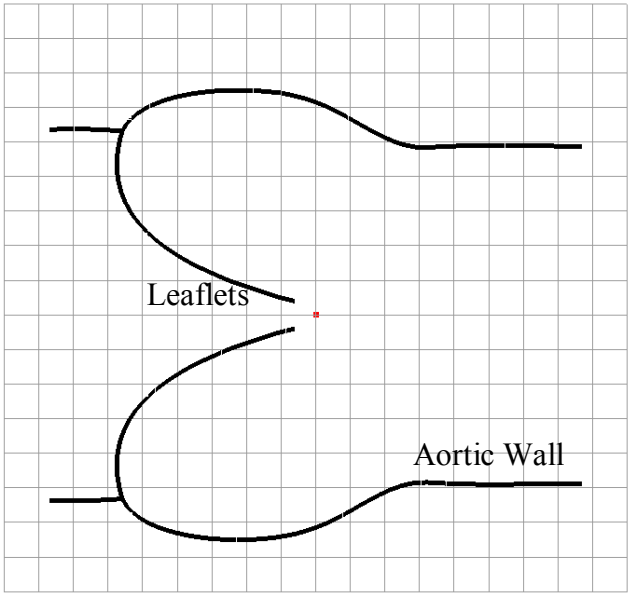

Figure 1.17: The schematic drawing of the fictitious domain method for the solution of the fluid-structure system in the aortic valve model.

Physically Ω_f and Ω_s cannot occupy the same domain in space and their interaction happens only at $\partial\Omega_s$. Hence, a new definition of the fluid domain excluding the solid domain denoted by Ω_f / Ω_s is necessary. Consequently, the governing equation of the fluid domain in ALE reference frame presented in section 1.2.4.a should be defined in Ω_f / Ω_s rather than Ω_f. In order to capture the fluid-structure interaction, the fluid and solid domains should be coupled. This coupling is performed by applying a no-slip condition,

$$\boldsymbol{v}_s - \boldsymbol{v}_f = 0 \tag{1.12}$$

at the boundary of the solid domain, $\partial\Omega_s$.

1.2.5.b Weak form of the governing equations

Based on the strong form of the governing set of equations (1.7), (1.8), (1.10) and (1.11) the weak formulation for the total set of equations will be derived. With $H^1(\Omega)$ as the Sobolev space and by defining the space of the acceptable solutions for the velocity vector in both domains as the following:

$$W_v = \left\{ (\boldsymbol{v}_f, \boldsymbol{v}_s) \,|\, \boldsymbol{v}_f \in H^1(\Omega_f / \Omega_s)^2, \boldsymbol{v}_s \in H^1(\Omega_s)^2, \boldsymbol{v}_f = \boldsymbol{v}_s \;\; on \;\; \partial\Omega_s \right\} \tag{1.13}$$

and the corresponding test functions space:

$$W_o = \left\{ (\boldsymbol{w}_f, \boldsymbol{w}_s) \,|\, \boldsymbol{w}_f \in H^1(\Omega_f / \Omega_s)^2, \boldsymbol{w}_s \in H^1(\Omega_s)^2, \boldsymbol{w}_f = \boldsymbol{w}_s \;\; on \;\; \partial\Omega_s \right\} \tag{1.14}$$

interestingly, deriving the weak form of the equations (1.7) and (1.10) within the framework of the finite element method and adding them together yields [39]:

$$\begin{aligned} &\int_{\Omega_f/\Omega_s} \boldsymbol{w}_f . (\rho_f \frac{\partial \boldsymbol{v}_f}{\partial t} + \rho_f (\boldsymbol{v}_f - \boldsymbol{v}_{grid}) \cdot \nabla \boldsymbol{v}_f - \rho_f \boldsymbol{f}_f) d\Omega + \int_{\Omega_f/\Omega} (\nabla \boldsymbol{w}_f)^T : \boldsymbol{\sigma}_f d\Omega + \\ &\int_{\Omega_s} \boldsymbol{w}_s . (\rho_s \frac{d\boldsymbol{v}_s}{dt} - \rho_s \boldsymbol{f}_s) + \int_{\Omega_s} (\nabla \boldsymbol{w}_s)^T : \boldsymbol{\sigma}_s d\Omega = \int_{\partial\Omega_f} \boldsymbol{w}_f . (\boldsymbol{\sigma}_f . \boldsymbol{n}_f) + \int_{\partial\Omega_s} \boldsymbol{w}_s . (\boldsymbol{\sigma}_s . \boldsymbol{n}_s) \end{aligned} \tag{1.15}$$

where $\boldsymbol{n}_f$ and $\boldsymbol{n}_s$ are the normal unit vectors on the fluid and solid surfaces, respectively. The basic idea of the fictitious domain method is to extend the fluid problem from Ω_f / Ω_s to Ω_f and couple the velocities $\boldsymbol{v}_f$ and $\boldsymbol{v}_s$ not only via the solid surface $\partial\Omega_s$, but the entire solid domain. Hence, the velocity and variance spaces need to be modified as follows:

$$\widetilde{W}_v = \left\{ (v_f, v_s) \,|\, v_f \in H^1(\Omega_f)^2, v_s \in H^1(\Omega_s)^2, v_f = v_s \;\; on \;\; \Omega_s \right\} \tag{1.16}$$

$$\widetilde{W}_o = \left\{ (\boldsymbol{w}_f, \boldsymbol{w}_s) \,|\, \boldsymbol{w}_f \in H^1(\Omega_f)^2, \boldsymbol{w}_s \in H^1(\Omega_s)^2, \boldsymbol{w}_f = \boldsymbol{w}_s \;\; on \;\; \Omega_s \right\} \tag{1.17}$$

Following a similar procedure used by Yu [39] and noting that

$$\int_{\Omega_s} (\rho_f \frac{d\boldsymbol{v}_f}{dt} - \rho_f \boldsymbol{f}_f) . (\boldsymbol{w}_f - \boldsymbol{w}_s) d\Omega + \int_{\Omega_s} \nabla (\boldsymbol{w}_f - w_s)^T : \boldsymbol{\sigma}_f d\Omega = 0 \tag{1.18}$$

and adding equation (1.18) to (1.15) yields:

$$\int_{\Omega_f} \boldsymbol{w}_f.(\rho_f \frac{\partial \boldsymbol{v}_f}{\partial t} + \rho_f(\boldsymbol{v}_f - \boldsymbol{v}_{grid})\cdot\nabla\boldsymbol{v}_f - \rho_f \boldsymbol{f}_f)d\Omega + \int_{\Omega_f}(\nabla \boldsymbol{w}_f)^T : \boldsymbol{\sigma}_f d\Omega +$$
$$\int_{\Omega_s} \boldsymbol{w}_s.((\rho_s - \rho_f)\frac{d\boldsymbol{v}_s}{dt} - (\rho_s \boldsymbol{f}_s - \rho_s \boldsymbol{f}_f))d\Omega + \int_{\Omega_s}(\nabla \boldsymbol{w}_s)^T : (\boldsymbol{\sigma}_s - \boldsymbol{\sigma}_f)d\Omega \quad (1.19)$$
$$= \int_{\partial\Omega_f} \boldsymbol{w}_f.(\boldsymbol{\sigma}_f.\boldsymbol{n}_f) + \int_{\partial\Omega_s} \boldsymbol{w}_s.(\boldsymbol{\sigma}_s.\boldsymbol{n}_s)$$

To enforce the fictitious fluid domain to move at the same velocity as the solid domain, equation (1.16), Lagrange multiplier λ_{fsi} is introduced to equation (1.12) to relax the constraint $\boldsymbol{v}_f = \boldsymbol{v}_s$ on Ω_s from equation (1.15) the combined velocity space and the corresponding constraint from the combined variance space and also taking the weak form of the continuity equation of the both domains, equations (1.8) and (1.11) , as well as the coupling equation will lead to the following set of the weak form equation of fluid solid interaction in combined FD and ALE approach :

$$\int_{\Omega_f} \boldsymbol{w}_f.(\rho_f \frac{\partial \boldsymbol{v}_f}{\partial t} + \rho_f(\boldsymbol{v}_f - \boldsymbol{v}_{grid})\cdot\nabla\boldsymbol{v}_f - \rho_f \boldsymbol{f}_f)d\Omega + \int_{\Omega_f}(\nabla \boldsymbol{w}_f)^T : \boldsymbol{\sigma}_f d\Omega +$$
$$= \int_{\partial\Omega_f} \boldsymbol{w}_f.(\boldsymbol{\sigma}_f.\boldsymbol{n}_f) - \int_{\Omega_s} \lambda_{fsi}.\boldsymbol{w}_f \quad (1.20)$$

$$\int_{\Omega_f} q_f(\nabla.v_f) = 0 \quad (1.21)$$

$$\int_{\Omega_s} \boldsymbol{w}_s.((\rho_s - \rho_f)\frac{d\boldsymbol{v}_s}{dt} - (\rho_s \boldsymbol{f}_s - \rho_s \boldsymbol{f}_f))d\Omega + \int_{\Omega_s}(\nabla \boldsymbol{w}_s)^T : (\boldsymbol{\sigma}_s - \boldsymbol{\sigma}_f)d\Omega \quad (1.22)$$
$$= \int_{\partial\Omega_s} w_s.(\sigma_s.n_s) + \int_{\Omega_s} \lambda_{fsi}.w_s$$

$$\int_{\Omega_s} q_s(\det(\boldsymbol{F}) - 1) = 0 \quad (1.23)$$

$$\int_{\partial\Omega_s} w_{fsi}(v_s - v_f) = 0 \quad (1.24)$$

where q_f, q_s and w_{fsi} are trial functions associated with equations (1.8), (1.11) and (1.12) in the defined space.

1.2.5.c Discretization

Using the finite element method, the Equations (1.20)-(1.24) are spatially discretized by dividing the fluid (Ω_f), solid (Ω_s) an the interface ($\partial\Omega_s$) into a number of non-overlapping elements [40, 41]. At nodal points of each element, the velocity unknowns, pressure unknowns and Lagrange multipliers are defined by using the polynomial interpolation based on the corresponding nodal values. Hence, the unknowns become interpolated over the entire domain in piecewise fashion and then the set of equations (1.20)-(1.24) at nodes are solved. In the next section, as the presented method is combined with adaptive meshing, the re-meshing approach is presented while the appropriate solution procedure in FSI modeling of the aortic valve will be discussed in the last section of this chapter.

1.2.5.d Combined ALE and mesh adaptation.

As discussed in section 1.2.5, since in FD technique, solid boundary crosses the fluid mesh, an interpolation to the immersed boundary is required which leads to less accurate results in terms of the transvalvular pressure gradient which plays a key role in valve morphology. To improve the accuracy, mesh refinement is necessary. Consider the vascular tissue structure with the boundary $\partial\Omega_s$ crossing the fluid mesh Ω_f (Figure 1.17). The basic idea of mesh adaptation is creating a boundary $\partial\Omega_f$ inside the fluid mesh which coincides with the solid boundary [38]. To do this, first the intersection of the solid boundary with fluid mesh is found, then selected nodes of fluid mesh are positioned on the intersected curve and then shifted along the this curve to fit the nodes of the solid boundary.

The repositioning of the fluid nodes around the boundary curve influence the elements shape affecting the results. For this, the smoothing is performed in several node layers around the boundary curve. According to the algorithm presented by Freitag and Ollivier-Gooch [42], first, Laplacian smoothing is used to calculate the new position of nodes by finding the center of the surrounding vertex nodes. Then, an angle optimization algorithm is employed to enlarge the angles of elements in the case that they are too small. For more details, we refer the reader to the work of Van Loon et al [38]. As previously, described in section 1.2.4.a, In ALE approach, the Eulerian fluid mesh moves arbitrary in space. Since the Lagrangian structural domain moves in time, every time step, the fluid mesh should be updated. Within one time step, after performing the Lagrangian step, based on the new position of the solid boundary, the fluid mesh is adapted. Then,

by applying the ALE and mapping procedures, the solutions of the corresponding equations are projected from the old mesh onto the newly created mesh. The distance between the old position and the updated position of the nodes divided by the time step gives the grid velocity $\boldsymbol{v}_{grid}$ which incorporates the convection of the corresponding node. Therefore, by combining the ALE and FD method, the stability of the model under large deformations is improved.

1.2.6 Solution procedure using LS-DYNA

In this study, LS-DYNA (LSTC, Livermore, CA, USA), as a commercial finite element analysis (FEA) software is implemented to solve equations (1.20)-(1.24) using the combined fictitious and adaptive meshing (ALE) methods.

Loosely (weakly) coupled and strongly (fully) coupled schemes are two distinguished schemes in the partitioned approach. The loosely coupled scheme is non-iterative which require only one solution per time step for both domains in a partitioned manner thus it is an efficient method from the computational point of view. However, for problems like the aortic valve model, in which the structural domain density is close to that of the fluid domain, this scheme is proven to be insufficient associated with numerical instabilities [43]. To avoid the numerical instabilities associated with low inertia vascular tissue in the blood domain as mentioned above, a strongly coupled strategy is implemented to solve the aortic valve model described in this thesis. The incompressible flow and the structural solvers are used to solve the fluid and solid domains, respectively and velocity fields are related to the displacement fields by means of implicit time-integration scheme. The adopted solution procedure is illustrated in Figure 1.18 and described next.

First, the initial configuration of both domains is discretized. The iteration counters i for FSI problem and j for the total problem including the ALE and local mesh refinement problem are set to one. Then within each time step, the following steps are taken. The CFD solver solve the fluid domain equations, (1.20) and (1.21), using the initial velocity and pressure conditions. The obtained interaction forces are then applied on the solid domain as the pressure load boundary conditions. Next, the solid domain equations, (1.22) and (1.23), are solved by the structural solver to obtain the structural displacements. Then the convergence is checked by implementing the obtained results to the coupling equation, (1.24). For a non-convergent solutions, certain number of iterations are executed until the convergence condition is satisfied. When the convergence is obtained the structural displacement at interface is used for fluid mesh adaptation to update the

fluid boundary $\partial\Omega_f^{j-1}$, map the results from the old mesh to the updated one and calculate $\boldsymbol{v}_{grid}$. Next, j is updated and the FSI problem is solved again for the new time step until the total problem is converged.

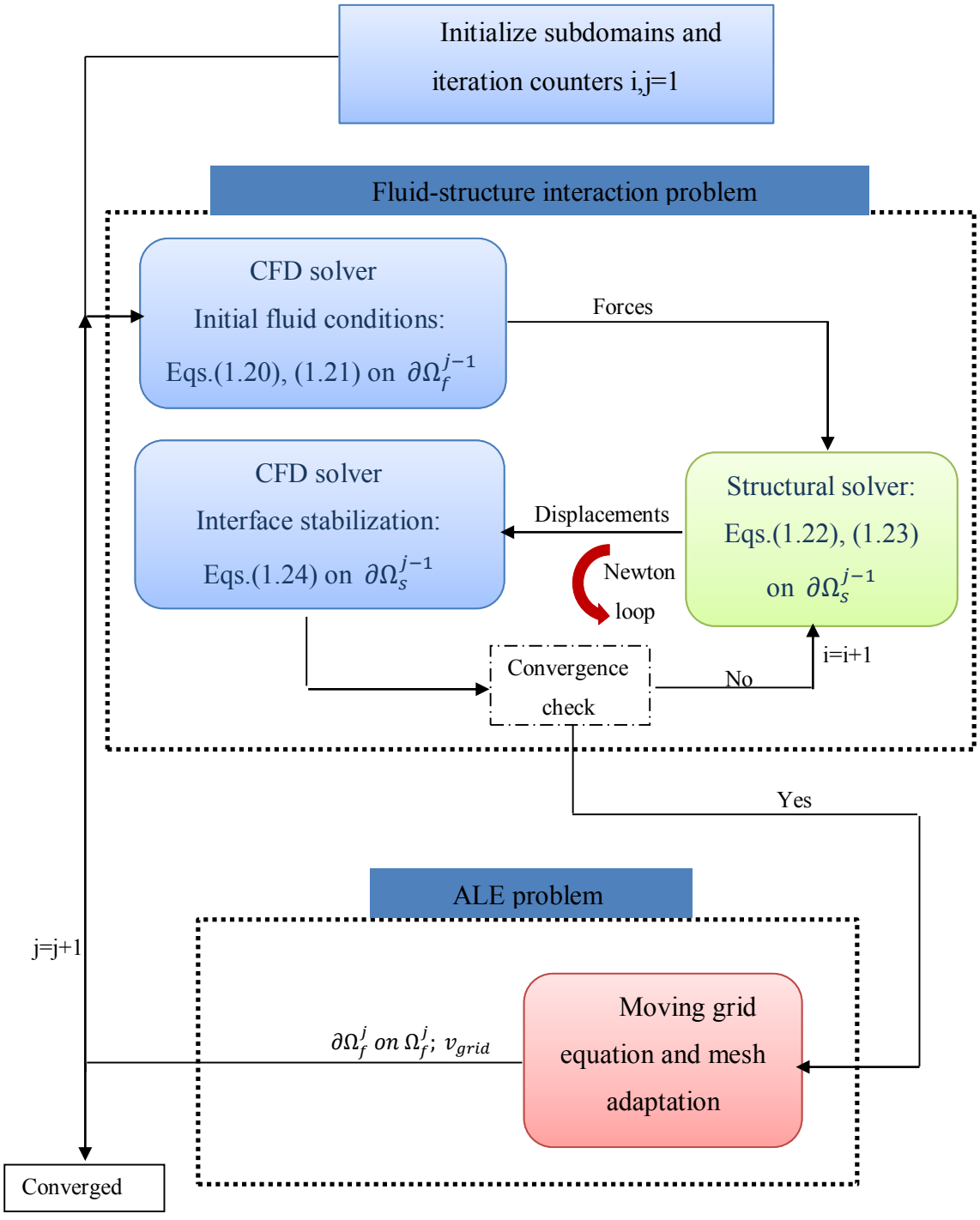

Figure 1.18: The solution process of FSI problems using strongly coupled scheme

Chapter 2: Computational model of the normal aortic root

2.1 Overview

To better clarify the stand point of the presented work in this thesis relative to the previously developed numerical models of the aortic valve, this chapter begins with a brief review of the evolution of the numerical studies for simulating the aortic valve. Then, by using the combined ALE and mesh adaptation approach, the proposed numerical model of the aortic root will be presented and finally the calculation in both domains will be assessed qualitatively and quantitatively.

2.2 Brief history of the aortic valve simulation

Finite element analysis have been used for over thirty years as a tool to understand and explain the function of the aortic valve. Earlier studies focused on the determination of the stress distribution in the leaflets by changing stiffness, thickness and elasticity of the tissue. Their primary purpose was the design optimization of the bioprosthetic and important information about the stress patterns in the valve leaflets, leaflets failure mechanisms and the design optimization of the bioprosthetic valves were obtained using these models.

The earliest numerical study of the aortic valve dates back to the mid-1970s. Due to limitation of the available computational methods and resources, simplified geometries of the valve were used to simulate the aortic valve by employing either in-house user-developed codes or early codes such as MARC. They aimed to explore the possibilities of finite element structural analysis methods [44, 45]. Gould *et al.* in 1973 considered three geometries for closed leaflets: spherical, paraboloid and an elliptical paraboloid models. Under static pressure loading, they calculated the leaflets stress field and the results showed high sensitivity of the stress field to any changes in the geometry of the leaflets [46]. In 1975, Cataloglu *et al.* included the sinuses in the model and did the same observation. They found that under static load, alteration of the stress pattern by adding sinuses to the model is negligible [47]. In the early 80s, a few studies were undertaken to quantify the stresses patterns in typical bioprosthetics to investigate the particularaspects of the leaflet failure [48].

Between 1985 and 1987, Hamid, Sabbah and Stein did a comprehensive study on design optimization of bioprosthetic valves and published their result in a series of four papers. They began with modeling the aortic leaflets with thin shell elements and calculation of the variation of

the stress pattern due to changing the leaflet stiffness [49]. Their subsequent study included definition of the nonlinear material properties for the vascular tissue. Similar to the previous model, it was revealed that the maximum stress happens at the commissures and can be involved in the calcification of leaflets in bioprosthetic [50]. In the last two publications, they reported the impact of variation in the stent-graft flexibility and stent-graft height on the stress patterns [51, 52].

From the beginning of the 90's, the use of commercial software became the widespread for analyzing the aortic valve behavior. MARC and ANSYS codes were implemented to perform structural analyses of the valve under static or quasi-static loads in its closed position. In 1991, to design a novel bileaflet bioprosthetic, by utilizing the membrane elements for the leaflets in the MARC software, Black *et al.* developed the first 3D model of the aortic valve in which bending of the shell elements were permitted. They reported that the maximal stress during the closure stage of the valve, happens close to the attachment of the leaflets to the stent posts [53]. However, due to the numerical instabilities during the leaflets curvature reversal state, their attempt in simulating the full closure phase of the valve was unsuccessful. Few years later, this instability issue was resolved by De Hart and his colleagues by incorporating path-following solution algorithms [54].

The Kunzelman group was the first to develop a numerical model of the heart valves with a specific clinical focus. In 1993, they implemented it with the implicit commercial code ANSYS under quasi-static loading conditions with a transversely isotropic cardiac tissue, oriented along the length of the experimentally observed principal collagen fiber distribution. They examined the impact of the pathological changes, surgical operations and the material property changes on the valve function. Their published papers had a significant role in bringing to the attention of clinicians the importance of engineering numerical models in understanding the function of the natural valves as well as the pathological valves [55-58]. Another strength of their model was using patient specific MRI based models instead of idealized geometry. By processing the resulting MRI images, they extracted three-dimensional data coordinates and corresponding thicknesses, to build a more realistic model. However the main limitation of their work was the static nature of the solution methods leading to simulating the valve only in its closed diastolic phase. Therefore, the calculated results corresponded to the diastolic state of the cardiac cycle.

The numerical instabilities due to large deformation of the leaflets during the cardiac cycle were the main cause of using static loading conditions. In 1996, the Patterson group, by using the LS-DYNA, performed structural dynamic analysis of the valve successfully. In their first study, only the leaflets of the bicuspid bioprosthesis were modeled using a linear and non-linear hyperplastic material properties and achieved more physiological motion of the leaflets [59].

As discussed, one major limitation of all these studies is that the pressure loads were applied on the structure to resemble the effect of the blood on the valve. However, this pressure is not uniform and may affect the valve dynamic behavior as well as the stress distribution on the leaflets. More importantly, structural simulations alone are insufficient to capture hemodynamic properties of the aortic valve. Similarly, CFD simulations are restricted to study of the blood flow not the valve structure. To capture the natural phenomena which occurs in the aortic valve, in 1999, Chew *et al.* did a pioneering study on the aortic valve with FSI components using the ALE approach in LS-DYNA. They created a three dimensional model of a bioprosthetic porcine valve with non-linear material properties to simulate tissue damage to the leaflets. Although their result didn't validate the previous studies, it demonstrated the ability of FSI model of the aortic valve [60].

About one year later, De Hart group, by using a user-defined FD approach, created a two dimensional FSI model of the aortic valve which was expanded to a 3D model subsequently. In their model, low Reynolds number at the inlet of the valve was used to avoid the numerical instabilities. They focused on developing FSI models rather than examination of the impact of particular conditions on the biomedical properties of the model. However, as discussed in section 1.2.4.b, implementing FD approach leads to less accurate results in terms of the calculated pressure and velocity fields gradients in in regions near the fluid–solid interface [54, 61, 62]. Van loon *et al* was the first who implemented combined ALE and FD method using SEPRAN package. Their study was more focused on demonstrating the capabilities of the FSI models to simulate healthy and stenotic the aortic valve and no clinical conclusion was made in their study [38].

In order to predict the coronary flow and blood pressure in epicardial coronary arteries, Kim *et al* in 2010, created a 3D FSI model of the aortic root including the coronary arteries. However, to eliminate the complexity and challenges associated with modeling the large deformation of the leaflets, their model did not incorporate the leaflets and the sinus structure which limits their study to investigate pathologies of this region in a global entity [63]. In our group Ranga *et al*. developed a 3D anatomically derived image-based aortic valve model and by employing ALE method they

created a FSI model of the valve using linear material properties [64]. Later, in 2010, Nobari *et al* expanded this model by adding the right and left main stems of the coronary arteries. Nevertheless, due to limitation of the ALE approach, they used simplified geometries of the coronary arteries in which tapering and branches of the vessels were neglected [65].

To overcome the limitation of the previously simulated FSI models, in this work we have implemented combined ALE and FD methods to develop a global FSI model of the aortic root with inclusion of the coronary arteries and their main branches, as well as the thoracic aorta including the ascending aorta (AA), the aortic arch, and the descending aorta. In a first step, the normal aortic root model in which two coronary ostia are included is created. This model will serve to assess the regional hemodynamic conditions in the aortic root due to pathologies of the valve. Then, in order to study the impact of regional pathologies of the aortic root on the velocity and shear stress distribution downstream in the coronary arteries, in the second step, the normal aortic root is expanded to include the coronary arteries and their main branches as a global model. In the last step the global model is further developed by adding the thoracic aorta including the ascending aorta (AA), the aortic arch, and the descending aorta. This model will aid to investigate the effect of the hemodynamic and geometrical changes in the aorta due to the pathologies or surgical procedure on the hemodynamic conditions in the aortic root and coronary perfusion. Such investigations are impossible with previously established FSI models of the aortic root which do not incorporate the coronary artery and aorta structures.

The following sections of this chapter include detailed information about the creation of the normal aortic root FSI model, while the global model will be discussed on the following chapters.

2.3 Numerical modeling of the normal aortic valve

Generally, the process of creating a numerical model can be subdivided in four steps: generation of the anatomical geometry of the structure, finite element mesh discretization, assigning the material properties and applying the corresponding boundary conditions.

The detailed explanation regarding the steps in creating the normal aortic valve will is discussed in the following sections.

2.3.1 The anatomical geometry of normal aortic root

The normal valve was constructed by using circular cross sections at different distances from the base along the central axis of the aortic valve. These circles correspond to the annulus, sinuses of Valsalva, commissures (Commiss) and sinotubular junction (STJ). However depending on the

health condition, age, gender and weight, the diameters and distances of these circles form the aortic base are variable. As a result, in this study, the average values are used to create an average anatomy of the aortic root structure. Therefore, based on the analysis of ex-vivo measurements performed by several research groups (presented in Table 2.1), an average adult male annulus diameter of 23 mm was taken as the base reference value and all other dimensions are all normalized to this parameter, Table 2.1[66-72].

Table 2.1: Normalized dimensions of the main components of the aortic valve based on the average values reported in the literature.

Research Group	Year	D_{sinus}	H_{sinus}	D_{commis}	H_{commis}	$H_{coaptation}$	D_{STJ}	H_{STJ}	D_{aorta}	H_{aorta}
Lozsadi et al.	1969	1.26		0.86	0.78		1.00	0.87		
Sands et al.	1696	1.12								
Mercer et al.	1973	1.70					0.75	1.01		
Swanson et al.	1974	1.46		1.07	0.71		1.00	0.88		
Thubrikar	1990	1.49		0.89	0.77			0.91		
Kunzelman et al.	1994		0.40			0.54	0.81	1.20	0.91	2.00
Choo et al.	1999						1.03	0.98		
Berdajs et al.	2002			0.90			0.95	0.83		
This Study		1.40	0.40	0.93	0.75	0.54	0.92	0.95	0.91	2.00

To create the CAD representation of the aortic wall, at first, only a third of the structure excluding the sinuses was modeled which was then mirrored across the two planes of symmetry of the valve. Then the full wall including sinuses was constructed by the intersection of the initially created wall by the structure of the sinuses obtained from 3D digitization. Finally the leaflets CAD model which was also constructed by 3D digitization, was added to the wall structure. SolidWorks 2010 CAD software was used to perform all geometry creation tasks. Figure 2.1 depicts the completed CAD model of aortic valve with the above parameters while Figure 2.2 shows different views of the constructed CAD file created using SolidWorks.

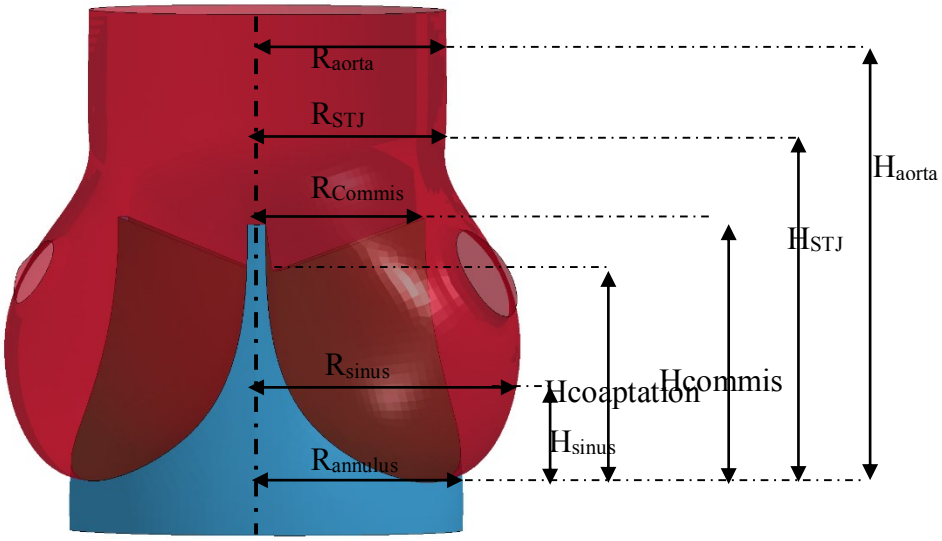

Figure 2.1: Constructed CAD representation of the normal aortic valve with overlay of key parameter measurements

The coronary ostia were created on two of the sinuses based on a gradual tapering to the average artery cross section of 0.28 cm^2 and 0.19 cm^2 on the left and right coronary ostia respectively while the center of the outlet orifices were located at the commissural level [73].

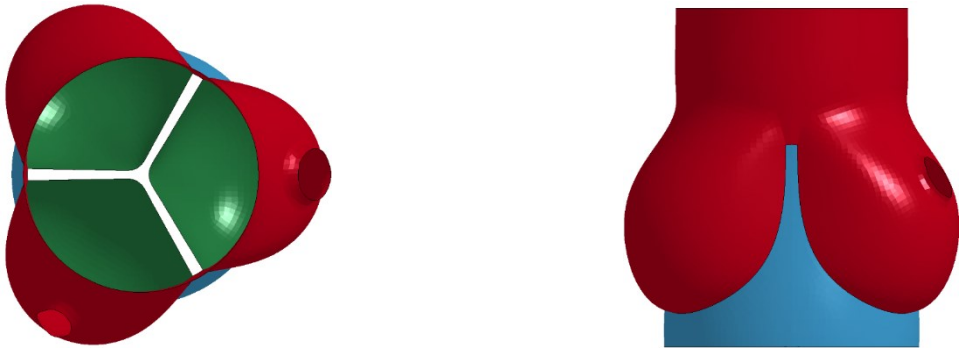

(a) (b)

Figure 2.2: (a) Short axis cut and (b) side view of the created aortic root model (The apparent gap in the first frame is due to the shell thickness and display).

2.3.2 Finite element model

After creating the geometry they were imported into a preprocessing software to be divided into separate parts and then discretized for the implementation of finite element analysis. In this study the creation of the mesh was performed in ANSYS Workbench 14.0 and then the resulting mesh file was transferred to LS-PrePost 3.2 for assigning the material properties, boundary

conditions, element formulation and implementing the FSI approach. Due to the FSI nature of this study, the preprocessing steps were performed on the solid and fluid domains separately as discussed in the following sections.

2.3.2.a The solid domain

In order to apply different boundary conditions, material properties and reach a high mesh quality, the solid domain consisted of three parts with no discontinuity between them and the connected nodes were shared between two adjacent parts.

The Belytschko-Tsay thin shell elements were chosen for the solid domain as they are capable of modeling the bending and accounting for in plane and normal loads. Since these elements have 12 degrees of freedom at each node including translation, acceleration and velocities in x, y and z directions and rotations about x, y and z axes as well, they are appropriate to model large deformation of the leaflets. In complex FSI problems like this model, increasing the number of elements will lead to significant increase in the computational time. On the other hand, there should be a specific ratio between the solid and fluid elements to achieve convergence. Therefore, mesh independency tests were performed to ensure convergence and obtain the minimum allowable element size. An example of mesh independency test on this domain by using the maximum stress happening on the leaflets during the systole cutoff value of the stress variation below 1% is presented in Figure 2.3. As a result, 11,018 quadrilateral elements were used for modeling the solid domain. A constant thickness of 0.5 mm and of 1 mm was assigned to the leaflet and aortic wall elements respectively.

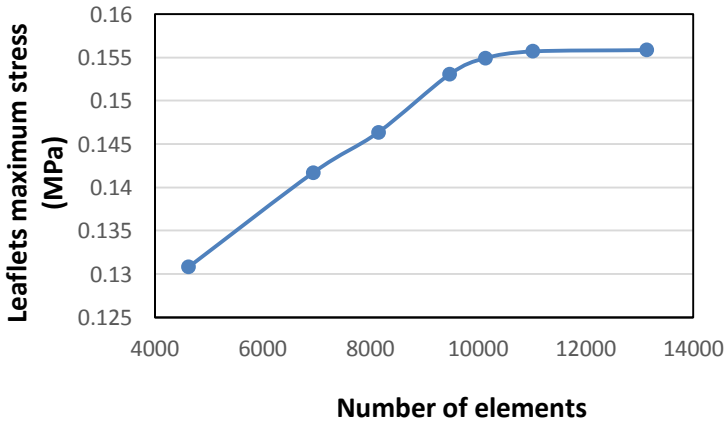

Figure 2.3: Mesh independency test on the solid domain based on the maximum stress on the leaflets during systole

2.3.2.b The fluid domain

The solid domain was immersed in the fluid domain which is additionally subdivided into the ventricular inlet, aortic outlet, and middle reservoir including the interfaces with the corresponding solid structures, right coronary ostia outlet and left coronary ostia outlet. An exploded view of the full assembly including the solid domain and fluid domain parts is shown in Figure 2.4. Unstructured mesh suitable for fluid analysis was selected for the fluid domain which consisted of 340,682 elements. This number of elements was observed to be an adequate after performing mesh independency tests.

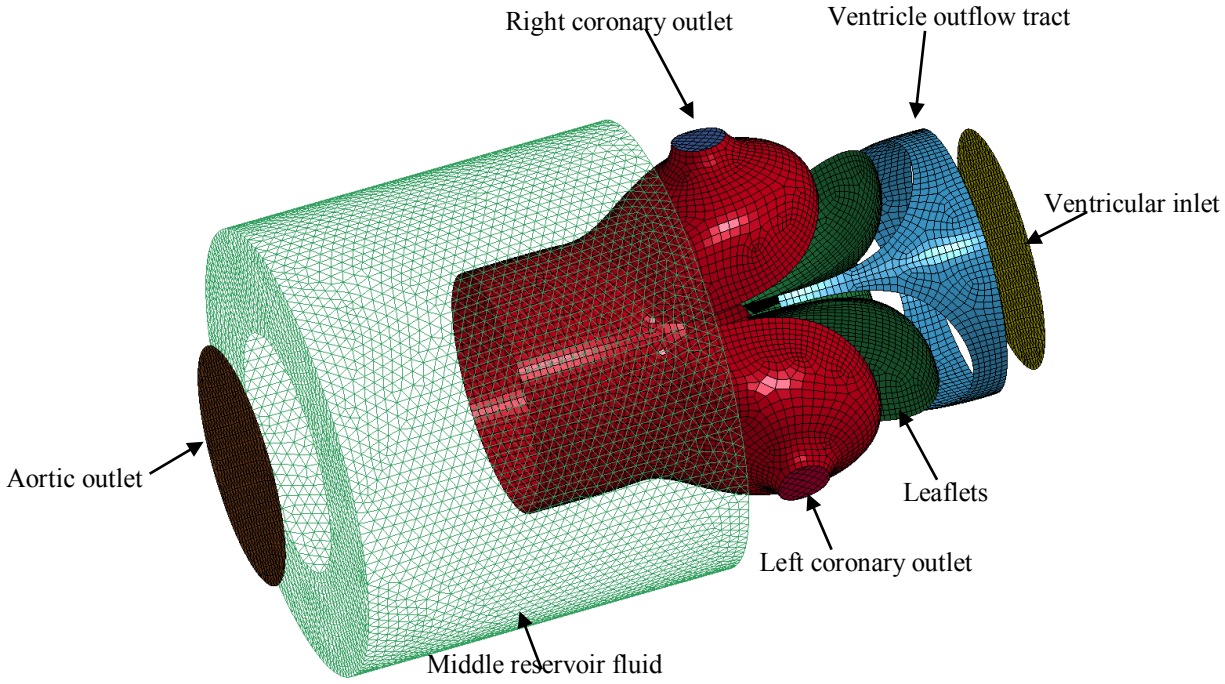

Figure 2.4: Exploded view of the various components of the aortic root model

2.3.3 Material property models

In the following two sections the material properties for the cardiac tissue and the blood as well as the assumption made for their definition are presented.

2.3.3.a Cardiac tissue material model

It is well known that cardiac tissue is heterogeneous, hyperelastic and orthotropic materials. There have been numerous experimental, theoretical and computational studies on the material properties of cardiac tissue especially on the aortic root. As discussed in section 2.2, some studies have incorporated some of these aspects into their numerical models. However, it is should be

indicated that the large deformation of the leaflets makes the numerical model of the aortic valve complex and challenging for stability, incorporating the nonlinear material property to the cardiac tissue increase the complexity and introduces more instability issues to the model. As a result, most of these studies, have either used simplified geometries or neglected the FSI nature by considering only the structural part or the fluid part. Therefore, most of FSI studies conveyed for the aortic root, have used either a small portion of the structure or simplified material properties. Similarly, our model push forward the global aspects of the aortic valve, we indeed implemented a linear elastic material property for the healthy cardiac tissue. Based on a recent study by our group, it was shown that the nonlinear stress-strain curve of the cardiac tissue can be approximated by two linear regions: one at low strain range (below 15%) and another at high strain rates while this linearity is even more strong at low strain rates [74]. In addition, it was shown that under normal physiological conditions, the strain in the aortic root varies in the range of about 10% [75, 76]. Consequently, using linear material property for the numerical simulation of the cardiac tissue under physiological conditions is adequate. In this study the linear elastic material properties with a Young's modulus of 334 KPa and 400 KPa for the aortic root and leaflets, respectively with a Poisson's ratio of 0.45 are implemented. These values are in the physiological range reported in previous studies [77, 78]

2.3.3.b Blood material model

The blood is composed of formed elements suspended in a solution called plasma. The formed elements are the red blood cells (erythrocytes), white blood cells (leukocytes) and platelets (thrombocytes). Among them, the red blood cells are the most dominant representing about 45% of the blood volume in any healthy person. Consequently, the red blood cells have a significant impact on the material properties of blood. Due to the capability of these cells to deform, they have a tendency to align with the flow field at high shear rates and also their capability to form "rouleaux" by sticking to each other at low shear rates, the blood is known to be a non-Newtonian and heterogeneous fluid [79, 80]. Its viscosity depends on the orientation and behavior of the red blood cells. At low shear rates (below 1 s^{-1}) the apparent viscosity of the blood is high, while at high shear rates it reduces significantly. This phenomenon is known as the shear thinning effect of blood which was first reported by Chien *et al.* [81]. Due to the shear thinning nature of the blood, it was shown in several studies that in modeling the blood across the large vessels and the aortic root which is associated with high levels of shear (>50 s^{-1}) a Newtonian assumption can be

used for it [82, 83]. Hence, in this study the blood is modeled as a Newtonian fluid with dynamic viscosity of 3.5 mPa.s and density of 1060 kg/m^3.

2.3.4 Boundary conditions

Because of the FSI aspect of the problem, boundary conditions and loads in terms of each of the two domains will be discussed separately in the following two sections.

2.3.4.a The solid domain

In order to prevent rigid body motion and constrain the displacement in specific directions to be closer to the physiological conditions, three sets of boundary conditions were applied on the solid domain including the ventricular inlet ring, the aortic outlet ring and the coronary ostia. On the ventricular inlet level, a constraint was applied to prevent the movement and deformation of the structure in the axial direction while allowing the root expand radially. On the aortic outlet level, the model is fully constrained to restrict the motion and rotation in any direction to prevent rigid body motion (twisting, rotation, translation). Finally, at the level of the coronary ostia, the model was fully constrained which avoid the issue of instability.

The contact between the leaflets was defined using 'single-surface-contact-mortar' in LS-DYNA which checks for penetration along the entire length of the unshared shell edges. It is a penalty based segment contact which inhibits the shell elements from penetrating through each other.

2.3.4.b The fluid domain

The inlet, the ascending aortic outlet, and the two coronary ostia on the fluid domain, are the locations on which boundary conditions should be imposed in the form of either pressure waveform or flow. For the normal aortic root model, at the inlet, the time dependent difference between the ventricular pressure and the aortic pressure shown in Figure 2.5 was applied. Consequently, the outlets of the fluid domain on the aortic side and both ostia had the free boundary condition. This approach was borrowed from previous studies [60, 84, 85]. As a result, the entire structure of the aortic root was under smaller pressure while maintaining the pressure gradient across the valves.

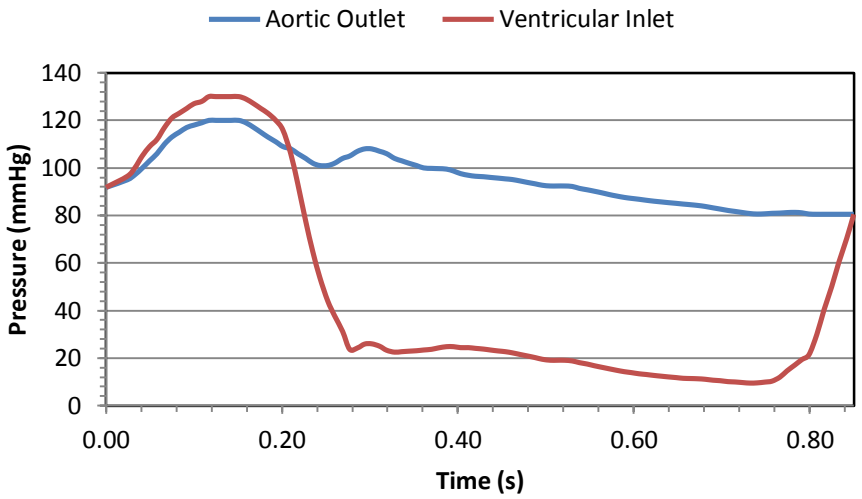

Figure 2.5: Physiological pressures at the ventricular inlet and aortic outlet

2.4 Results of the normal aortic root model simulation

In this section, the results of the simulated model with LS-DYNA using the combined ALE and FD methods and strongly coupled strategy for a simulated cardiac cycle of 0.85s (corresponding to a heart rate of 70 beats per minute) are presented.

2.4.1 The solid domain

The relevant engineering parameters for the solid domain are the leaflet morphologies, leaflet velocities, and leaflet stresses. Although this domain also contains the aortic root and the sinuses, the most accurate and available data exists for the leaflets. This is likely due, as one may recall from the literature review, to the fact that the leaflets are more prone to tearing and calcification compared to the surrounding areas and that bioprosthetics contain only the leaflet structures.

2.4.1.a Leaflets morphologies and dynamics

Looking from the position of the ascending aorta back towards the left ventricle, known as the short-axis view, allows the observer to see some key features. The shape of the orifice, the opening and closing features of the aortic valve, the cusps and aortic wall instantaneous motion pattern and dynamics during the different phases of the cardiac cycle have a clinical implication and can be quantified clinically. Figure 2.6 presents the computed leaflets morphologies at six discrete opening and closing times of the cardiac cycle. Values were in good agreement with previous studies and the valve opens to 78% of the cross-sectional area of the aortic ring [61]. Also, the

calculated commissural expansion was 8.4% compared to the natural values of 12% which is the result of applying the pressure gradient at the level of the ventricle out flow tract [86].

The leaflets opening during the systolic phase was associated with ballooning and tip fluttering, which was similar to clinical and physiological observations [87]. The maximum opening happened at t = 0.12s into the cardiac cycle. These large displacements are the main source of the complexity related to the FSI modeling of the aortic root. Following the maximum opening of the leaflet, the diastolic phase starts by the closure of the valve and the returning to its initial configuration. Since after complete closure, there was no variation observed in the leaflets morphology, the remaining images of the valve related to the rest of the cardiac cycle were not included in Figure 2.6.

Time	Isometric view	Short axis view
t=0.00 s 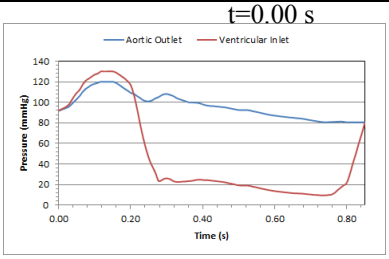	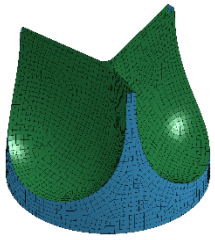	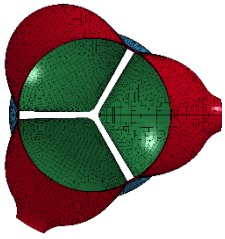
t=0.04 s 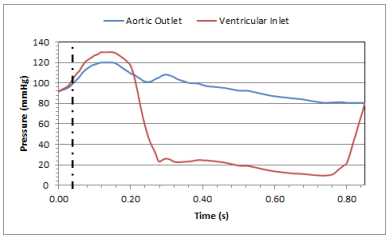	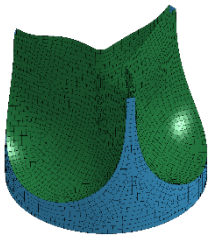	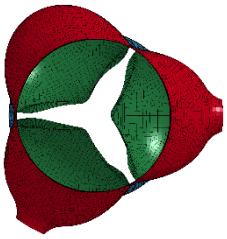
t=0.06 s 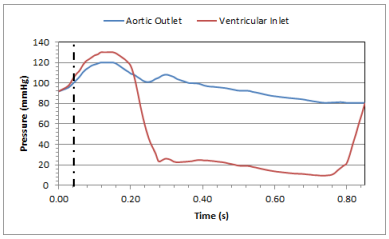	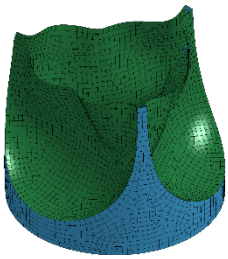	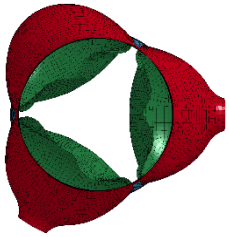

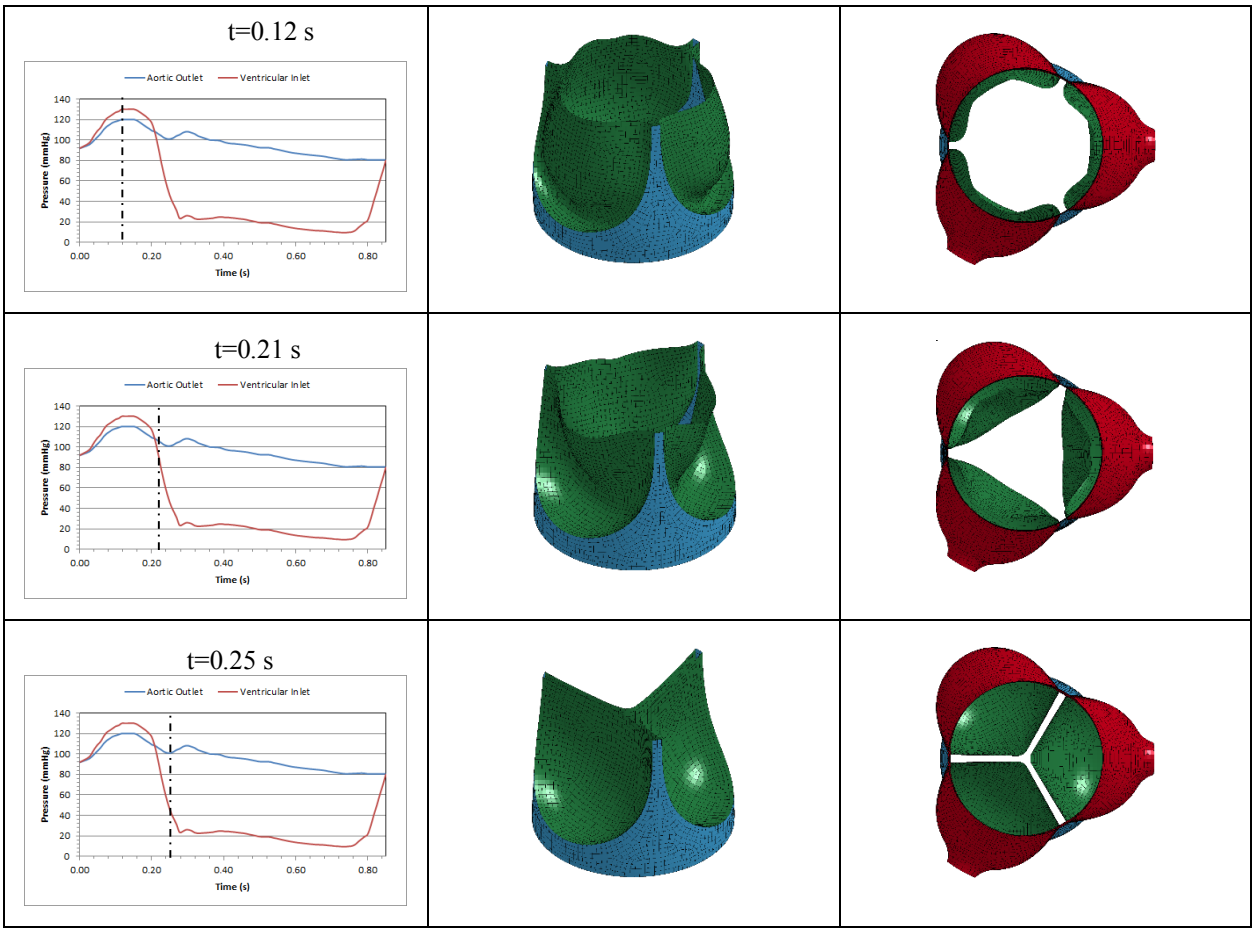

Figure 2.6: The computed leaflets morphologies, seen in isometric and short axis views (The apparent gap in the first frame is due to the shell thickness).

In addition to the examination of the leaflet morphology, the leaflet tips dynamics were examined and the corresponding values of their velocities and accelerations were calculated. The rapid valve opening time (RVOT), rapid valve opening velocity (RVOV), rapid valve closing time (RVCT), rapid valve closing velocity (RVCV), and ejection time (ET) are some common clinical criteria of the leaflets tip velocity histories which are accessible by echocardiography studies [87, 88]. A schematic representation of these parameters is depicted in Figure 2.7.

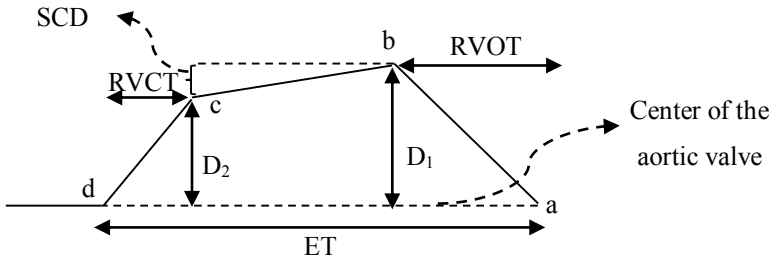

Figure 2.7: Schematic representation of the clinical aspects of the leaflets dynamics: ab = rapid valve opening; bc = slow systolic closure; cd = rapid valve closing; SCD = slow closing displacement, D_1 and D_2=leaflets tip distance from the central axis

The parameters are used in the assessment of the outcome of the valve surgical procedures and the durability of the different prosthetics, and have implication on the coronary flow and left ventricular function. For each of these five indices, average, healthy, values have been experimentally and non-invasively determined. In Table 2.2, the values are compared to those derived with the current model in healthy conditions (120/80 mmHg: ΔP = 40 mmHg) which indicates a good match between our results and the echocardiography data reasonably.

Table 2.2: Comparison between FSI and echocardiography leaflet dynamics.

	RVOT (ms)	RVOV (cm/s)	RVCT (ms)	RVCV (cm/s)	ET (ms)
Normal aortic valve model	56	36.4	40	20.9	252
Echocardiography values	57.5 ± 11.3	29.2 ± 8.7	47.0 ± 11.1	23.6 ± 7	324 ± 70

2.4.1.b Leaflets stress pattern

The stress patterns on the aortic leaflets are quite complex and variable during the cardiac cycle. In this section, von-Mises stress in the leaflets is examined for verification. This biomechanical parameter which varies during the cardiac cycle was observed at two instants of the cardiac cycle one at peak systole in which the pressure gradient on the valve was maximum, and the other at diastole when the leaflets were closed and in contact at the commissural level. As it is shown in Figure 2.8, during the systole the maximum stress happens on the attachment line just below the commissures while in diastole, it shifts toward the commissures. This particular arrangement and the calculated magnitude of the stress was in agreement with previous reports and reported stress patterns on the leaflets [62, 89].

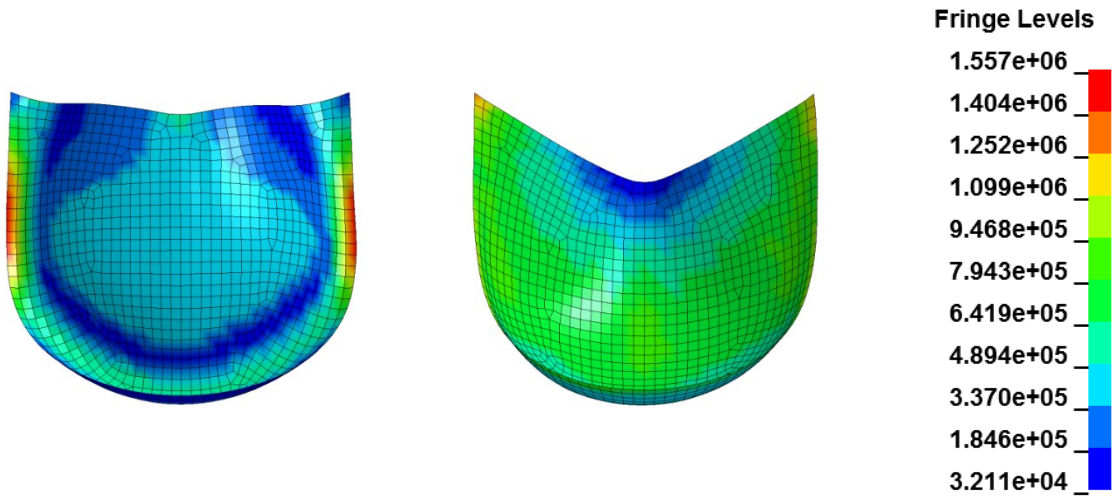

Figure 2.8: Stress distribution on the leaflets during systole (left) and diastole (right) (The unit of stress values is dyne/cm^2).

2.4.2 The fluid domain

The resulting blood flow across the valve is visualized on Isosurfaces during the early systolic phase of the cardiac cycle in Figure 2.9. In order to verify the results in the fluid domain, the calculated flow parameters were compared to the known physiological data. Recirculation regions in the sinuses during the early diastole were validated quantitatively.

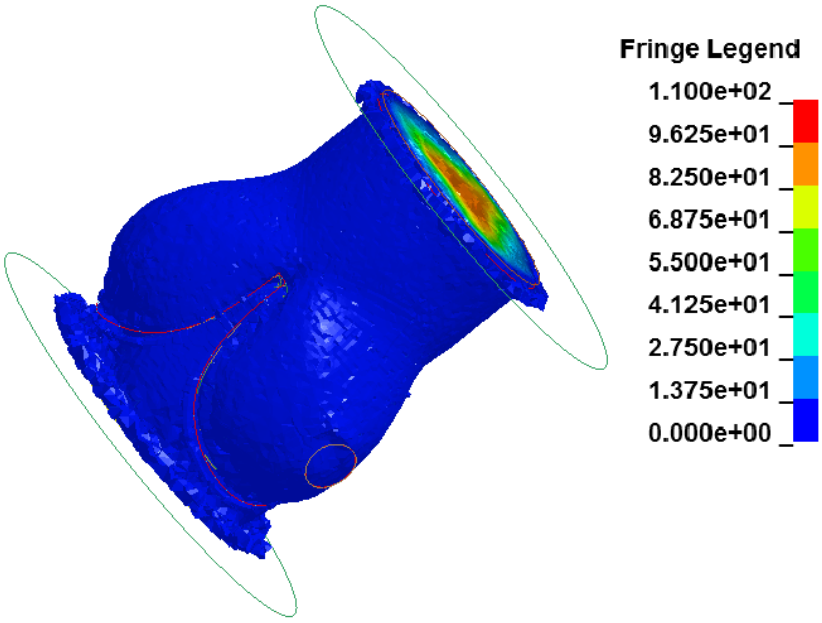

Figure 2.9: Visualized blood flow through the normal aortic valve at t=0.09 s into the cardiac cycle (The unit of velocity is cm/s).

The blood velocity is a very interesting validating biomechanical parameter as it is possible to obtain precise non-invasive measures of its characteristics by MRI. Hence, as a quantitative verification, the blood velocity was calculated at the level of the commissures as well as the sinotubular junction (STJ) which are provided in Figure 2.10. The peak value of the calculated velocity was 1.43 m/s occurring at 0.15 s, which is in agreement with previous studies that have reported peak velocities of 1.35 ± 0.35 m/s [47]. The fluid displays an acceleration which is followed by a deceleration and then a return to a magnitude near zero during the diastolic phase similar to the physiological case. As depicted in Figure 2.10, there was no negative values of flow which is an indication of proper valve closure reflecting no backflow into the ventricular chamber which confirms the full contact between the leaflets during the diastolic phase of the cardiac cycle.

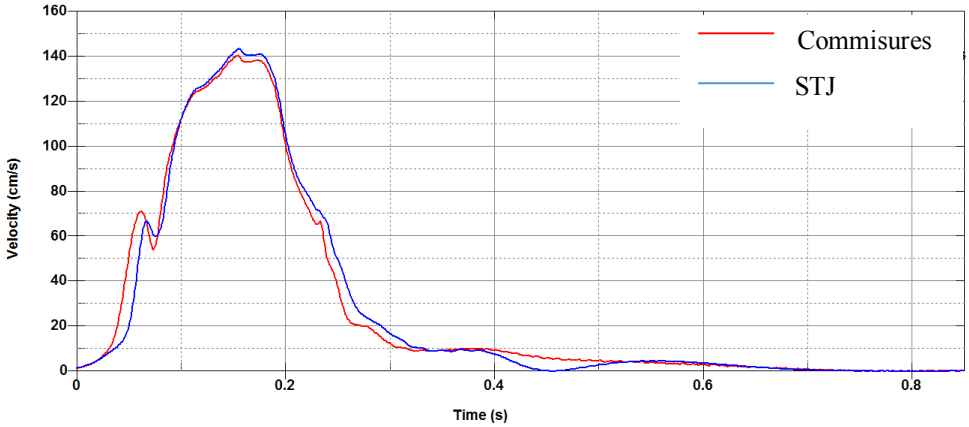

Figure 2.10: The waveforms of the blood flow velocity during a cardiac cycle at sinotubular junction (STJ) and commissure

Diastolic recirculation regions (vortices) in the sinuses during the closure stage of the normal valve is another verifying feature [90]. For the current model, this feature was clearly obtained as shown in the velocity vector plots of the at time t = 0.221 sec, Figure 2.11.

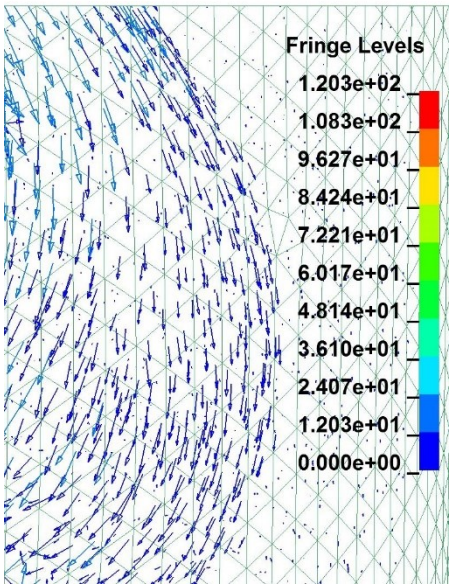

Figure 2.11: Velocity vectors representing the vortex formation around the leaflet tip in the left aortic sinus area (The unit of velocity values is cm/s).

2.5 Discussion

The presented FSI model of the aortic valve was solved by implementation of the strongly coupled scheme in LS-DYNA. The key features of this model are: 1. three-dimensionality, 2. anatomical geometry 3. fully coupled fluid-structure interaction, 4. Implementation of combined ALE and FD approach and 5. application of appropriate boundary conditions in both domains to mimic a natural aortic valve. A simplification was made for definition of the material property by using linear material property for the cardiac tissue. However, as discussed in section 2.3.3, it is shown to be an acceptable approximation. There was no instability problem in the course of the cardiac cycle and the model was run completely without any numerical crash. The obtained results were verified qualitatively and quantitatively in both domains and were in good agreement with previous numerical and clinical data. This normal model of the aortic root has the potential to investigate the effect of the aortic valve diseases on the hemodynamic condition in the aortic root. In the next chapter this model is be used to in verification of the pressure gradient equation through a stenotic valve.

Chapter 3: Derivation of a simplified relation for assessing aortic root pressure drop incorporating wall compliance

3.1 Overview

As discussed in sections 1.1.2.c and 1.1.2.d, aging and certain pathologies such as arterial hypertension, diabetes, hyperglycemia, hyperinsulimenia can cause geometrical and mechanical changes in the aortic valve microstructure which contribute to the development of aortic stenosis (AS). Because of the associated high rate of mortality and morbidity, assessing the impact and progression of this disease is essential. Systolic transvalvular pressure gradient (TPG) and the effective orifice area (EOA) are commonly used to grade the severity of valvular dysfunction. In this chapter a theoretical model of the transient viscous blood flow across the aortic stenosis is derived by taking into account the aorta compliance. The derived relation of the new TPG is expressed in terms of clinically available surrogate variables (anatomical and hemodynamic data). The proposed relation includes empirical constants which need to be empirically determined. We used the developed normal aortic valve model (Chapter 2). The relation was evaluated using clinical values of pressure drops for cases for which the modified Gorlin equation is problematic (low flow, low gradient aortic stenosis).

3.2 Introduction

In aortic stenosis (AS) calcified nodules on the valve leaflets occur which lead to the thickening and stiffening of the leaflets, restricting the natural motion of the valve [91-93]. As a consequence of the obstruction to the blood flow caused by the stenosis, the hydraulic resistance increases. Therefore, high systolic pressure is needed to maintain the necessary cardiac output which may lead to left ventricular hypertrophy which eventually can result in heart failure. Because of the high rate of mortality and morbidity due to the aortic stenosis, assessing its stage and severity is important for the clinician [94-96].

In the management of patients with AS, the first consideration to perform corrective surgery is made largely on the presence or absence of symptoms. In addition, the severity of the AS plays a key role in determining which patients should undergo valve replacement. Systolic transvalvular pressure gradient (TPG) and the effective orifice area (EOA) are commonly used to grade the severity of the valvular dysfunction [96]. These parameters can be assessed using either

catheterization or Doppler echocardiography [97, 98]. However, the current models are problematic under certain conditions. Because of the role of compliance (windkessel effect), it is hypothesized that the incorporation of compliance can improve the pressure estimate.

Numerous experimental and analytical studies have been done to relate the TPG across the stenosis to the blood flow rate and EOA. In one of the first studies, based on fundamental hydraulics, Richard Gorlin and his father developed a formula that can be used to estimate the effective orifice area (EOA) of the stenotic valves and relate the pressure difference and flow through the valve. The frictional effect of the blood flow were not incorporated on the pressure loss [99]. Young and Tsai, by doing an extensive series of model tests, simulated the arterials stenosis and derived the empirical constants of their proposed equation. The obstructed geometry is more diffuse than AS and to the best of the authors knowledge was not transposed to AS [100, 101]. By considering the flow friction, Clark presented a detailed analysis of the instantaneous pressure gradient across the aortic valve. In his study, for simplicity, the contribution of the aortic wall distensibility was neglected. Although the derived equation was validated with animal experimentations, it was not translated to clinic [102]. By using the generalized Bernoulli equation for a rigid wall, several studies investigated the pressure gradient dependency on the blood flow rate and the obstructed area [103-105]. However, the first explicit model of the transvavular pressure gradient was proposed by Garcia et al. They developed an analytical model for the frictionless blood flow across rigid aorta which has clinical potential [106]. For simplicity, none of these studies considered the effect of the aortic root compliance on TPG. Again, the objective of this chapter is assessing the aortic pressure drop for the transient viscous blood flow across the aortic stenosis, by taking into account the vessel wall compliance.

As mentioned in section 2.2, in most of the previous numerical studies of the aortic valve, the objectives were to reproduce the valve dynamics to study alteration to geometrical and hemodynamic parameters and derive the stress patterns. A few studies have been done for making these engineering results meaningful for physicians in terms of diagnostic and prognostic assessment. For this, it is required to map the engineering variables into clinical indices based on anatomical and hemodynamic data called surrogate variables (velocity, shear stress, elasticity, pressure gradient, thickness, and dimensions). More specifically anatomical data include: wall and valve morphologies, wall and leaflet thickening, wall thinning, dilation of the aortic valve, and the hemodynamic surrogate variables include: pressure drop, flow rate, back flow, leaflet stiffening

and dynamics. In this chapter, we use the proposed FSI model of the normal aortic valve. Then, stenoses with different severities are introduced. Finally, the derived TPG is expressed in terms of the surrogate variables and the numerical model is used to extract the empirical constants. Finally the model is assessed using real clinical data.

3.3 Analytical model of blood flow across AS

To derive an expression for the instantaneous transvalvular pressure gradient, a two dimensional model of the blood flow from the left ventricle through the aortic root is used (Figure 3.1). The cross section at any position, x is assumed to be circular. The blood is assumed to be incompressible and the vessel walls are linear elastic.

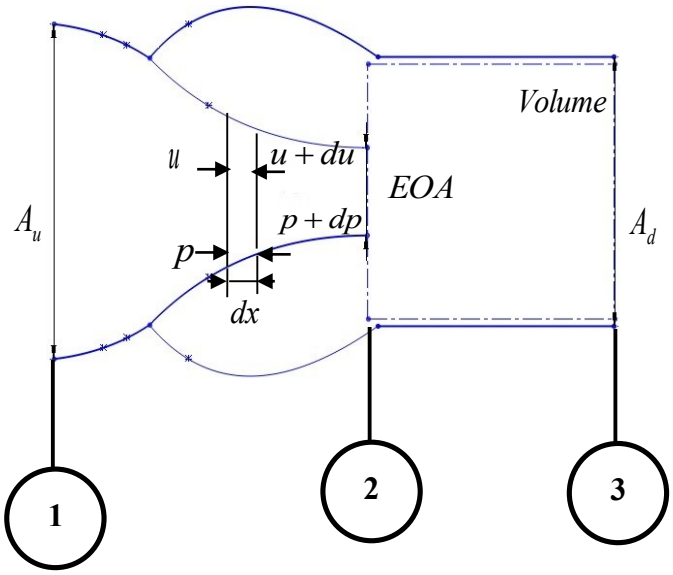

Figure 3.1:A schematic of blood flow from the left ventricle to the aorta across stenotic aortic valve, A_u : Cross sectional area of fluid upstream of the stenosis, EOA : effective orifice area, A_d : Cross sectional area of the fluid downstream of the stenosis.

Upstream of the stenosis, the flow accelerates due to the obstruction presented by the stenosis which results in a jet with its smallest diameter at the vena contracta (EOA). During this convective acceleration, the pressure is converted to kinetic energy. In this process the pressure loss is minor. After passing through the stenosis, the flow expands and fills the cross section of the ascending aorta and decelerates. This decelerating process leads to recirculation and energy losses [107]. Applying Newton's second law to an elemental disk of width dx as shown in Fig.1, yields [102]:

$$-\partial p/\partial x = \rho\,\partial u/\partial t + \rho u\,\partial u/\partial x + 4\tau/d \tag{3.1}$$

where ρ is the blood density, d the diameter, p the pressure, u the velocity, and τ the viscous shear stress. For simplicity, the velocity and pressure vary with position and time while τ is assumed to be dependent only on time. Integrating equation (1) relates the variables to the pressure difference as follows:

$$-\Delta p = \underbrace{\rho\int(\partial u/\partial t)dx}_{\Delta p_L} + \underbrace{\rho\int(u\,\partial u/\partial x)dx}_{\Delta p_C} + \underbrace{4\int(\tau/d)dx} \tag{3.2}$$

The first term on the right side, ∇p_L, represents the pressure loss due to instantanous acceleration. The second term, ∇p_C, is the pressure loss because of the convective acceleration and the last term, ∇p_V corresponds to the viscous force. In this study, it is assumed that the contribution of the inertial, frictional and wall distensibility terms in the transvalvular pressure gradient are linear and will be analyzed separately. For this purpose, initially, the effect of the instantanous and convective terms are first taken into account and the effect of the viscosity and compliance will be analyzed in the subsequent sections.

3.3.1 The effect of fluid inertia

In order to derive the relationship between the pressure gradient and flow, the model is split into two sections. Section one is upstream of the stenosis, from location 1 in Figure 3.1, to the orifice area (location 2 in Figure 3.1). Section two begins from location 2 and ends at location 3, downstream of the stenosis where the reattachment of the flow to the vessel wall occurs. In a first approach, it is assumed that the velocity profile is uniform, the walls are rigid and the fluid is inviscid. Using equation (3.2) for section one, yields:

$$p_u - p_2 = \rho\int_1^2 \frac{\partial u}{\partial t}dx + \frac{\rho}{2}(u_2^2 - u_u^2) \tag{3.3}$$

If the wall is assumed to be indistensible, then the continuity yields $Q = u_u A_u = u_2 EOA = u_d A_d$. So, for rigid walls, equation (3.3) can be rewritten as:

$$p_1 - p_d = \rho\frac{\partial Q}{\partial t}\int_{x_1}^{x_2}\frac{dx}{A} + \frac{\rho}{2}Q^2\left(\frac{1}{EOA^2} - \frac{1}{A_u^2}\right) \tag{3.4}$$

In section two, from the orifice area to a point downstream of the stenosis, the flow can be disturbed and turbulent. For analysis of this section, the control volume method is useful. The acting forces on a fixed control volume Ω with Γ as boundary can be expressed as [106, 108]:

$$\rho\int_{\Omega}\frac{\partial\vec{V}}{\partial t}\,d\Omega+\rho\int_{\Gamma}\vec{V}\vec{V}.\vec{n}\;d\Gamma=\sum\vec{F} \tag{3.5}$$

where $\vec{V}$ is the fluid velocity vector, $\vec{n}$ is normal vector to the surface and $\vec{F}$ are the body and surface forces acting on the control volume. Neglecting the viscous forces and using equation (3.5) for the dashed volume control shown in Figure 3.1, gives:

$$(p_2-p_d)A_d=\rho\frac{\partial Q}{\partial t}\int_{x_2}^{x_3}dl+\rho Q(u_d-u_2) \tag{3.6}$$

Using continuity equation simplifies equation (3.6) as follows:

$$p_2-p_d=\rho\frac{\partial Q}{\partial t}(\frac{L_{23}}{A_d})+\frac{\rho Q^2}{A_d}(\frac{1}{A_d}-\frac{1}{EOA}) \tag{3.7}$$

where, L_{23} is the distance from the location 2 to the location 3. Summing equations (3.4) and (3.7) gives:

$$p_u-p_d=\rho\frac{\partial Q}{\partial t}(\frac{L_{23}}{A_d}+\int_{x_1}^{x_2}\frac{dx}{A})+\frac{\rho Q^2}{2}\left[(\frac{1}{EOA}-\frac{1}{A_d})^2+(\frac{1}{A_d^2}-\frac{1}{A_u^2})\right] \tag{3.8}$$

where the first and second terms on the right side of equation correspond to Δp_L and Δp_C in equation (2), respectively

Garcia et al [106] used dimensional analysis and curve fitting to replace the integral terms. In this study, a similar analysis is done. By defining the parameter λ as:

$$\lambda=\frac{L_{23}}{A_d}+\int_{x_1}^{x_2}\frac{dx}{A} \tag{3.9}$$

and taking into account that the flow geometry and position of location 3 and consequently L_{23} depends mainly on the ratio of EOA and A. It is meaningful to express λ in terms of EOA and A_d. A dimensional analysis provides:

$$\lambda\sqrt{A_d}=g(\frac{A_d}{EOA}) \tag{3.10}$$

In order to determine the function g, it should be considered that according to equation (3.9), when EOA approaches zero (stenosis becomes severe) λ tends toward $+\infty$. In addition, when the

stenosis approaches toward the non-stenotic case, location 3 tends toward location 1 and consequently λ, tends to zero. A simple function g coherent with these two criteria is:

$$\lambda\sqrt{A_d} = \zeta(\frac{A_d}{EOA} - 1) \tag{3.11}$$

where ζ is an empirical constant. Then the net pressure drop becomes:

$$p_u - p_d = \rho\zeta\frac{1}{\sqrt{A_d}}\frac{\partial Q}{\partial t}(\frac{A_d}{EOA} - 1) + \rho k_c\frac{Q^2}{2}\left[(\frac{1}{EOA} - \frac{1}{A_d})^2 + (\frac{1}{A_d^2} - \frac{1}{A_u^2})\right] \tag{3.12}$$

the first term is the pressure loss due to local inertia and the second term represents the pressure loss caused by kinetic terms in the sudden expansion from the orifice area to the aorta. The introduced coefficient k_c to this term is an empirical constant which need to be evaluated

3.3.2 The effect of viscosity

The friction contribution in pressure loss is difficult to evaluate. Clark suggested to use the equation of shear force experienced by a flat plate oscillating in a viscous fluid for the pulsatile flow across the valve which can be expressed as:

$$\tau = \sqrt{\frac{\rho\mu\omega}{2}}u \tag{3.13}$$

where μ is the dynamic viscosity, and ω is the heart frequency [102, 109]. Viscosity contribution to the pressure in the fluid flow, Δp_V , across any vessel with circular cross section is presented by the last term of equation (3.2). Therefore, by substituting equation (3.13) in equation (3.2) and using the continuity equation for a circular section, pressure loss due to the viscosity can be expressed as:

$$\Delta p_V = \rho k_v\frac{L_{13}}{EOA^{3/2}}\sqrt{\nu\omega}\,Q \tag{3.14}$$

where, k_v is an empirical constant and L_{13} is the distance from location 1 to location 3.

3.3.3 The effect of vessel wall compliance

For the fluid flow across a distensible wall, the flow rate, Q, varies with distance because of the transient storage of fluid associated with the distensible boundary [102, 110]. The variation of the flow rate with distance due to the compliant walls will influence all terms in the right hand side of equation (3.2). The main influence of compliance on the pressure drop is related to additional convective pressure loss due to the post stenotic dilatation of the aorta resulting from flow disturbances in this region [111]. For simplicity, since the convective pressure term has the highest

contribution on the pressure loss [102], in this study, only the changes in this term due to the wall distensibility is analyzed. This effect can be calculated from the last term in equation (3.12) compared to the same conditions for the non-distensible case. Since the area of the ventricle outflow tract is of the same caliber as the aorta, the last parenthesis can be neglected. For a distensible wall with fixed EOA, flow disturbance downstream of the stenosis causes a change in the cross sectional area by an amount dA.Then for the compliant vessel the convective pressure loss becomes:

$$\Delta p_C = \frac{\rho Q^2}{2A_d^2}\left(\frac{A_d + dA}{EOA} - 1\right)^2 \tag{3.15}$$

If the vessel is modeled with a thin walled cylinder obeying Hooke's law (assuming physiological deformation), since the longitudinal stress is much smaller that the circumferential one, then

$$e_{\theta\theta} = \frac{da}{a} = \frac{adp}{Eh} \tag{3.16}$$

Where $e_{\theta\theta}$ is the circumferential strain, a the radius of the vessel, a_0 the initial radius, E the Young's modulus of the wall material and h the wall thickness. Then, the cross sectional variation in equation (3.15) can be expressed as:

$$dA = \frac{2A_d\sqrt{A_d}}{\sqrt{\pi}}\frac{dp}{Eh} \tag{3.17}$$

Hence, by expanding equation (3.15), neglecting the higher order terms and using equations (3.16) and (3.17), the effect of the wall compliance in pressure loss can be expressed as:

$$\Delta p_C = \Delta p_{Rigid} + \Delta p_{Co} = \frac{\rho Q^2}{2}\left[\left(\frac{1}{EOA} - \frac{1}{A_{AO}}\right)^2 + \frac{4\sqrt{A_d}\,dp}{Eh\sqrt{\pi}}\left(\frac{1}{EOA}\right)\left(\frac{1}{EOA} - \frac{1}{A_d}\right)\right] \tag{3.18}$$

The first term in the right hand side (Δp_{Rigid}) is the pressure loss caused by convective inertia in the rigid vessel, while the second term (Δp_{Co}) corresponds to the contribution of the vessel compliance to convective pressure loss:

$$\Delta p_{Co} = 2\rho Q^2 \frac{\sqrt{A_d}\,dp}{Eh\sqrt{\pi}}\left(\frac{1}{EOA}\right)\left(\frac{1}{EOA} - \frac{1}{A_d}\right) \tag{3.19}$$

Where dp is the pressure variation in the aorta. This term can be scaled as a fraction of the pulse pressure by introducing an empirical constant k_p which has the dimension of the pressure.

Hence, by including the effect of all constant coefficients of equation (3.19) in k_p, it can be simplified as:

$$\Delta p_{Co} = \frac{\rho k_p Q^2}{Eh}\left(\frac{\sqrt{A_d}}{EOA}\right)\left(\frac{1}{EOA} - \frac{1}{A_d}\right) \tag{3.20}$$

3.3.4 Global pressure drop across the aortic valve

The instantaneous global transvalvualar pressure gradient can be then expressed as:

$$p_u - p_d = \Delta p_V + \Delta p_C + \Delta p_L + \Delta p_{Co} \tag{3.21}$$

substituting equations (3.12),(3.14) and (3.20), equation becomes:

$$p_u - p_d = \rho k_v \frac{L_{13}}{EOA^{3/2}}\sqrt{\nu\omega}\, Q + \rho k_c \frac{Q^2}{2}\left[\left(\frac{1}{EOA} - \frac{1}{A_d}\right)^2 + \left(\frac{1}{A_d^2} - \frac{1}{A_u^2}\right)\right] + \rho\zeta \frac{1}{\sqrt{A_d}}\frac{\partial Q}{\partial t}\left(\frac{A_d}{EOA} - 1\right) + \frac{\rho k_p Q^2}{Eh}\left(\frac{\sqrt{A_d}}{EOA}\right)\left(\frac{1}{EOA} - \frac{1}{A_d}\right) \tag{3.22}$$

where k_v, k_c, ζ and k_p are empirical constants.

3.4 Aortic stenosis models

Equation (3.22) includes empirical parameters which need to be evaluated. This can be done with simulated, experimental or clinical data. In the first approach, we used the developed 3D FSI numerical model (chapter 2) to generate data for their determination. To achieve this goal, as illustrated in Figure 3.2, by constraining the motion of leaflets tip, five stenosis models with different severity were created. While, the percentage of the reduction in the area occupied by blood from the left ventricle out tract to the orifice is used as an index to evaluate the stenosis severity.

3.5 Results

For all models, the heart rate was fixed at 74 bpm. A section view of the blood velocity vector at 0.12s into the cardiac cycle during which the blood velocity in the left ventricle is maximum, for healthy and stenosed models with severity of 79%, is presented in Figure 3.3.

All of the six models, including the healthy model, were simulated with four distinct cardiac outputs of 3, 4, 5 and 6 L/min. Then, by measuring TPG, blood flow rate, rate of change of the blood flow rate, EOA, all corresponding terms in equation (3.22) were evaluated. Therefore, a system of twenty four linear equations were generated which can be expressed in matrix form as:

$$\boldsymbol{MK} = \boldsymbol{\Delta p} \tag{3.23}$$

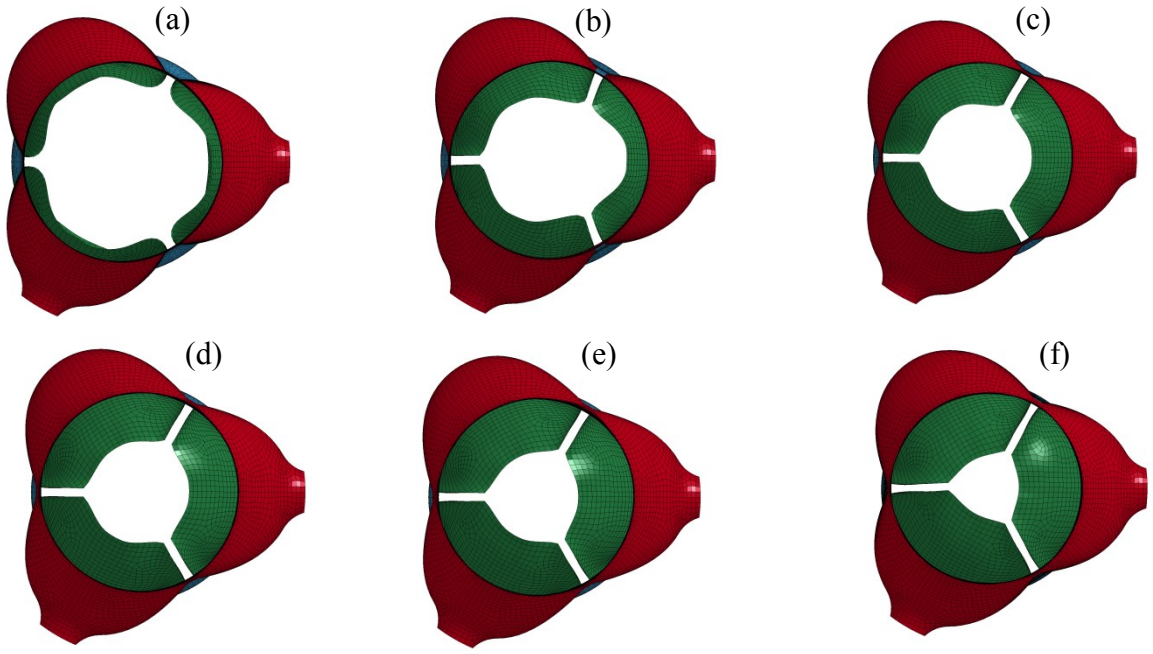

Figure 3.2: Schematic of the created models in their maximum opening state: a): Healthy model, b): Stenosis with severity of 61%, c): Stenosis with severity of 72%, d): Stenosis with severity of 79%, e): Stenosis with severity of 84%, f): Stenosis with severity of 92%

where $\boldsymbol{M}$ is a 24×4 matrix whose rows are the calculated terms on the right hand side of equation (3.22). $\boldsymbol{K}$ is the matrix of the empirical constants with dimension of 4×1 and $\boldsymbol{\Delta p}$ is a 24×1 matrix of the measured TPG corresponding to each model. Since $\boldsymbol{M}$ is a non-square matrix, a Moore-Penrose pseudo inverse approach is used to invert the resulting over-determined system of linear equations. The approach that was proposed by Moore (1920) and Penrose (1955) aims to compute the least squares solution to a system of linear equations which lacks a unique solution [112]. According to this method, the generalize inverse of matrix $\boldsymbol{M}$ in equation (3.23) is defined as $(\boldsymbol{M}^T\boldsymbol{M})^{-1}\boldsymbol{M}^T$, where $\boldsymbol{M}^T$ denote the transpose of $\boldsymbol{M}$. Hence, the empirical constants can be calculated using the following equation.

$$\boldsymbol{K} = (\boldsymbol{M}^T\boldsymbol{M})^{-1}\boldsymbol{M}^T \tag{3.24}$$

The calculated values for k_v, k_c, ζ and k_p are presented in Table 3.1.

Table 3.1: Values of derived empirical constants

Parameter	k_v	k_c	ζ	k_p
Calculated value	20.05	0.79	6.89	-82162 dyne/cm^2

The overall square root error of the approach was 0.0965. Therefore the derived global transvalvular equation can be rewritten as:

$$p_u - p_d = 20.05\rho \frac{L_{13}}{EOA^{3/2}}\sqrt{\nu\omega}\,Q + 0.79\rho\frac{Q^2}{2}\left[\left(\frac{1}{EOA}-\frac{1}{A_d}\right)^2 + \left(\frac{1}{A_d^2}-\frac{1}{A_u^2}\right)\right] + 6.89\rho\frac{1}{\sqrt{A_d}} \quad (3.25)$$

$$\frac{\partial Q}{\partial t}\left(\frac{A_d}{EOA}-1\right) - 82162\,\frac{\rho Q^2}{Eh}\left(\frac{\sqrt{A_d}}{EOA}\right)\left(\frac{1}{EOA}-\frac{1}{A_d}\right)$$

(a) (b)

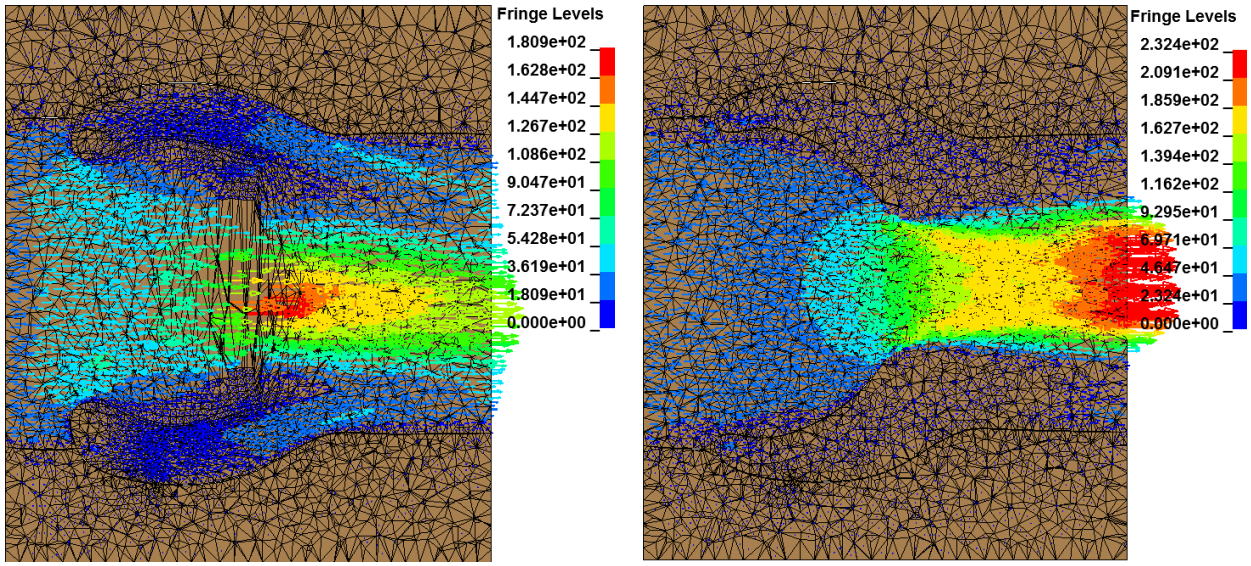

Figure 3.3: Blood velocity vector over the leaflets at 0.12s into the cardiac cycle in a): Healthy model b): Stenosis with severity of 79%

The temporal average of pressure drop calculated from equation (3.25) is compared with results of studies done by Gorlin,Garcia et al and Clark for a fixed flow of 5L/min in Figure 3.4.a and for a fixed EOA of 0.85 cm^2 in Figure 3.4.b. Also the impact of stenosis severity and blood acceleration for the global pressure drop is shown in Figure 3.5.a. The relative contribution of wall compliance to global pressure gradient for as a function of EOA for different cardiac output is presented in Figure 3.5.b.

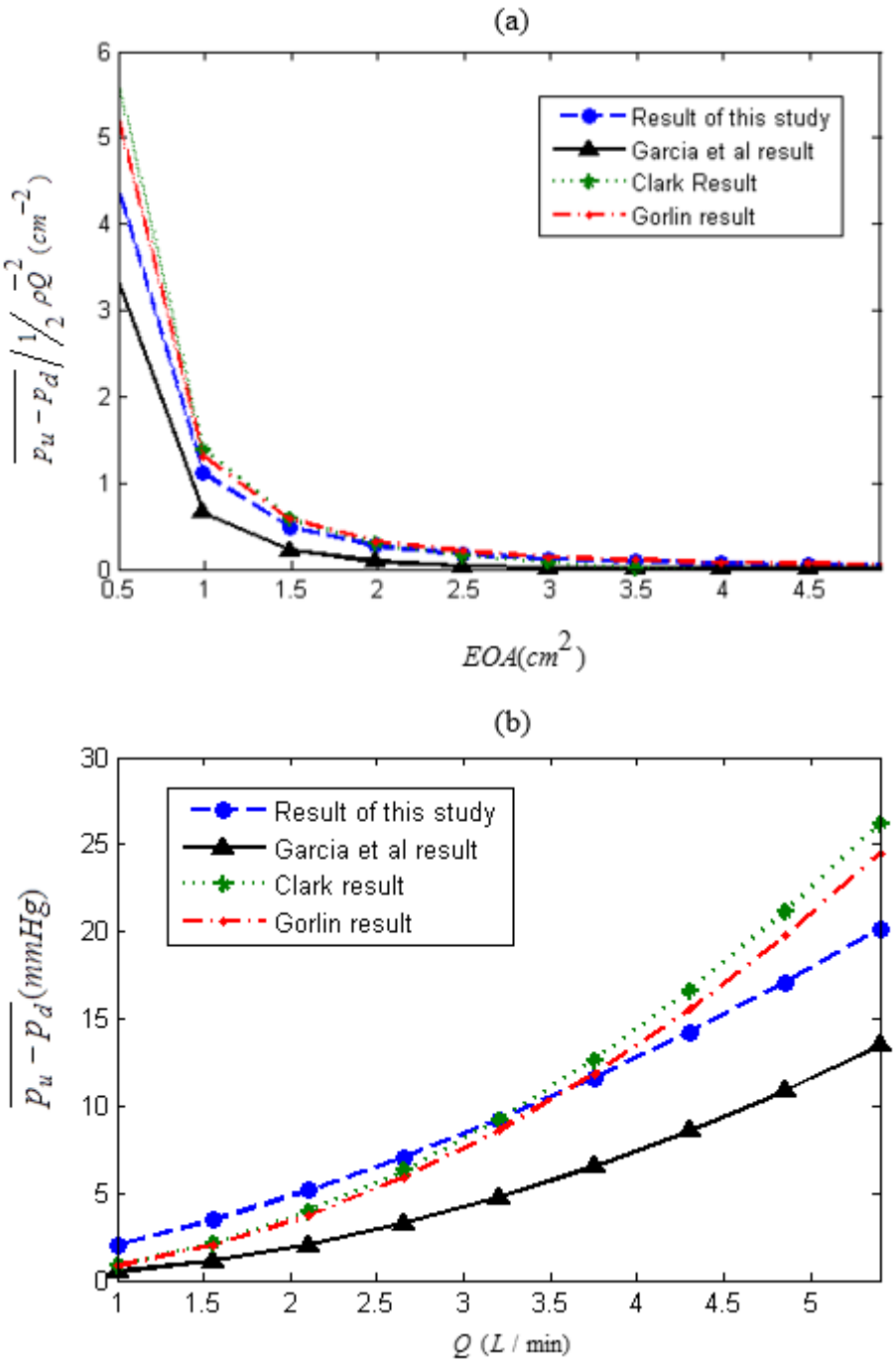

Figure 3.4: a):Temporal mean of pressure drop calculated from equation (3.25), Gorlin,Garcia et al and Clark study results for cardiac output of 5L/min, b): Pressure drop predicted from Our result, Gorlin, Garcia et al and Calrk study as a function of flow for a fixed EOA of 0.85cm^2, for all cases, heart rate is 74bpm and $A_u = A_d = 4.91\,cm^2$.

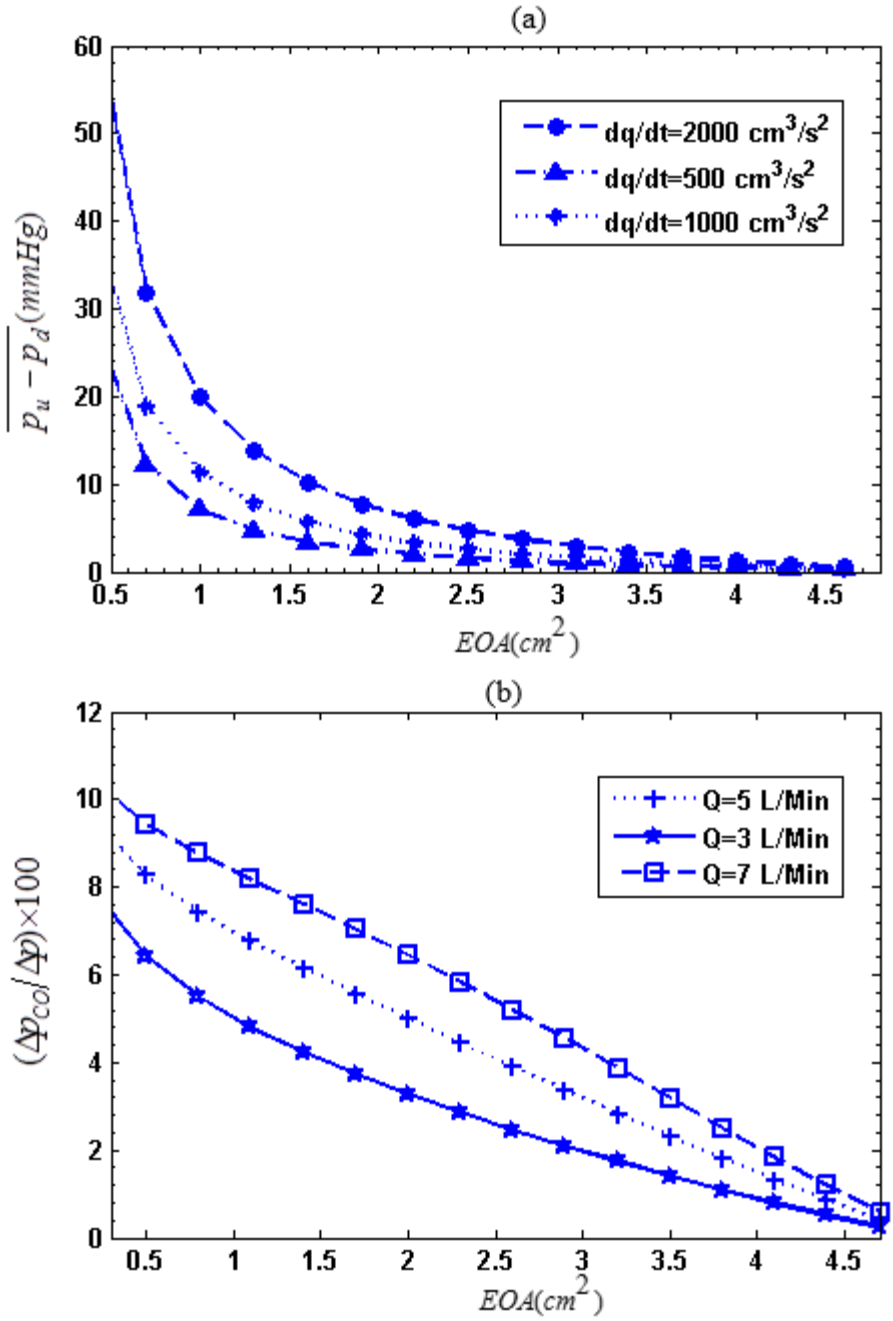

Figure 3.5: Global pressure drop for selected values of flow acceleration. d): Percentage of pressure loss due to vessel wall compliance to total pressure gradient, for all cases, heart rate is 74bpm and $A_u = A_d = 4.91\,cm^2$.

3.6 Discussion

A global relation of TPG that takes into account geometrical and hemodynamic parameters including the vessel wall compliance was derived. A numerical model incorporating an anatomical 3D geometrical model of the aortic root with the sinuses of Valsalva was used for its parameters.

The calculated values for the empirical constants of equation (3.22) are listed in Table 3.1. Therefore the pressure drop across a compliant wall is expressed by equation (3.25). The first term on the right hand side of this equation corresponds to frictional loss, the second term takes into account the pressure loss due to convective acceleration, the third term is responsible for local inertia of the blood flow, and the last term is the pressure loss related to the dilation of the compliant vessel. As it was discussed, Gorlin developed a formula that can be used to estimate the effective orifice area (EOA) of the stenotic valves and relate the pressure difference and flow through the valve:

$$\Delta p = \frac{1}{2}\rho Q^2 \frac{1.28}{EOA^2} \tag{3.26}$$

this formula was derived with the assumptions of a rigid circular conduit, non-viscous and steady flow, however valvular orifices are compliant and the flow is viscous and pulsatile. It is reported that deviation for the calculated area by this formula increases under the following conditions: 1) Low flow rate, and 2) Small area [113, 114]. As presented in Figure 3.4.a, the pressure drop calculated from our study for stenoses of different severities through which a fixed amount of flow (5L/min) is passing, is higher than the Gorlin result while for a fixed size stenosis (Figure 3.4.b), our results yield higher values of pressure gradients for lower flow rate.

Based on a theoretical model, Clark proposed the following equation for TPG:

$$\Delta p = \rho \frac{Q^2}{2c_d^2}\left[\left(\frac{1}{EOA^2} - \frac{1}{A_u^2}\right) + \frac{2(1 - A_d/EOA)}{A_d^2}\right] + \rho \frac{\partial Q}{\partial t}\int_{A_u}^{A_d} \frac{dx}{A} \tag{3.27}$$

where c_d is the discharge constants to include the frictional effects. His suggested range for discharge constants was 0.8-1. His model includes an integral term for the local acceleration which needs to be expanded for clinical application [102]. The temporal average of pressure drop plotted in terms of EOA for a constant flow in Figure 3.4.a and for a constant EOA as a function of Q in Figure 3.4.b. Hence, the Clark equation is almost superimposed to the Gorlin equation in Figure 3.4.a while there is a small difference for high flow for a fixed EOA (Figure 3.4.b).

Garcia et al used a theoretical model and derived a similar equation for TPG in which the convective and local inertial terms were considered.

$$p_u - p_d = \rho \frac{Q^2}{2}\left[(\frac{1}{EOA} - \frac{1}{A_d})^2 \right] + 6.28\rho \frac{\partial Q}{\partial t}\sqrt{\frac{1}{EOA} - \frac{1}{A_d}} \tag{3.28}$$

They used a dimensional analysis to derive the inertial pressure loss $6.28\rho \frac{1}{\sqrt{A_d}} \frac{\partial Q}{\partial t}(\frac{A_d}{EOA} - 1)^{0.5}$. We have used a similar dimensional analysis with only one parameter for simplicity. The value for our parameter ζ, 6.89 is comparable with the value of their parameter of 6.28. As it is shown if Figure 3.4.a and Figure 3.4.b, the pressure drop calculated from their equation results in lower values as compared to our results. The reason is that they didn't consider the frictional effect. Therefore it underestimated the pressure drop.

In Figure 3.5.a, the net pressure drop calculated from equation (3.25) is presented as a function of the EOA for a normal flow rate of 5L/min for three values of flow acceleration to illustrate the effect of local term. This term is generally neglected in most studies while it is clear from Figure 3.5.b that as the percentage of the stenosis increases, the contribution of the local acceleration to the global pressure drop increase.

The last term, which is the contribution of the aorta compliance to the pressure loss, is the main contribution of this study. As it was discussed before, some assumptions have been used for its derivation. The calculated value for parameter (k_p) is -82162 dyne/cm^2. The contribution of this term to the total pressure gradient for the three selected values of flow is plotted as a function of orifice area in Figure 3.5.a. So, as the flow rate increases, because of more dilation of wall, this term becomes higher and for a normal cardiac output of 5L/min about 10% of the pressure is stored in the wall deformation for the AS with a severity of 84%.

3.7 Conclusion

In this chapter we have derived a theoretical model of the transient viscous blood flow across the aortic stenosis taking into account the aorta compliance. Then by using the developed FSI model of the aortic root, discussed in previous chapter, the derived relation of the new TPG is expressed in terms of clinically available surrogate variables (anatomical and hemodynamic data). The results showed that the proposed relation provides physiologically compatible results even for cases for which current models fail (low flow). The model reveals that for a normal cardiac output

of 5L/min, about 10% of the pressure drop is used to deform the wall for a severe AS while this is neglected in the models. This generalized model can be used to estimate the effective valve orifice area for determining the severity of the stenosis in cases where the tissue still has compliance.

Chapter 4: 3D global Fluid-Structure interaction model of the aortic root with inclusion of coronary arteries

4.1 Overview

The normal aortic root model only allows studying coronary flow while it is insufficient for investigating the impact of the regional pathologies of the aortic root on velocity distribution and shear stress downstream in the coronary arteries. The diseases of the coronary arteries and the aortic root are still the leading causes of mortality and morbidity worldwide, however while due to some limitation either by using the medical imaging modalities or numerical simulation still much remains to be elucidated about the importance and relevance of the hemodynamic and geometrical variables on development of diseases in this region of the heart. As a result, in this chapter, a 3D global fluid-structure interaction of the aortic root with inclusion of anatomically inspired coronary arteries using the finite element method is presented. The calculated variables in the solid domain (leaflet morphologies, Leaflets dynamics and leaflets stress) and fluid domain (blood velocity vector, blood velocity profile, coronary blood supply, wall shear stress on the coronary vessels) were assessed both qualitatively and quantitatively.

4.2 Introduction

Throughout the years, numerous studies have been performed on either the aortic valve or the coronary structures. The studies on the aortic valve were mentioned in section 2.2. The numerical studies on the coronary structures have focused on noninvasive flow assessment. In the last 25 years, computational fluid dynamics (CFD) has been widely used to study the blood flow through the coronary arteries [115]. Some early studies used simplified geometries of the right coronary arteries (RCA) or the left coronary arteries (LCA) individually with the assumption of steady laminar flow [116-118]. However, current models are lacking the small branches of the coronary arteries feeding the ventricles [115, 119-121]. In addition, due to the complexity, most of these numerical investigations are limited to the fluid domain. A fluid structure interaction (FSI) simulation is needed to examine the impact of the vessel wall on the blood flow and vice versa.

Due to the large deformations that leaflets experience during the cardiac cycle, numerical modeling of fluid–structure interaction of the aortic valve has proven to be a challenging task. Adding the coronary arteries to the aortic valve model increases this complexity which has limited

the studies of both adjacent structures. Although, few studies have incorporated the aortic valve and the coronary vessels into one numerical model, these conveyed studies, have either neglected FSI nature of the model or used a simplified geometry of aortic valve and coronary structures for simplicity. Verhey et al. employed CFD simulation in order to study the impact of the coronary artery outlet angle variation in artificial aortic root prosthesis. Nevertheless, their model was lacking the leaflets. Gaillard et al. developed an in-vitro version of a previously developed mathematical model of the aortic to examine the impact of stenosis on coronary flow reserve[122]. Recently, Nobari *et al*, by adding the main stem of the left and right coronary arteries to their previously developed aortic valve model, investigated the effect of the leaflets stiffening on the coronary hemodynamics [89]. But, due to the limitation of the computational method they used, the tapering of the vessels was ignored and just the main stem of the coronary vessels without the main bifurcation was modeled.

There are situations in which the occlusion of the small coronary vessels is very important. Examples are those in which the blood supply to the critical parts such as atrioventricular node (AV), the sinus node (SA) and right ventricle out tract is interrupted causing mechanical and electrical instability of the heart and its valves. Consequences of any damage to the small coronary vessels are arrhythmias, conduction disturbances, syncopal attacks and frequently sudden death [123, 124]. While due to the complexity of the FSI simulation, the study of the flow across the small coronary arteries, are neglected in most clinical and numerical investigations.

In addition, recently, it was shown that there can be a bidirectional interaction between the diseases of the aortic root and the diseases of the coronary arteries [125, 126]. While Current studies, have focused on the local modeling of the coronary blood flow rather than a global model of the aortic root including the sinuses, leaflets and coronary arteries. Consequently, there is an obvious demand for such a global model.

Hence the goal of this chapter is to develop the normal aortic valve model to a 3D global model by including the anatomically realistic coronary vessels and their critical small branches using finite element method. Such a global model gives a new insight in to the study of the interdependence between the pathologies of the aortic valve and the coronary vessels, coronary stents, occlusion of the critical small coronary vessels and its effect on the heart muscle and its

electrical nodes supply and also the impact of different pathologies on the WSS pattern on the coronary vessels.

4.3 The anatomical geometry of the coronary structures

In order to include accurate geometrical model of the coronary vessels in the global model, the Zygote Solid 3D Circulatory System (Zygote Media Group, Inc.) model was used. This model was developed using CT scan image slices of perfused individuals to create a 3D polygonal model from the image stack. Data identified by medical modelers as coronary tissue was isolated from surrounding tissue data and compiled into a rough 3D heart template model. Then all anomalies from the template introduced by scanning technology, patient movement and individuality were removed from the model using the using anatomical atlases and research reference data by medical modelers. This model was edited and cut to include only the particular parts and branches of the coronary arteries. These edited structures were later added to the normal aortic valve model created in section 2.3.1. The coronary vessels included in this model are left main stem (LMS), main circumflex (MCx), left atrial circumflex (LAC) and the first posterior circumflex branch (1st PLCx), main left anterior descending (MLAD), left anterior descending (LAD) and diagonal branch of the LAD (DLAD) on the left coronary arteries (LCA) and right main stem (RMS), conus branch (CB), right ventricular branch (RV), and posterior descending (PD) on the RCA. Figure 4.1 presents schematic of the solid domain of the model geometry in different views.

(a)

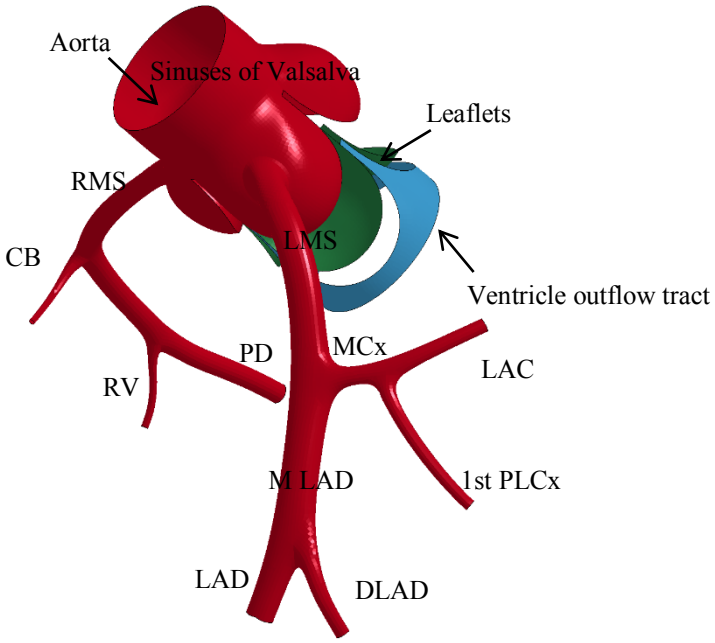

(b)

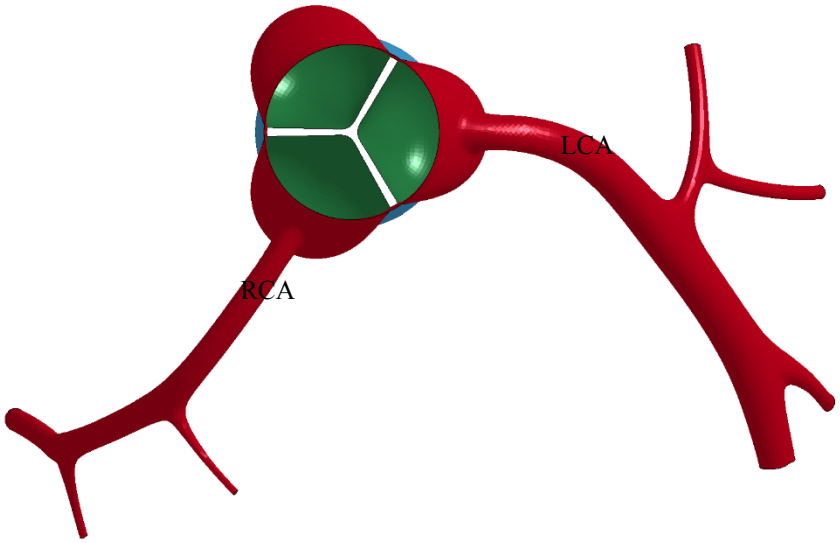

Figure 4.1: **a** Exploded view of the various components of the aortic root model including the coronary arteries, LMS: left main stem, MCx: main circumflex, LAC: left atrial circumflex, 1st PLCx: the first posterior circumflex branch, MLAD: main left anterior descending, LAD: left anterior descending, DLAD: diagonal branch of the LAD, RMS: right main stem, RV: right ventricular branch CB: Conus branch, PD: posterior descending of RCA **b** top view of the model showing the global structure, RCA: right coronary arteries, LCA: left coronary arteries,

The cross sectional areas of the all modeled branches of the coronary arteries, their distances from the ostium measured in the bifurcation site and their function are listed in Table 4.1 which are within the reported range measured by Funabashi et al [127].

Table 4.1: Coronary vessels cross sectional area and distance from the ostium, LMS: left main stem, MCx: main circumflex, LAC: left atrial circumflex, 1st PLCx: the first posterior circumflex branch, MLAD: main left anterior descending, LAD: left anterior descending, DLAD: diagonal branch of the LAD, RMS: right main stem, RV: right ventricular branch, AM: acute marginal artery, PD: posterior descending of RCA

	Vessel type	Area (cm^2)	Distance from ostium (cm)	Anatomy and function
Left Coronary Arteries (LCA)	LMS	0.2845	0	Courses from the left sinus of Valsalva carrying the blood to LCA
	MCx	0.0423	3.150	Arises from the left main coronary artery courses along the left atrioventricular groove
	LAC	0.0402	4.030	Braches of the MCx and supply blood to the left atrium and in 40–50 percent of hearts, the SA node
	1st PLCx	0.0203	4.030	Braches of the MCx and supply blood to the lateral aspect of the left ventricular myocardium and the AV node
	MLAD	0.2024	3.698	Continues directly from the bifurcation of the left main stem branching into LAD and DLAD
	LAD	0.1279	5.229	Continues directly from the bifurcation of the MLAD, coursing in the anterior interventricular groove to the apex of the heart
	DLAD	0.0234	5.229	Course along anterolateral wall of the left ventricle and supply this part of the heart
Right Coronary Arteries (RCA)	RMS	0.1988	0	Courses from the right sinus of Valsalva carrying the blood to RCA
	CB	0.0131	2.798	Arises from the right main coronary artery and supplies the right ventricle outflow tract
	RV	0.0201	5.607	Branches off the right main coronary artery and supplies the right ventricle
	PD	0.0645	5.607	Runs along the posterior interventricular groove, giving off perpendicular branches supplying the left ventricle, right ventricle and the AV node

4.4 Finite element model

Similar to the normal aortic valve model, the constructed geometry were imported into a preprocessing software to be divided into separate parts and then be discretized for implementation of finite element analysis. The preprocessing steps were performed on the solid and fluid domains separately which are discussed in the following sections.

On the solid domain, the selected element type was the same as for the normal aortic valve model described in section 2.3.2.a. Since, an appropriate ratio between the solid and fluid elements is required for achieving convergence, mesh independency tests were performed to ensure convergence and obtain the minimum allowable element size. As a result, 22,650 quadrilateral elements were used for modeling the solid domain. In addition, the constant thickness of 1 mm were assigned for the coronary vessels.

Similarly, In order to assign the different boundary conditions on different parts of the model, the fluid domain was composed of several parts which are presented in Figure 4.2. This domain was composed 549,908 unstructured mesh which was observed to be adequate after performing mesh independency tests.

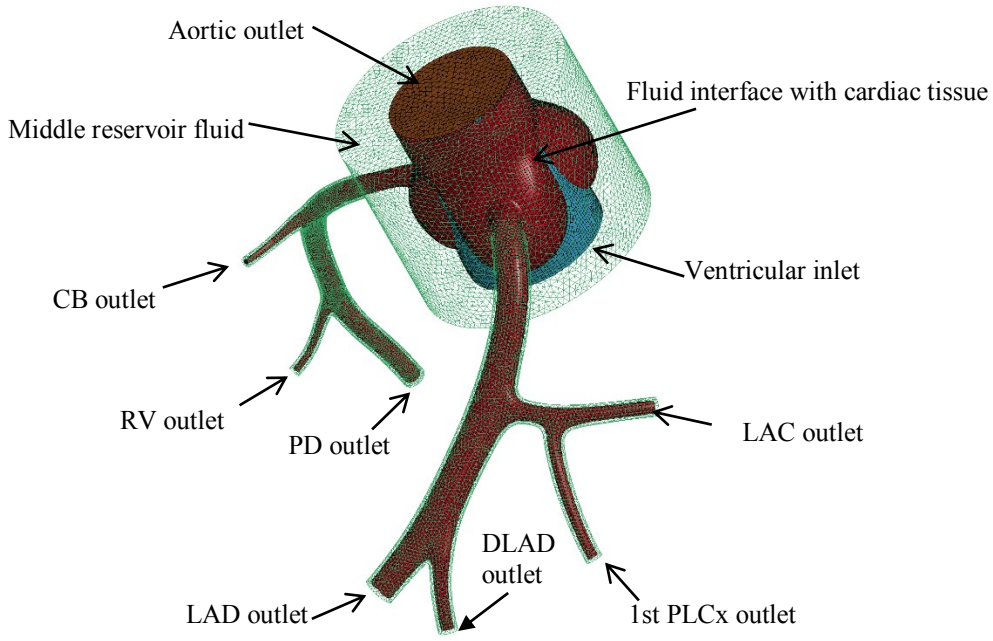

Figure 4.2: The meshed fluid medium including the specified parts to define the boundary conditions and interface with the solid domain

4.4.1 Material properties

On the solid domain, the material property of the leaflets and the aortic wall was similar to the normal aortic valve model, section 2.3.3.a, while for the coronary arteries the assigned material property was the same as the aortic wall. In addition, the blood on the fluid domain modeled using the selected material property for the normal aortic valve model which was discussed in section 2.3.3.b.

4.4.2 Boundary conditions

The applied boundary conditions and loads on each domain will be discussed separately in the following.

On the solid domain, the assigned boundary conditions on the ventricular inlet ring and the aortic outlet ring were the same as the normal aortic valve which was discussed in section 2.3.4.a. While on the coronary structure in order to avoid the issue of instability, movement constraints were applied on the bifurcation sites as well as the branches outlet rings.

On the fluid domain, time dependent physiological values of blood speed on the ventricular inlet corresponding to the cardiac flow of 5.068 L/min (Figure 4.3.a) as well as the difference between the transient physiological blood pressure waveforms corresponding to the outlets of the model, Figure 4.3.b, and the aortic pressure was imposed on the outlets [128]. This method was borrowed from literature to avoid the instabilities issues and reduce extremely the long computation time. The duration of the simulated cardiac cycle is 0.85 s corresponding to a heart rate of 70 beats per minute.

(a)

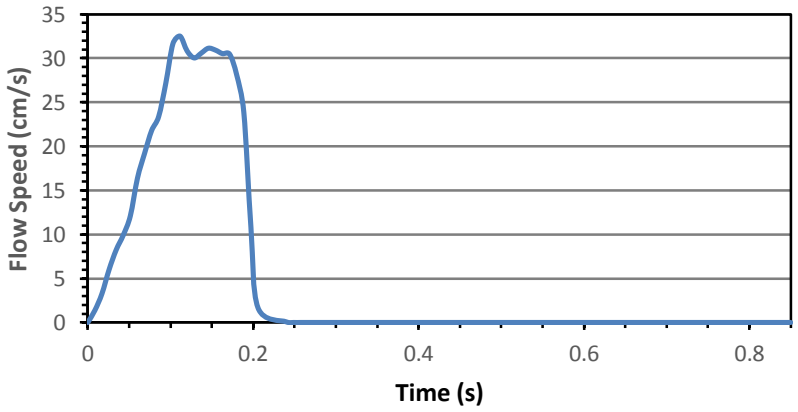

(b)

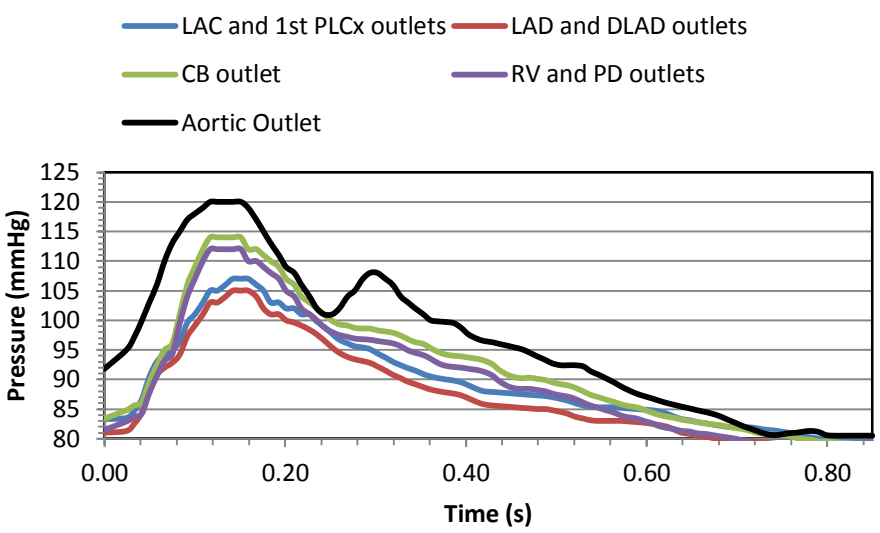

Figure 4.3: The physiological values of the blood speed and pressure at (a): ventricular inlet and (b): outlets of the model

4.5 Results of the global aortic root model simulation

Similar to the normal aortic valve model, the calculated results of running the model in LS-DYNA using the describe method in section 1.2.5 will be presented in the fluid domain and solid domain separately.

4.5.1 The solid domain

The calculated results in terms of the leaflets stress pattern was similar to those of the normal aortic valve which was verified in section 2.4.1.b. Therefore in this section only the leaflet morphologies and dynamics will be used as the verification parameters.

The computed leaflets morphologies were in a good agreement with previous studies which are presented in Figure 4.4 at six discrete opening and closing times of the cardiac cycle. The valve opens to 74% of the cross-sectional area of the aortic ring while the computed commissural expansion was 8.1% while it is reported to be about 12% from the echocardiography measurements which is the result of imposing pressure gradient at the outlets.

Time	Isometric view	Short axis view
t=0.00 s	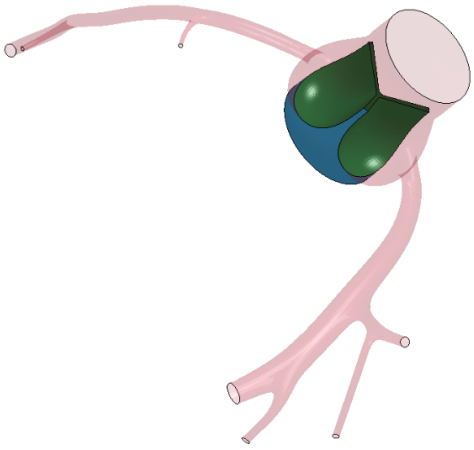	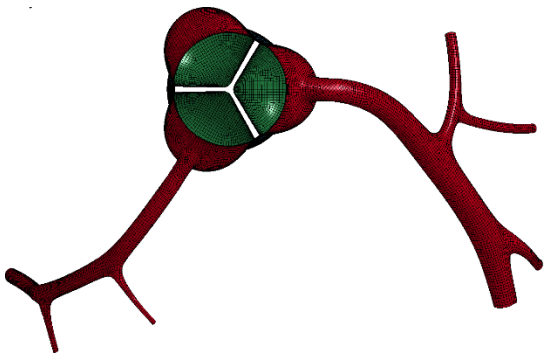
t=0.04 s	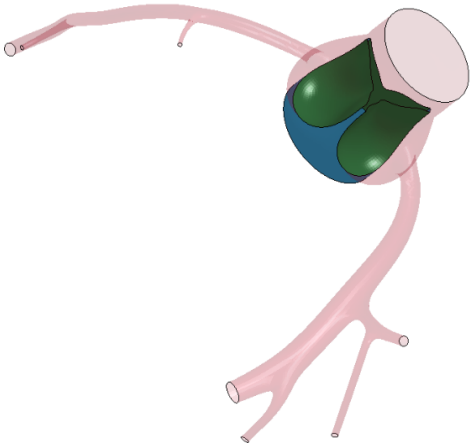	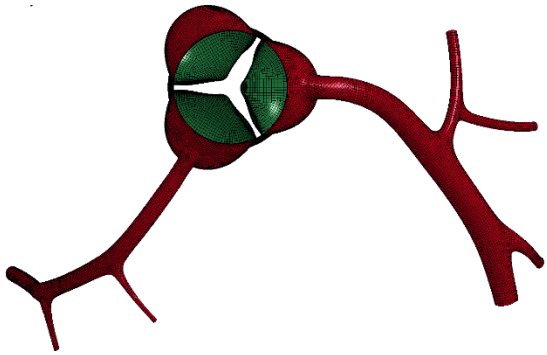
t=0.06 s	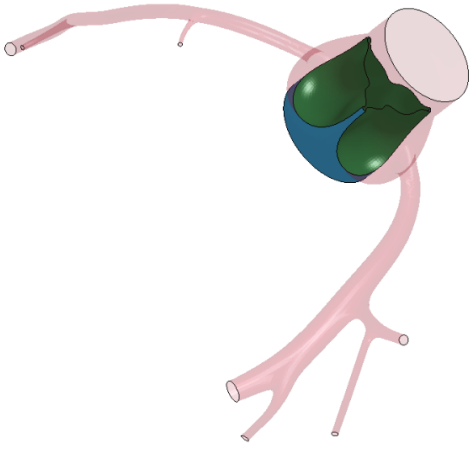	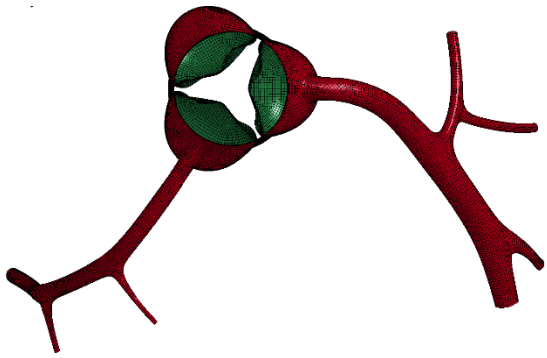

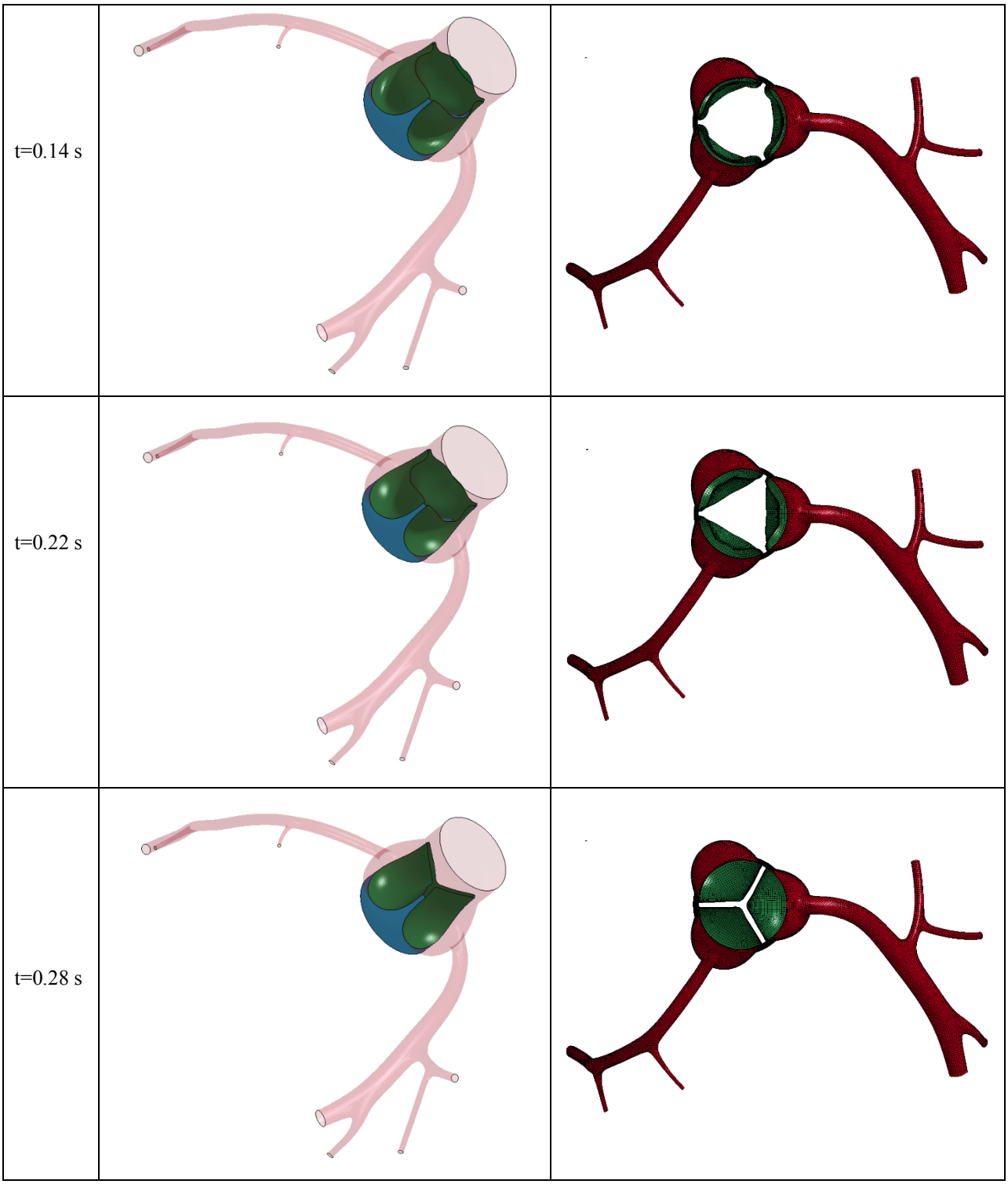

Figure 4.4: The computed leaflets morphologies, seen in isometric and short axis views

Compared to the normal aortic valve model, in the global model the ejection time was longer and maximum valve opening happened at 0.14 s. For more quantitative assessment, the clinical aspects of the leaflets tip velocity histories (section 2.4.1.a) were measured which are presented in Table 4.2. The calculated values were within the reported range from the echocardiography studies. Compared to the normal aortic valve, the valve opens and closes slower which can be the results of imposing boundary conditions of the coronary structures.

Table 4.2: Comparison between the global model and echocardiography leaflets tip velocity histories

	RVOT (ms)	RVOV (cm/s)	RVCT (ms)	RVCV (cm/s)	ET (ms)
Global model	64.3	31.0	50.0	19.8	283
Echocardiography values	57.5 ± 11.3	29.2 ± 8.7	47.0 ± 11.1	23.6 ± 7	324 ± 70

4.5.2 The fluid domain

The computed velocity profile and their induced WSS as well as the blood flow at different selected cross sections and branches outlets are presented.

The blood velocity is very important verifying biomechanical parameter as it is possible to obtain precise non-invasive measures of its characteristics by MRI. Figure 4.5 represents the computed blood flow visualized with Isosurfaces during the maximal coronary perfusion where the valve is completely closed.

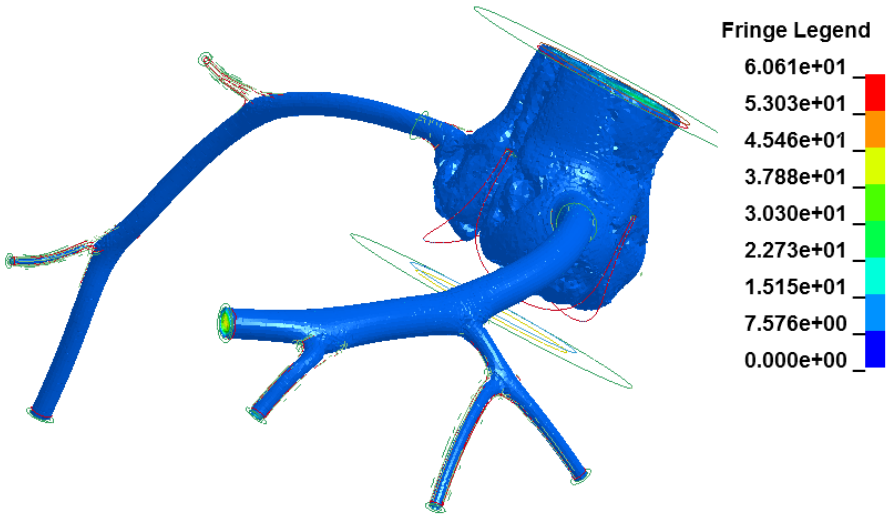

Figure 4.5: Plot of blood flow velocity vectors showing the blood flow across the aortic root region and the coronary arteries during the diastolic phase of the cardiac cycle (The unit of velocity is cm/s).

Observation of no backflow confirms the full contact between the leaflets during the diastolic phase of the cardiac cycle. Diastolic recirculation regions (vortices) in the sinuses aiding in closure of the normal valve is another wanted qualitative feature [90]. For the current model, this feature can be clearly seen in the velocity vector plots at time t = 0.241 sec in Figure 4.6.

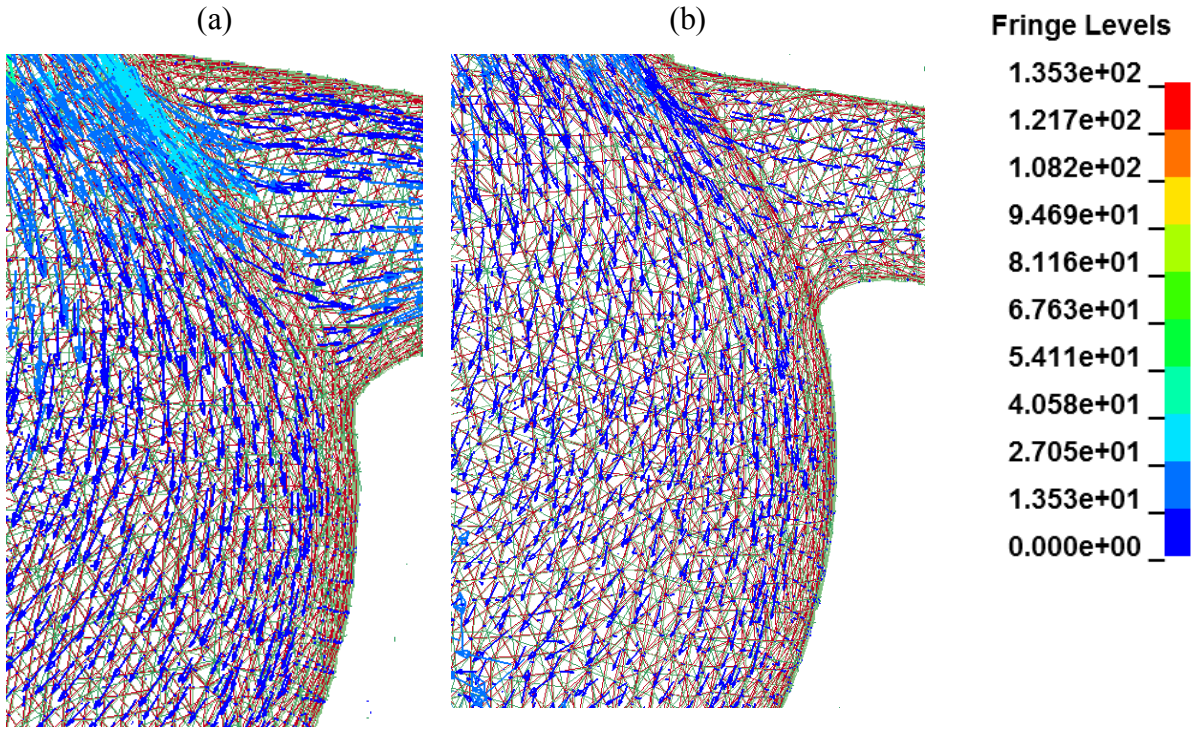

Figure 4.6: Velocity vectors representing the vortex formation behind the leaflets in the (a) left aortic sinus and (b) right aortic sinus (The unit of velocity is cm/s).

As a quantitative verification, the blood velocity across the central axis of the aorta and the coronary arteries blood flow are presented in Figure 4.7. The blood velocity in aorta reaches its peak value of 164.3 cm/s, a value in good agreement with the physiological peak velocity 135 ± 35 cm/s, during the systolic phase of the cycle and return to a magnitude near zero during the diastolic phase [129]. In addition, the measured velocity of the blood during the maximum flow at the inlet level of the left coronary artery is 29.7 cm/s while in the right coronary artery it reaches 15.7 cm/s during the maximal flow.

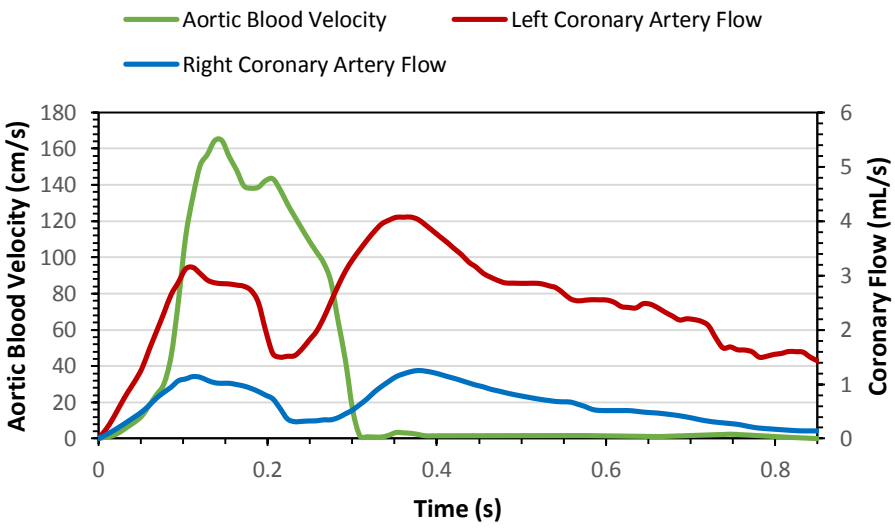

Figure 4.7: The computed time dependent aortic blood velocity (green) and coronary flow (blue: right coronary artery and red: right coronary artery)

In order to investigate the flow behavior in the coronary vessels a total of fifteen cross-sections are selected along the coronaries: nine cross-sections along LCA and six cross-sections along RCA as shown in Figure 4.8.a. Cross sections (CSs) 1 and 10 are located in the entrance of the coronary arteries while the rest of CSs are chosen along the coronary arteries before or after the bifurcation to investigate the bifurcation, branching and tortuosity impact on the flow behavior. The calculated velocity profiles when the coronary flow is maximum are presented in Figure 4.8.

(a)

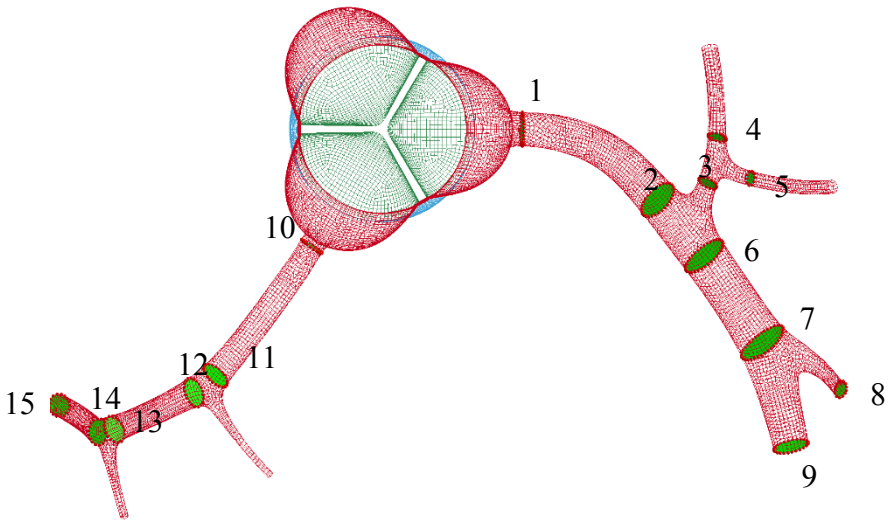

(b)

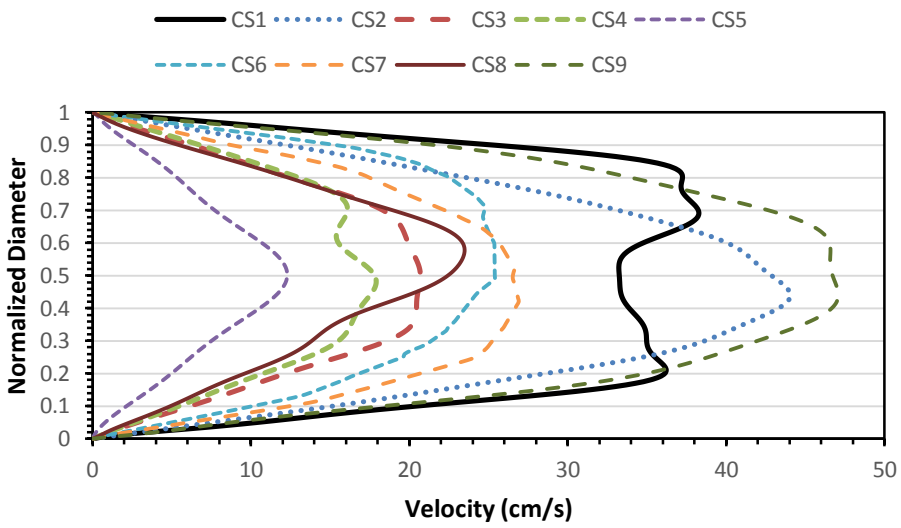

(c)

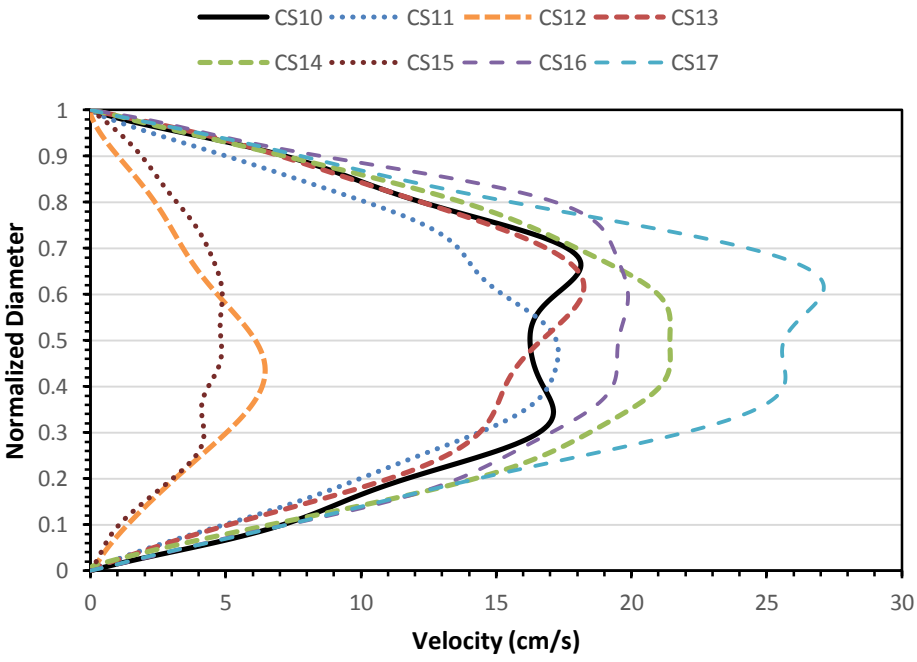

Figure 4.8: Cross-sections at which velocity profiles are calculated along the coronary vessels and the corresponding numbering system used for identification (a) Velocity profile at selected cross sections on the LCA (b) and RCA (c)

4.6 Discussion

Because of the inherent complexity of fluid-structure interaction modeling of aortic leaflets, there was a clear lack of a global representation of the aortic valve region which would assist in elucidating the overall behavior of this structure in pathological conditions. To overcome this limitation, in this chapter, as a development to the normal aortic valve model, Chapter 2:, a 3D global fluid-structure interaction model of the aortic valve including the anatomically realistic coronary vessels and their small branches was presented. For verification, on the solid domain, the calculated results in terms of the leaflet morphologies, leaflets opening and closing timing, as presented in Table 4.2, were compared to known echocardiography data showing a reasonably good match [87, 130-132]. On the fluid domain, blood velocity vector fields were obtained to assess the flow pattern across the aortic root and the coronary arteries. Vortex formation around the leaflets tip in the sinuses through the early diastole as another verifying phenomenon was observed in the simulated model, Figure 4.6. Another interesting result was the temporal velocity across the ascending aorta and the coronary arteries, Figure 4.7. The peak value of the blood velocity measured in the ascending aorta, LCA inlet and RCA inlet were 164.3 cm/s, 29.7cm/s and 15.7cm/s, respectively which were in the range reported by echocardiography studies [133, 134]. For a heart rate of 70 bpm, 5.068 L/min of blood was pumped as the total cardiac output out of which about three and one percent was delivered to the LCA and RCA, respectively. Of the blood entering the LCA, 8.13 percent flows to the LAC vessel which feeds the left atrium and in in 40–50 percent of hearts, the SA node of the heart. Also, 2.88 percent leaves through the 1st PLCx branch to supply the lateral aspect of the left ventricular myocardium and the AV node. Furthermore, 9.65 percent enters the DLAD to flow through the anterolateral wall of the left ventricle while 79.34 percent reaches to LAD vessel going in the anterior interventricular groove to the apex of the heart. Conversely, 4.71 percent of the blood flows through the RCA leaves through the CB branch to supply the right ventricle outflow tract while only 3.4 percent reaches to RV branch and the rest flows though the PD vessel which runs along the posterior interventricular groove, giving off perpendicular branches supplying the left ventricle, right ventricle and the AV node.

Furthermore, in order to study the blood flow distribution in the coronary vessels, velocity profiles were obtained along the LCA and RCA on fifteen selected cross sections, Figure 4.8.

These profiles corresponded to the maximum blood flow along the coronary structures. The flow in the inlet of the LCA and RCA (CS1 and CS10), was disturbed. In addition, the curvature and bifurcation had significant impact on the location of maximum velocity as well as its magnitude.

4.7 Conclusion

The developed model of the aortic valve region in this study was different from all the recent works in the sense that the inclusion of the coronary arteries and their branches introduced the notion of globality into the model. This global model was verified with the results of the previous numerical and echocardiography studies. This proposed model has the potential to investigate the possible causal effect of the aortic valve abnormalities on the coronary vessels pathologies, occlusion of the critical small coronary vessels and its effect on the heart muscle which will be presented in the following chapters. Such investigations are impossible with previously developed models of the aortic root without the coronary arteries or simplified structure as the coronary vessels.

Chapter 5: Hemodynamic changes in coronary arteries due to aortic root pathologies

5.1 Overview

Atherosclerosis is still the leading cause of mortality and morbidity in the developed world. Although its initiation and progression is a complex multifactorial process, it is well known that the blood flow induced wall shear stress is an essential factor for localizing early atherosclerotic plaque. In recent clinical studies, it was established that the regional pathologies of the aortic valve such as aortic stiffening and calcific aortic stenosis (CAS) can affect the coronary hemodynamics and consequently lead to the formation of the atherosclerotic plaques. However, due to some limitation either using medical imaging modalities or numerical simulation, the impact of hemodynamic effects is not yet fully elucidated for disease initiation and progression. In this study, our previously developed 3D global fluid-structure interaction of the aortic root incorporating the anatomically inspired natural cusps and the coronary artery and their critical small branches using finite element method is used to investigate the possible interaction between coronary artery pathologies and aortic valve pathologies. For the simulated healthy model, the calculated wall shear stress (WSS) ranged from 0.41 Pa to 1.34 Pa which was in the protected region. However in the moderate and severe aortic stenoses, wide regions of the coronary structures, especially the proximal sections, around the first bifurcation, were exposed to the lower values of the WSS which could potentially lead to an atherogenic phenotype.

5.2 Introduction

Atherosclerosis which leads to partial or complete occlusion of the arteries remains as the major cause of death in the developed countries. Although it is associated with multiple risk factors such as hypertension, diabetes, infection and smoking, the blood flow-induced wall shear stress (WSS) is shown to be an essential feature of atherogenesis [135, 136]. WSS which acts directly on the endothelium could modulate endothelial gene expression by shear stress response transcription factors. It was shown that the vessel regions with WSS higher than 1.5 Pa, are associated with atheroprotective gene expression profile and remain disease free, while the regions with low shear stress, less than 0.4 Pa, are atherosclerosis-prone areas due to stimulation of the atheorgenic phenotype [137]. The anatomical features such as tapering, branching, tortuosity,

sharp turns, as well as arterial wall motion due to the vessel wall elasticity are identified as the most important influencing features in the pattern of the WSS and consequently the localization of atherosclerosis lesion [115].

The coronary arteries are the most important sites of the atherosclerotic plaque formation as the occlusion can give rise to angina pectoris and myocardial infarction. Despite the clinical importance of the coronary arteries, due to the complex tortuosity and small size of the coronary vessels, there have been relatively limited studies on hemodynamic features leading to atherosclerosis in these arteries compared to the peripheral arteries [138]. Pathologies of the aortic valve such as aortic stiffening and calcific aortic stenosis (CAS) are thought to affect coronary blood flow. In recent clinical studies, it was established that such regional pathologies can alter the structural and hemodynamic function of the valve and coronary arteries and lead to development of the atherosclerotic lesion [139-142]. However, due to some limitation either using medical imaging modalities or numerical simulation, the impact of hemodynamic effects is not yet fully elucidated for disease initiation and progression.

Numerous clinical and numerical studies were done on the aortic valve region and the coronary arteries individually [45, 61, 64, 84, 143-145]. But, only a limited number of them have incorporated both of these adjacent structures into one numerical model [65, 122, 146]. Due to the large deformations that leaflets experience during the cardiac cycle, numerical modeling of fluid–structure interaction of the aortic valve has proven to be a challenging task. Adding the coronary arteries to the aortic valve model increases this complexity which constitutes the limitation of the current methods and all of the developed models so far have either ignored the natural aortic root structure by using simplified geometry of the valve or the coronary vessels or neglected the interaction between the fluid and solid domains [89, 146]. In this chapter, our previously developed 3D global fluid-structure interaction of the aortic root with inclusion of anatomically inspired coronary vessels and their critical small branches using finite element method in Chapter 4: is used to investigate the possible interaction between coronary artery pathologies and aortic valve pathologies.

5.3 Materials and Methods

The simulated global model described in Chapter 4: was used for this investigation. In order to examine the impact of the aortic valve stenosis on the pattern of the WSS on the coronary

vessels, the aortic valve stenoses models were created by constraining the motion of leaflets tip with different degrees of severity. The percentage of the reduction in the area occupied by blood from the left ventricle out tract to the orifice was used as an index to evaluate the stenosis severity.

5.4 Results

Four models including a healthy natural valve and stenotic valves with severity of 56%, 72% and 80% were simulated for analysis. The schematics of the healthy and an 80% severe stenosed valves in their maximum opening during the systolic phase seen from the position of the ascending aorta back towards the left ventricle are presented in Figure 5.1.

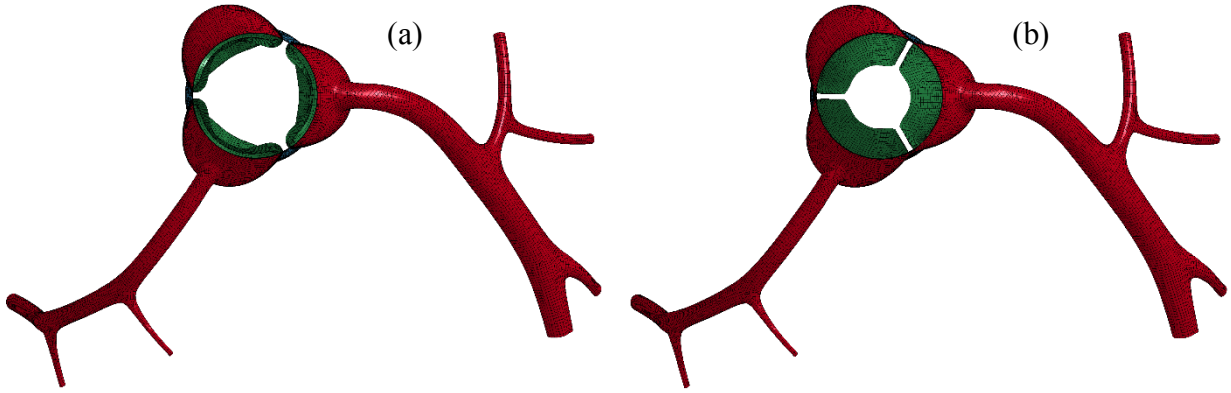

Figure 5.1: Schematic of the simulated models in their maximum opening state: Healthy model (a) and stenotic valve with severity of 80% (b)

For a healthy model, the blood velocity in aorta reached its peak value of 164.3 cm/s, a value in good agreement with the physiological peak velocity 135 ± 35 cm/s, during the systolic phase of the cycle and return to a magnitude very near zero during the diastolic phase [129]. In addition, the measured velocity of the blood during the maximum flow at the inlet level of the left coronary artery is 29.7 cm/s while in the right coronary artery it reaches 15.7 cm/s during the maximal flow. In order to investigate the flow behavior in the coronary vessels, a total of fifteen cross-sections are selected along the coronaries: nine cross-sections along LCA and six cross-sections along RCA as shown in Figure 5.2.a. Cross sections (CSs) 1 and 10 are located in the inlet level of the coronary arteries while the rest of CSs are chosen along the coronary arteries before or after the bifurcation to investigate the bifurcation, branching and tortuosity impact on the flow behavior. The calculated velocity profiles when the coronary flow is maximum are presented in Figure 5.2.b

(a)

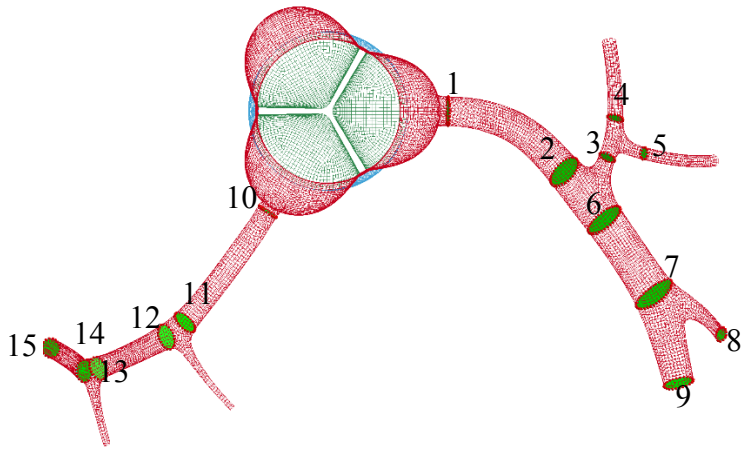
1
2
3
4
5
6
7
8
9
10
11
12
13
14
15

(b)

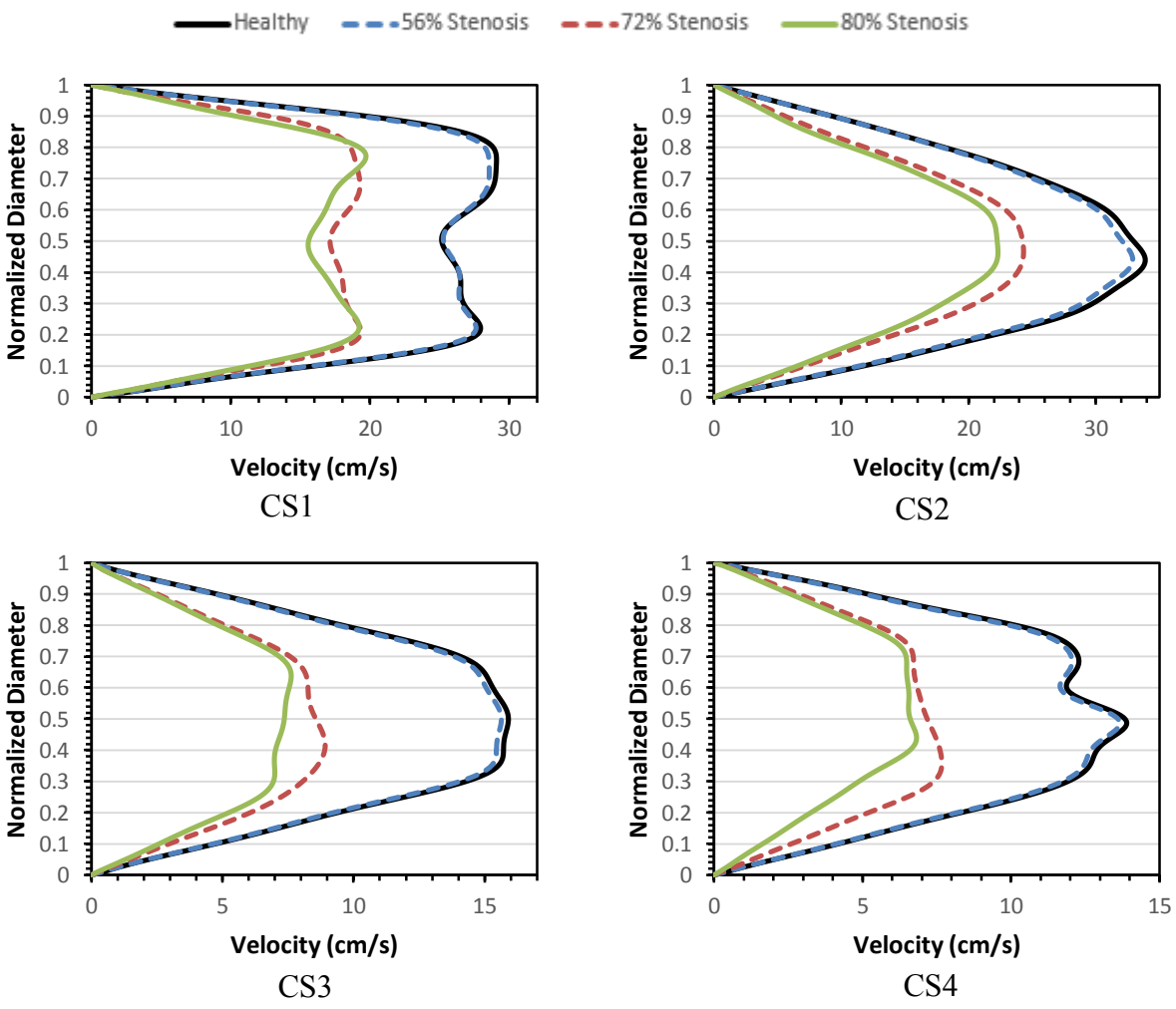
Healthy
56% Stenosis
72% Stenosis
80% Stenosis
Normalized Diameter
Velocity (cm/s)
CS1
CS2
CS3
CS4

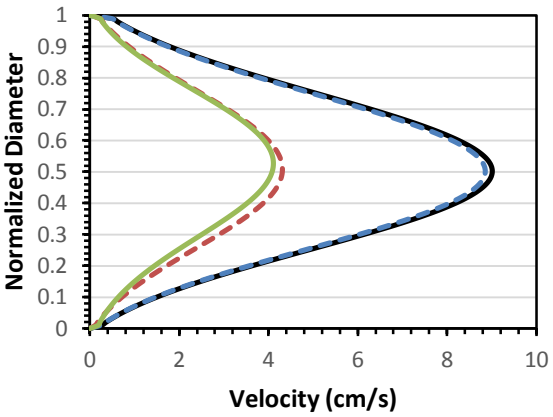

CS5

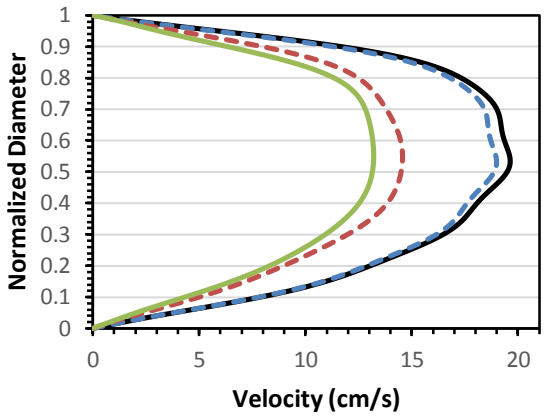

CS6

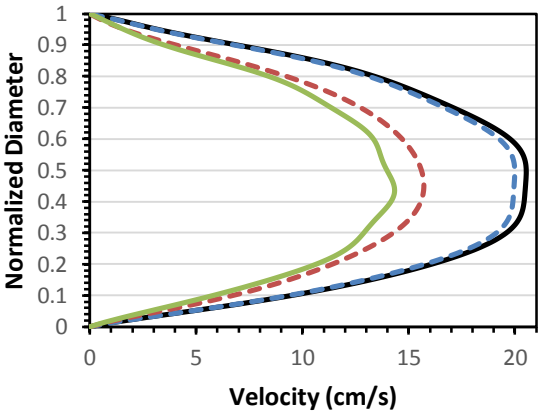

CS7

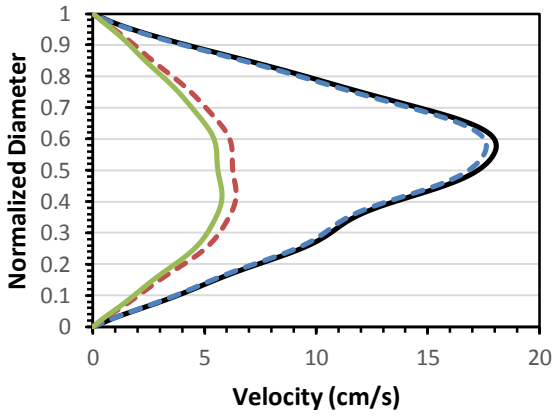

CS8

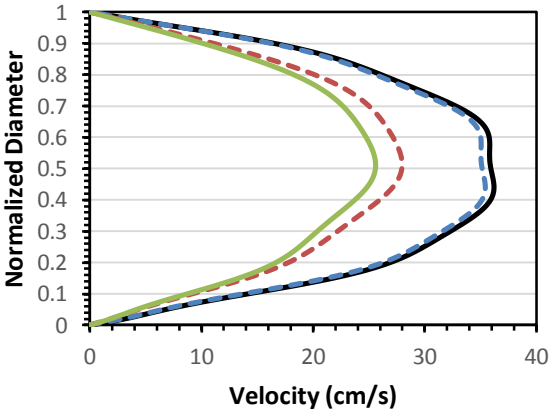

CS9

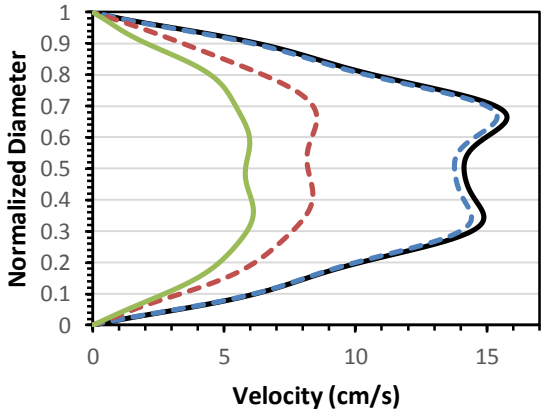

CS10

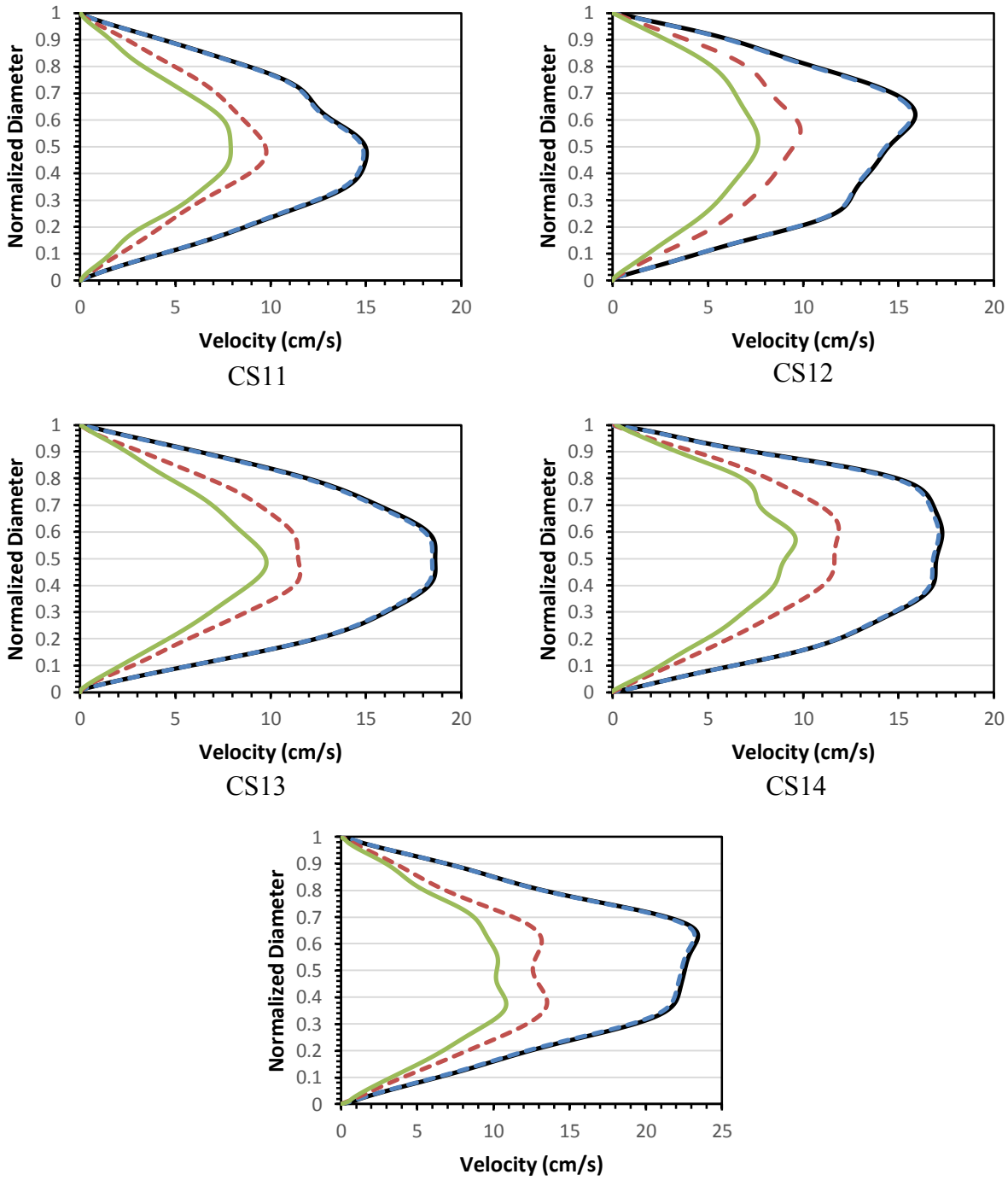

Figure 5.2: Cross-sections at which velocity profiles are calculated along the coronary vessels and the corresponding numbering system used for identification (a) Velocity profile at selected cross sections (b)

The velocity profile at the inlet level of both coronary arteries for the healthy and stenotic valves were blunt with progression of the blood flow along the arteries, the velocity profile became

fully developed before giving rise to the small branches. However, as a result of the branching, sharp turns and bends the magnitude and location of the peak velocity changes by general displacing to the outer wall which agreed with findings from previous studies [144, 145]. In order to examine the impact of the aortic valve constriction on WSS qualitative and quantitative changes on the left and right coronary vessels, the corresponding induced WSS of the calculated velocity profiles during the peak flow are presented in Figure 5.3.

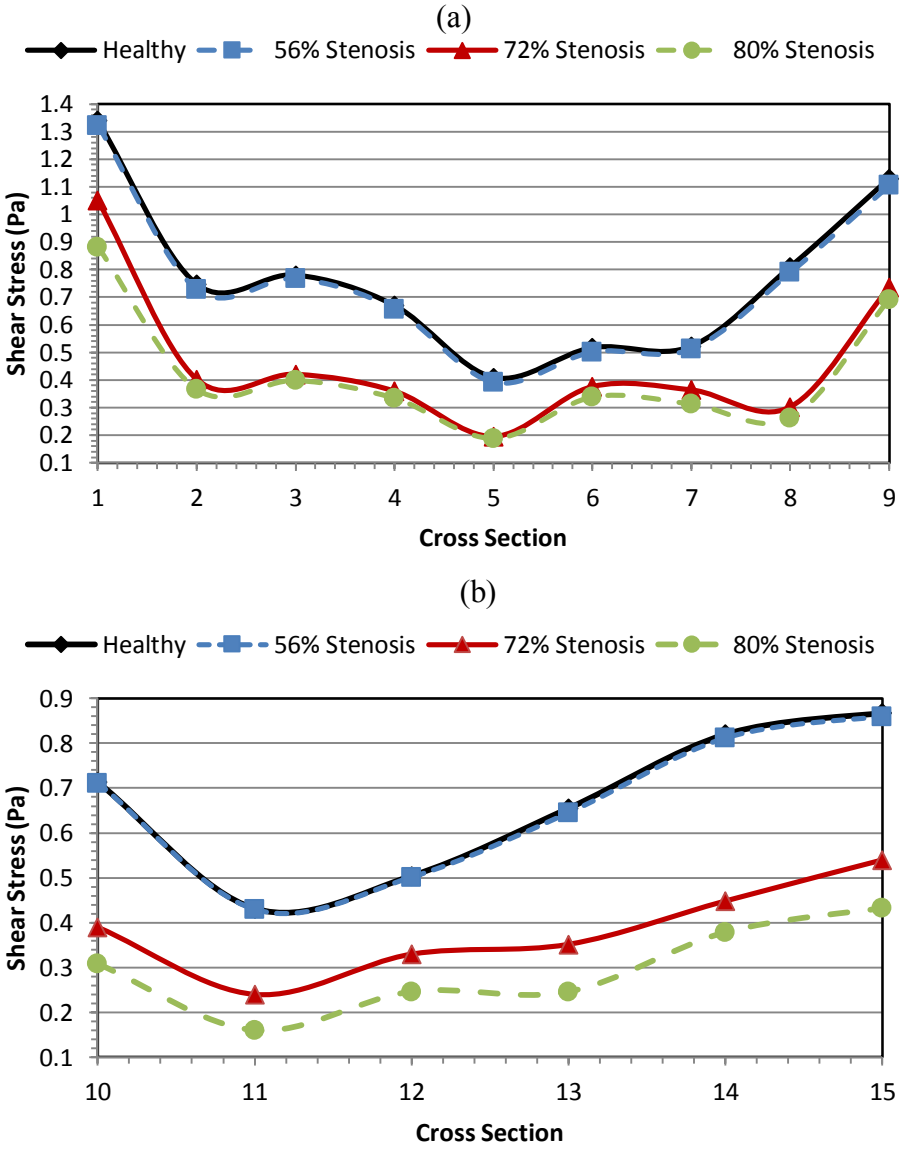

Figure 5.3: The calculated imposed shear stress on LCA (a) and RCA (b) for the simulated models of the aortic valve constriction

The measured values indicate a good agreement with reported values of WSS for the healthy arteries and confirms the results of the previous clinical and numerical studies reporting the distal proximal of the coronary arteries as the most problematic regions for initiation and progression of atherosclerosis for all simulated models [137, 138].

5.5 Discussion

Because of the difficulties associated with studying blood flow across the small sized and complex coronary arteries, little is understood about the link between the hemodynamic changes in these vessels and onset of the atherosclerosis. In addition, evidence from recent studies suggests that there is a causal effect of the aortic valve abnormalities on pathologies of the coronary vessels [141, 142]. However, due to inherent complexity of fluid-structure interaction modeling of aortic leaflets, there is a clear lack of a global representation of the aortic valve region with inclusion of the coronary structures to assist elucidating the overall behavior of this structure in pathological conditions. Hence, this study was undertaken to investigate the impact of the aortic valve stenosis on the hemodynamic of the coronary arteries. The previously developed 3D global fluid-structure interaction model of the aortic valve including the anatomically realistic coronary vessels and their small branches was used for this purpose. The stenosed aortic valve models were simulated by constraining the motion of leaflets tip. The calculated velocity profiles along the coronary arteries on the selected cross sections (Figure 5.2.a) were presented for the healthy and the stenotic valves in Figure 5.2.b. Interestingly, for the moderate aortic stenosis (stenosis with severity of 56%) the change in the velocity profile was negligible compared to the healthy model while as the stenosis became severe (72% stenosis) and critical (80% stenosis) the peak value of the velocity in all cross sections were reduced. As expected, due to the vortex formation behind the aortic sinuses, the velocity profiles at the level of ostium (CS1 and CS10) for both coronary vessels were blunt while it becomes fully developed before the first bifurcation (CS2 and CS11). All models exhibited similar flow patterns and due to the multiple bends, the general displacement of the higher momentum fluid to the outer wall was detected similar to the results of the previous studies [147-149]. As discussed, the distribution of WSS in coronary arteries is thought to be a significant feature which is linked to the onset and development of the coronary heart disease. Hence, to investigate the link between the impairment of the aortic valve and diseases of the coronary arteries, the calculated WSS along the proximal, distal and marginal portions of the coronary

arteries corresponding to the selected cross sections were presented in Figure 5.3. For the healthy model, WSS ranged between 0.41 Pa and 1.34 Pa on LCA and 0.43 Pa and 0.83 Pa on RCA. Hence, according to the findings of previous clinical study, since the arterial regions with WSS less than 0.4 Pa, are atherosclerosis-prone areas due to stimulation of the atheorgenic phenotype, the healthy model was in the atheroprotected range. In contrast to the moderate stenosis which led to indistinguishable change in the WSS magnitude relative to the healthy valve, for the severe and critical stenosis, most portions of both coronary vessels were exposed to WSS less than 0.4 Pa indicating disease prone regions due to the aortic valve impairment. The impact of the aortic stenosis severity on WSS magnitude change on the right coronary artery was more significant as the values of the blood velocity and consequently the induced WSS were less than those of the left coronary. In all simulated models, the arterial areas around the first bifurcation on the main circumflex (MCx) of the left coronary and those around the first bifurcation on the right coronary were the most problematic areas since they were exposed to low values of WSS. While due to the rapid changes in the arterial curvature, WSS exhibited higher values on the distal portions of the coronaries.

5.6 Conclusion

As previously discussed, by using this model, it is possible to investigate the causal effect of the aortic valve on the coronary vessels pathologies which was the main emphasis of this chapter. The results revealed significant impact on coronary hemodynamics due to constriction of the aortic valve. And a continuous drop in WSS and blood velocity was detected with progression of the aortic stenosis. It can be concluded that in patients with severe and critical aortic stenosis, coronary arteries are prone for localizing early atherosclerotic plaque and its risk is higher on the right coronary vessels. These findings not only are coherent with recent clinical studies, also, particularly attempt to reveal some of the possible underlying reasons behind the detected link between aortic valve impairment and coronary artery diseases.

Chapter 6: Regional hemodynamic of Multi-Vessel Coronary Plaques

6.1 Overview

Coronary plaques occur frequently at bifurcations sites and they are reported as one of primary causes of death in the developed world. Percutaneous coronary intervention, for treatment of multi-vessel coronary lesions, is associated with high event rates. In the context of complex interaction between multiple stenoses a simple FFR measurement is insufficient for assessing the functional severity of the regional multi-vessel coronary disease. In order to improve the understanding of the formation and development of coronary plaques and elucidating the mechanism of interaction between multiple coronary lesions globally located on different coronary vessels, in this chapter a the developed global model is used to investigate the hemodynamic changes corresponding to different types of coronary multi-vessel plaques with different severities. Results revealed significant hemodynamic changes in the setting of either a single left main stem lesion or concomitant left main stem plaques with downstream lesions.

Coronary artery disease (CAD) is still the leading cause of death in the developed world. Atherosclerotic plaques are the main causes of CAD which result in the lumen stenosis [150]. Plaques have a tendency to occur in the vicinity of coronary bifurcations and about 15% to 20% of the total number of percutaneous coronary interventions are performed for multi-vessel coronary lesions. However, compared to non-bifurcation coronary lesions, percutaneous coronary intervention of multi-vessel coronary lesions is a challenging task associated with lower success rate, higher procedural costs, and higher angiographic restenosis [151, 152]. Consequently, better insight into hemodynamic of multi-vessel lesions is needed to improve the current strategies and devices [153].

In order to determine the functional significance of the coronary stenosis, fractional flow reserve (FFR) has become the gold standard technique over the past few years. It is defined as the ratio of maximal myocardial blood flow in the case of a diseased artery to maximal myocardial blood flow if the same artery was normal. Therefore, it represents the extent to which maximal myocardial blood flow is limited by the presence of CAD. The use of FFR to guide revascularization of coronary diseases has given rise to improved patient outcomes [154].

However, due to the dynamic interaction of the multiple stenoses, the hemodynamic significance of individual stenosis is affected. Hence, a simple FFR measurement appears inadequate for assessing the functional severity of individual stenosis for multi-vessel coronary plaques [155]. Recently, it is hypothesized that using the gradient of FFR across an individual stenosis is a surrogate of the relative hemodynamic significance of each lesion is coronary tandem lesion [156]. Nevertheless, the mechanism of interaction between multiple coronary lesions located on different coronary vessels still remains unclear. Aggravation of a side branch (SB) ostial stenosis after implantation of main branch (MB) stent is another phenomenon associated with treatment of multi-vessel coronary plaques which needs to be elucidated using a functional analysis [157].

Most medical imaging techniques only provide anatomical parameters of the coronary vessels and do not provide functional assessment of the plaques. The hemodynamic parameters such as pressure gradient across the lesion, blood flow changes and blood induced wall shear stress are not provided by imaging. Accordingly, in order to improve the understanding of the formation and development of plaques, numerical methods has been widely used to study blood flow through the coronary arteries over the last few years [115, 158, 159]. However, the current studies have considered the impact of the lesion severity on hemodynamic changes in the coronary artery. Regional models of either left coronary artery or the right coronary artery using computational fluid dynamics (CFD) in which the interaction between blood, vessel wall and the aortic valve is neglected have been reported. The primary aim of this study is to develop a model to investigate the hemodynamic changes corresponding to different types of coronary multi-vessel plaques with different severities using a global model.

6.2 Materials and Methods

Depending on the location of the plaques, the coronary multi-vessel lesions present a wide range of angiographic and anatomical morphologies. Hence, indexing facilitates their description. Different classifications are proposed for the identification of these lesions among which the Medina classification is the simplest one to use. This classification uses the three segments of a bifurcation including the main branch proximal (MBP), the main branch distal (MBD), and the side branch (SB). By respecting the order of these segments, binary values of 1 and 0 are assigned to each segment according to whether it is affected by lesion or not. The schematic of the

considered types of lesions in this study and their identification using Medina indexing is depicted in Figure 6.1.

The generated lesions were axisymmetric whose shape (Figure 6.2) was defined by the following equation [100]:

$$\frac{R}{R_0} = 1 - \frac{\delta}{2R_0}(1 + \cos\frac{\pi z}{Z_0}) \qquad \text{for } -Z_0 \le z \le Z_0 \quad \text{with} \quad \frac{\delta}{2Z_0} \le \frac{1}{5} \tag{6.1}$$

where R_0 is the radius of the non-constricted vessel, $2Z_0$ refers to the length of the lesion, δ is the maximum height of the lesion while R and z define the shape of the lesion in the illustrated coordinate system in Figure 6.2.

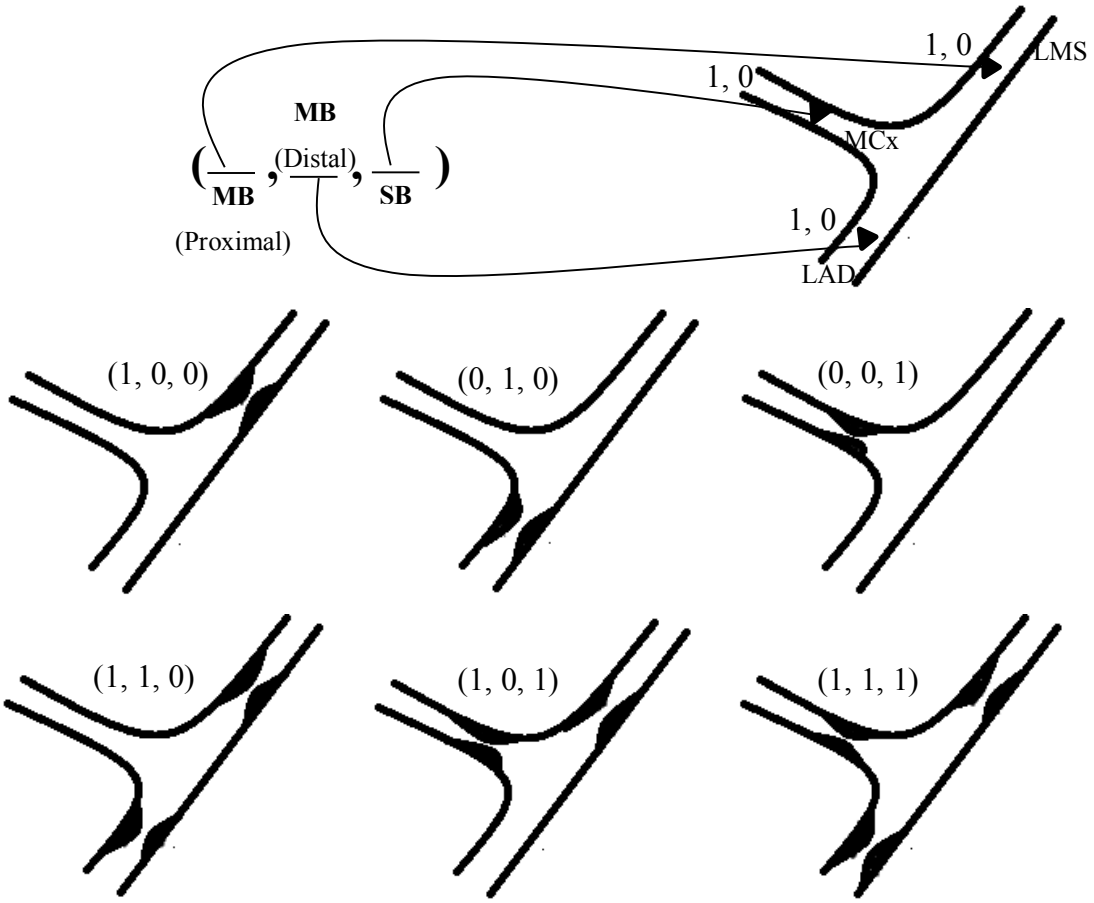

Figure 6.1: The investigated lesions in this study and their identification using Medina classification, LMS: left main stem, MCx: main circumflex, LAD: left anterior descending

Since the bifurcation of LCA into the MCx and LAD is reported as the most prevalent location affected by multi vessel lesions, [160], LMS, MLAD and MCx were selected as the three segments

of the medina indexing on which the six plaque configurations presented in Figure 6.1 were generated.

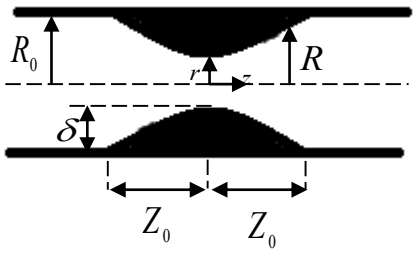

Figure 6.2: Geometric configurations of the generated lesions.

A total of 18 combinations of the stenoses with 50, 80 and 88 percent reduction in lumen cross sectional area corresponding to 30, 55 and 65 percent diameter stenosis for the six configuration presented in Figure 6.1 were generated. The severity of the constrictions on all segment of each configuration was the same. Figure 6.3 presents the schematics of the generated 88% area stenoses on the left coronary artery corresponding to (1, 1, 1) configuration. In order to investigate the impact of the constrictions to flow behavior in the coronary vessels and measure the corresponding hemodynamic changes, a total of fifteen cross-sections (CSs) were selected along the left coronary artery which are shown for 88% area (1, 1, 1) type stenosis in Figure 6.3.b. CSs 3, 7 and 12 are located in the middle of each constriction. Hence, their cross sectional area is variable depending on the severity of the stenosis.

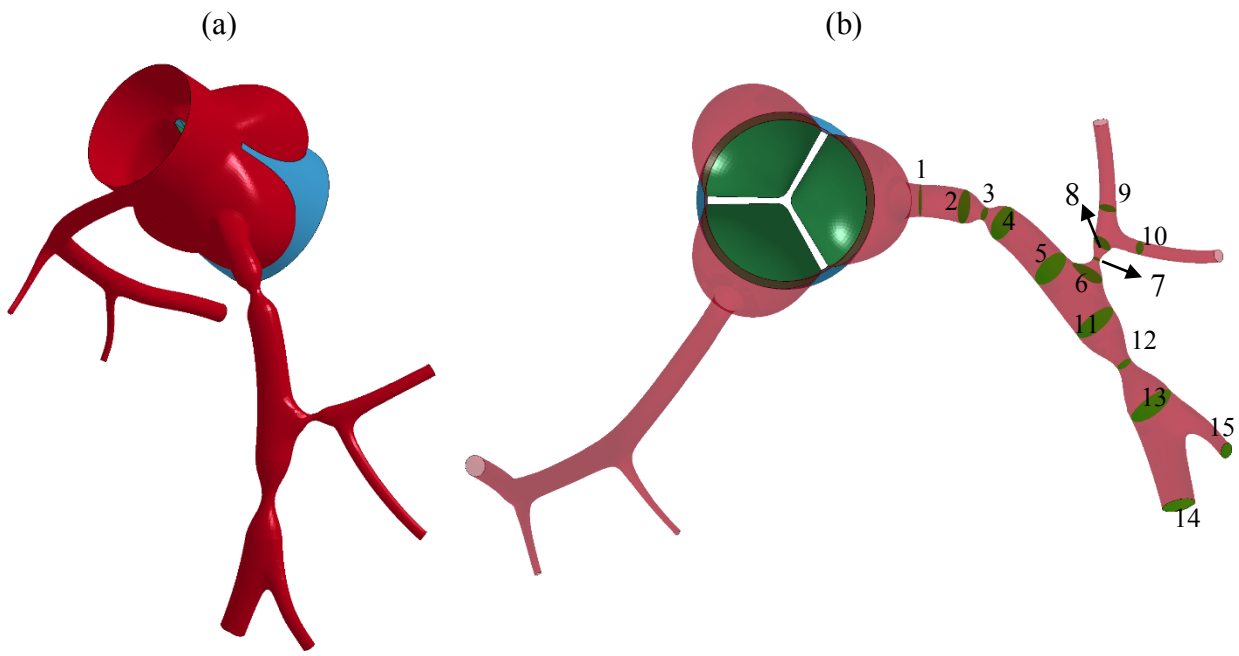

Figure 6.3: Schematics of the generated 88% area plaques on the left coronary arteries corresponding to (1,1,1) type seen in isometric view (a) as well as from a position of the ascending aorta back towards the left ventricle in transparent form including the cross-sections at which hemodynamic data are measured and the corresponding numbering system used for identification (b). To be noted the apparent gap between the leaflets corresponds to the shell thickness.

6.3 Results

A schematic of the blood flow in the fluid domain for (1, 1, 1) type of 85 percent area stenosis during diastole at peak coronary flow is depicted in Figure 6.4. Furthermore, the pattern of the flow velocity for constricted locations corresponding to this model and the healthy model are also included in Figure 6.4.

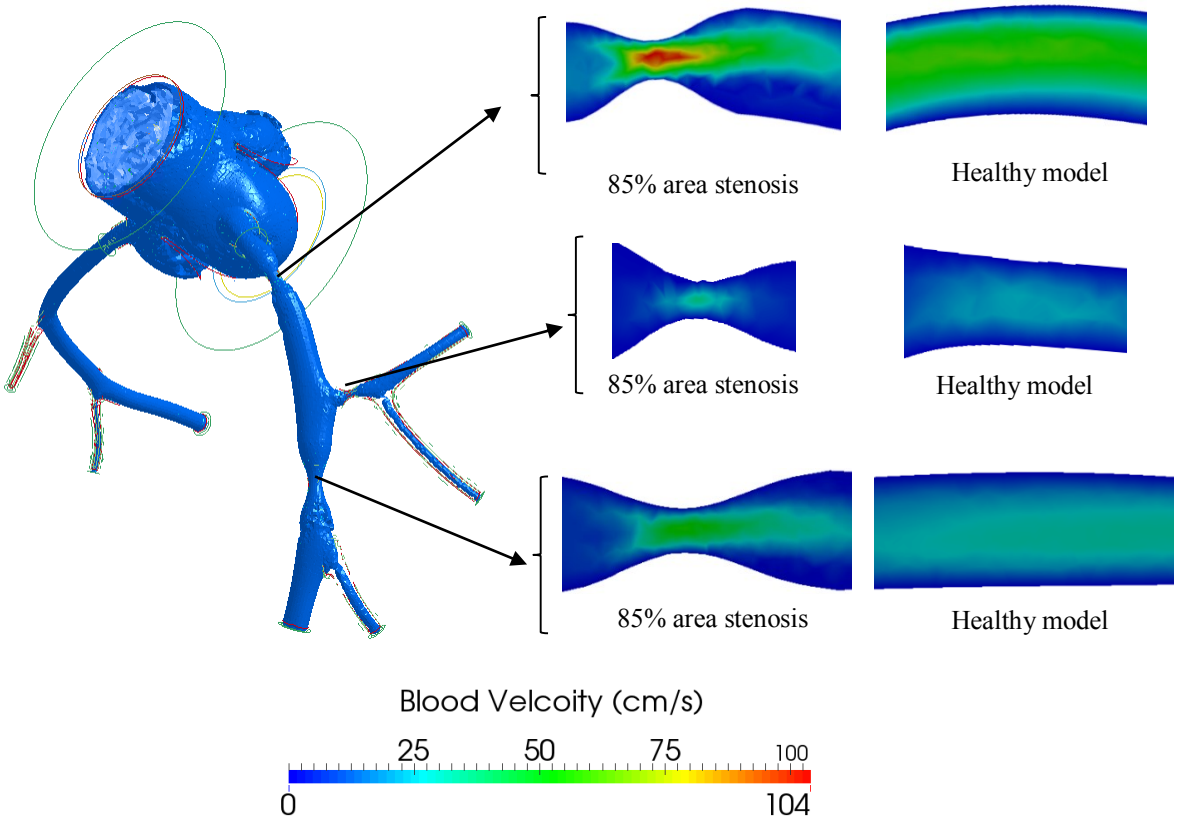

Figure 6.4: Visualized blood flow through the (1, 1, 1) stenosis with 85 percent reduction in lumen area during the coronary peak flow and the pattern of the flow velocity at construction locations compared to that of the healthy model

In the healthy model, the measured velocity of the blood at the inlet level of the left coronary artery is 23.5 cm/s and 29.7 cm/s for the systolic and diastolic phase of the cardiac cycle respectively, while in the right coronary artery it reaches 14.7 cm/s as the highest systolic value and maximum diastolic magnitude of 15.7 cm/s. The temporal waveforms of blood flow in the left coronary arteries, right coronary arteries as well as the main circumflex and main left anterior descending for a healthy model are presented in Figure 6.5. The measured values and their temporal trend during a cardiac cycle were in agreement with the average clinical observations [134].

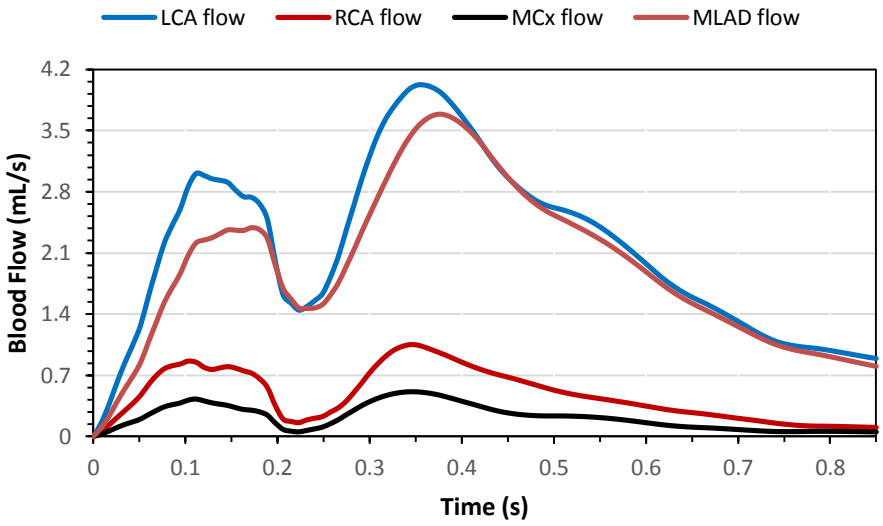

Figure 6.5: Coronary blood flow measurements in the healthy model

As discussed, a simple FFR measurement for predicting the functional severity of the individual stenosis in multi-vessel coronary plaques is insufficient. In this study, to take into account the dynamic interaction of the multiple stenosis, three FFR values including the FFR_{total}, FFR_{MCx} and FFR_{LAD} were defined as the ratio of the blood flow in a stenotic model to the blood flow in the healthy model measured in LMS, MCx and MLAD arteries, respectively. Figure 6.6 represents the calculated values of FFR_{total}, FFR_{MCx} and FFR_{MLAD}.

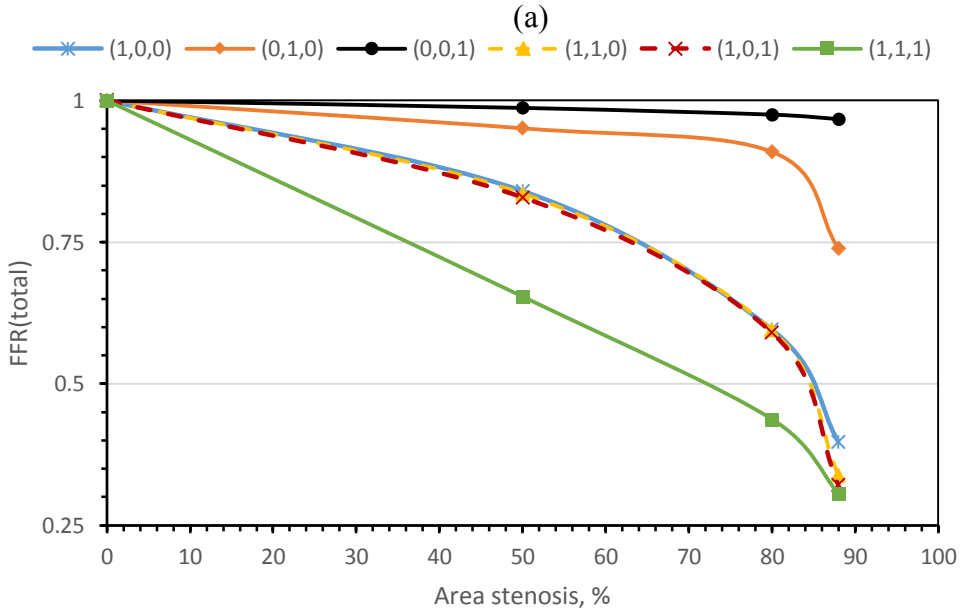

(b)

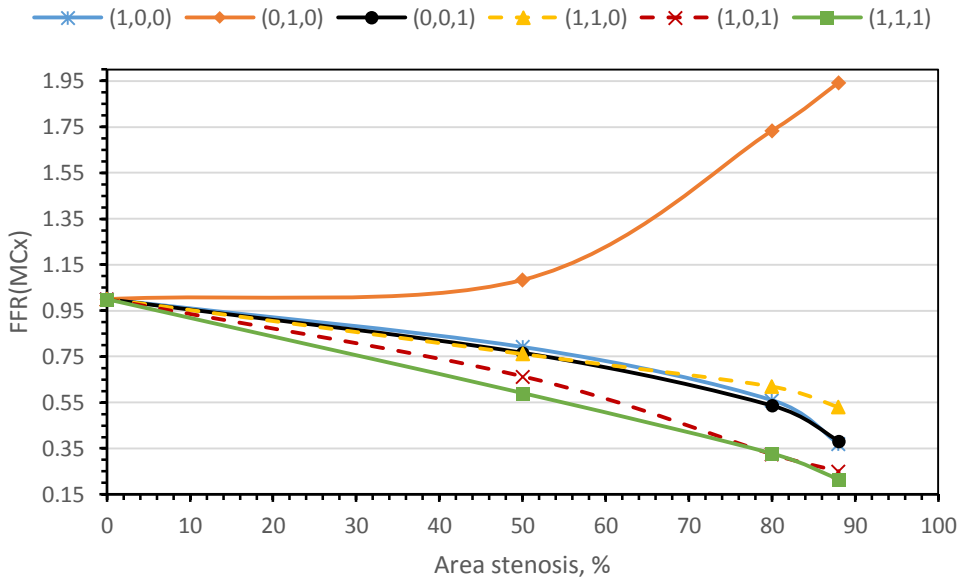

(c)

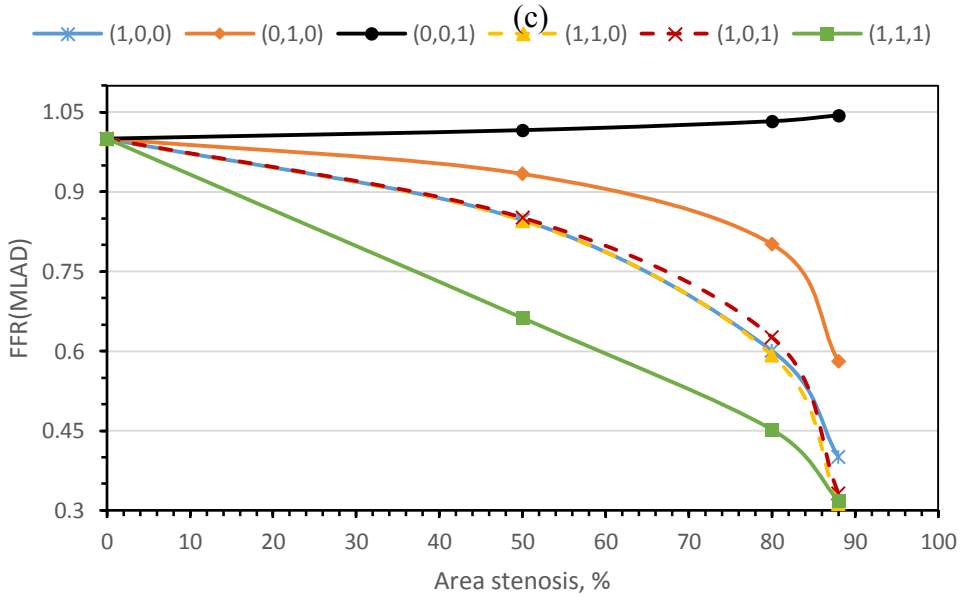

Figure 6.6: The calculated values of FFR_{total}, FFR_{MCx} and FFR_{MLAD} in the simulated models

To characterize the hemodynamic changes on the LCA due to different types of plaques, the cross sectional velocity patterns at plaques locations and the blood flow-induced wall shear stress

Table 6.1: Cross sectional pattern of the blood velocity at effective plaque-locations corresponding to the healthy model and all six types of the generated stenotic models with 88% reduction in the lumen cross sectional area

LCA	Model type						
CS	Healthy	(1,0,0)	(0,1,0)	(0,0,1)	(1,1,0)	(1,0,1)	(1,1,1)
1	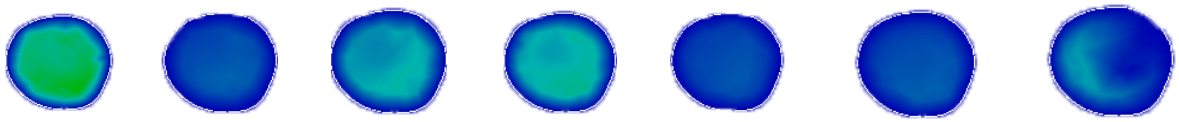						
3	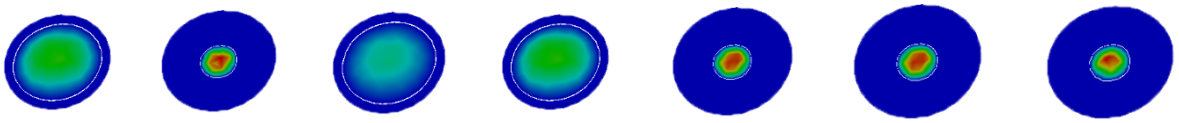						
7	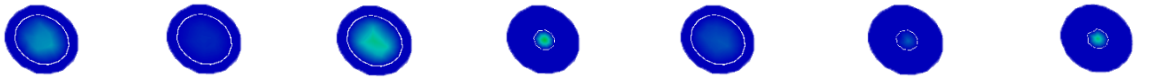						
12	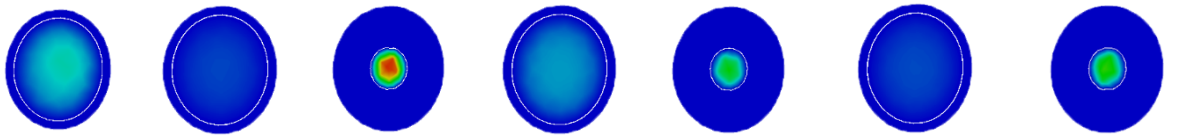						

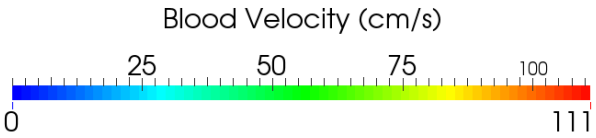

(WSS) at selected cross sections (Figure 6.3.b) were calculated and compared in the healthy model as well as all six types of the generated coronary plaques. Table 6.1 represents a comparison of the cross sectional velocity profile between the healthy model and all types of the generated 88% area stenoses while the calculated values of the blood induced wall shear stress corresponding to all simulated nineteen models are shown in Table 6.2.

Table 6.2: The calculated wall shear stress at selected cross sections

			Model Configuration					
LCA	CS	Healthy	(1,0,0)	(0,1,0)	(0,0,1)	(1,1,0)	(1,0,1)	(1,1,1)
50 Percent area stenosis								
LMS	1	1.340	1.277	1.389	1.381	1.251	1.296	1.164
	2	1.108	0.994	1.174	1.241	0.951	0.939	0.916
	3	1.131	2.624	1.008	1.064	2.784	2.754	2.454
	4	0.803	0.214	0.849	0.946	0.295	0.288	0.2
	5	0.748	0.582	0.721	0.762	0.63	0.698	0.598
MCx	6	0.272	0.218	0.368	0.179	0.186	0.198	0.196
	7	0.716	0.648	0.663	1.143	0.697	1.151	1.155
	8	0.831	0.583	0.857	0.585	0.536	0.515	0.463
	9	0.670	0.508	0.786	0.576	0.612	0.491	0.479
	10	0.410	0.31	0.434	0.301	0.365	0.216	0.281
MLAD	11	0.517	0.4	0.411	0.505	0.391	0.406	0.404
	12	0.547	0.439	1.664	0.607	1.564	0.48	1.562
	13	0.523	0.424	0.321	0.571	0.285	0.497	0.265
	14	1.130	0.962	0.932	1.165	0.985	1.2	0.909
	15	0.810	0.551	0.62	0.707	1.248	1.335	0.559
80 Percent area stenosis								
LMS	1	1.340	0.794	1.244	1.508	0.787	0.699	0.825
	2	1.108	0.516	0.850	1.215	0.396	0.453	0.546
	3	1.131	4.358	0.827	1.220	4.142	3.168	4.043
	4	0.803	0.356	0.700	0.933	0.182	0.069	0.048
	5	0.748	0.331	0.596	0.835	0.386	0.351	0.367
MCx	6	0.272	0.113	0.338	0.268	0.211	0.055	0.154
	7	0.716	0.289	0.946	1.555	0.525	1.139	2.345
	8	0.831	0.314	1.102	0.650	0.580	0.141	0.283
	9	0.670	0.262	0.835	0.629	0.489	0.145	0.263
	10	0.410	0.127	0.411	0.351	0.286	0.071	0.156
MLAD	11	0.517	0.324	0.465	0.759	0.312	0.332	0.364
	12	0.547	0.254	2.736	0.567	1.925	0.276	2.470
	13	0.523	0.244	0.176	0.595	0.042	0.294	0.200
	14	1.130	0.602	0.825	1.363	0.589	0.598	0.742
	15	0.810	0.247	1.046	0.760	0.578	0.326	0.368
88 Percent area stenosis								
LMS	1	1.340	0.432	0.819	1.445	0.481	0.549	0.499
	2	1.108	0.308	0.723	1.148	0.358	0.376	0.293
	3	1.131	5.755	0.656	1.096	5.290	7.373	5.063
	4	0.803	0.271	0.570	1.017	0.227	0.100	0.191
	5	0.748	0.226	0.461	0.765	0.264	0.341	0.283
MCx	6	0.272	0.067	0.410	0.088	0.193	0.075	0.100
	7	0.716	0.167	0.809	3.912	0.458	1.519	2.711
	8	0.831	0.165	1.147	0.251	0.480	0.097	0.154
	9	0.670	0.161	0.976	0.237	0.444	0.085	0.135
	10	0.410	0.074	0.577	0.130	0.247	0.044	0.080
MLAD	11	0.517	0.186	0.284	0.690	0.171	0.276	0.192
	12	0.547	0.157	3.717	0.600	2.375	0.262	3.081
	13	0.523	0.166	0.189	0.605	0.133	0.251	0.139
	14	1.130	0.334	0.582	1.239	0.323	0.504	0.416
	15	0.810	0.152	0.284	0.817	0.158	0.266	0.218

6.4 Discussion

Because of the intrinsic risks associated with intervention of the multi-vessel coronary lesions and complications such as higher angiographic restenosis, functional assessment of the coronary plaques is necessary to improve the current strategies and devices. As the medical imaging techniques are limited in the complete evaluation of the coronary lesions, numerical simulations have gained a considerable attention in homodynamic assessment of the coronary vessels. However, the current studies have only considered a regional model of the coronary arteries in which the interaction of the coronary blood flow and vessel wall as well as the aortic root is neglected. Furthermore, they have only investigated the impact of the plaque severity on hemodynamic changes in the coronary vessels. It is well known that in multi-vessel coronary lesions, the hemodynamic significance of individual stenosis is affected by others while few studies have considered this interaction. In this study the developed 3D global fluid-structure interaction model of the aortic root incorporating the natural cusps of the aortic valve and with anatomically inspired coronary vessels was used. For a functional analysis of the plaques, the impact of the lesions location as well as their severity was investigated. Based on the Medina classification, six plaque configurations were defined and the calcified plaques were generated using the profile defined in equation (6.1). Progressive lesions from mild to severe were constructed on the left coronary arteries while the severity of the all constrictions on each configuration was identical.

The myocardial blood flow is proportional to the size of the myocardial bed and the presence of the coronary lesions is responsible for the reduction of the myocardium perfusion. Since the LMS myocardial bed consists of the MLAD and MCx beds, it has a large size [161]. The LMS supplies about 75% of the left ventricular myocardium in patients with right dominant type and 100% in the case of left dominant type [162]. Hence, occlusion of LMS would reduce the blood supply to large portion of the myocardium resulting in high risk of life-threatening LV dysfunction and arrhythmias. LMS lesions are prevalent which happens in 4% to 7% of patients undergoing coronary angiography. Identification of significant left main disease is a challenging task and it is reported that LMS lesions treated medically for FFR ≤ 0.80 are associated with excellent clinical outcomes in terms of adverse cardiac event rates. [162, 163]. Angiographically significant LMS stenosis is defined as reduction in luminal cross section $\geq$75%. However, coronary angiography

often underestimates or overestimates the plaque functional severity assessment. It is reported that more than 20% of lesions in LMS with area severity ≤75 are ischemia producing and such a mismatch is frequently encountered in clinical assessment of LMS lesion using angiography and FFR [164]. As demonstrated in Figure 6.6, the calculated FFR_{total} of LMS lesions ((1,0,0) configuration) with area severity less than 60% was higher than 0.80 while by increasing the severity to 80 and 88 percent, the myocardium perfusion was reduced to 0.61 and 0.40 of the healthy model which was consistent with the findings of previous studies [160, 164]. On the contrary, the reduction in FFR_{total} due to a single lesion in either the distal main branch or side branch was less considerable compared to a plaque in LMS which could be explained as a result of the branch steal in the corresponding stenotic models. According to Figure 6.6.a, the calculated FFR_{total} for the severe (0, 0, 1) stenosis was 0.96 which is much higher than the cutoff value of 0.75. Similarly, for the moderate and mild (0, 1, 0) lesions, the FFR_{total} was higher than 0.9 while in a severe stenosis it was reduced to 0.74. In the simulated models with a lesion in either MLAD or MCx, as a result of the increased resistance of the affected artery, the non-stenotic branch shunts the blood flow away from the parallel daughter branch. This phenomenon which is known as the branch steal was reported in the previous studies [165, 166]. As illustrated in Figure 6.6.a and Figure 6.6.b, when a single plaque is introduced into MCX, due to the branch steal, the FFR_{LAD} was increased and consequently, the FFR_{total} reduction was negligible while FFR_{MCx} lessened significantly such that for plaques with area severity ≥0.5 it was below the cutoff value of 0.75. Similarly, a plaque in MLAD raised FFR_{MCx}. However, as the MLAD bed size is larger than that of MCx, compared to (0,0,1) models, the simulated (0,1,0) models, presented smaller flow reduction in the affected branch and more intense branch steal by non-affected daughter branch compared to (0,0,1) configurations.

The coronary lesions are diffuse and a LMS stenosis is usually associated with plaques in the other branches[162]. As presented in Figure 6.6.a, in the setting of LMS and downstream lesions, (1,1,0) and (1,0,1) configurations, as a result of the branch steal, except for the severe downstream lesions, the change of the calculated FFR in the LMS was inconsiderable. However, according to Figure 6.6.b and Figure 6.6.c, the reduction of the calculated FFR in the affected downstream artery was more significant compared to a single LMS plaque, especially for (1, 0,1) lesions. These findings indicate that only a severe lesion in MLAD and MCx will influence the FFR_{LMS} which

are consistent with the results of the previous investigations [160, 166]. As expected, when a LMS lesion is concomitant with lesions in both downstream arteries, due to the increased resistance and reduced size of the myocardial bed in both daughter branches, no branch steal happened which led to the remarkable drop in the calculated FFR. As illustrated in Figure 6.6, even for a mild lesion the FFR was less than the cut off value.

The reduction of the myocardium perfusion, influences the blood flow velocity which is the main component of WSS. Furthermore, the hemodynamic change due to the presence of lesions may give rise to the further distribution of lesions. The WSS is known to be an essential feature of the lesions acting directly on the endothelium [135, 136]. It could modulate endothelial cell gene expression through activation of the shear stress response transcription factors. It is proven that the vessel regions with WSS higher than 1.5 Pa, are associated with plaque protective gene expression profile. Hence they remain disease free, while due to the stimulation of the atheorgenic phenotype in the regions with low shear stress, less than 0.4 Pa, are plaque-prone areas [137]. In this study 0.4 Pa was considered as the cut off value of WSS. The visualized patterns of the flow velocity for all simulated 88% area plaque configurations and the healthy model during the maximum flow are demonstrated in Table 6.1. The results revealed significant changes in the velocity of the blood flow. In the healthy model, the maximum measured velocity was 43.81 cm/s occurred in MLAD while the peak value of the calculated blood velocity corresponding to multi-vessel lesions, was 111.17cm/s which happened in CS 3 of the 88% area (1,0,1) stenosis. According to Table 6.2, except for the inlet level of MCx (CS 6), in the healthy model, the calculated WSS on LCA ranged between 0.410 Pa in CS 10 and 1.340 Pa in CS1 indicating the plaque protected regions. The low value of WSS in CS 6 can be interpreted as the distribution of the lower flow (compared to CS 5) over higher vessel cross sectional area (compared to CS 7).

When the blood flow passes through the stenotic arteries, upstream of the plaque, the flow accelerates due to the constriction presented by the stenosis resulting in a jet with a higher velocity and WSS compared to the normal case at the vena contracta (CSs 3, 7 and 12). However, the expansion of the flow after passing the vena contracta, leads to recirculation and energy losses. As a result, within the short distances from the lesions (CSs 4, 5, 8 and 13), low velocity and WSS was observed (Figure 6.4). This velocity fluctuations gave rise to the flow recirculation in post-stenotic regions. Along LMS, in presence of a single lesion in one of the two downstream segments

of the bifurcation, there was no case of WSS ≤ 0.4 Pa while by presence of either a single lesion in LMS or a lesion in LMS concomitant with downstream plaques, the decreased flow and higher energy loss led to WSS≤ 0.3 Pa in CS 4.

Along MCx, when a single mild lesion is introduced to LMS, CSs 6 and 10 were the regions with WSS less than 0.4 Pa. However, by increasing the severity of the lesion, the calculated WSS on all defined sections was lower than cut off point. Furthermore, as a result of the branch steal in the setting of a single plaque in MLAD, the calculated WSS on all sections was higher than 0.4 Pa. For the rest of the configurations, the post stenotic sections were the problematic regions with WSS less than cut off value.

Along MLAD and its downstream branches, in the setting of a mild LMS plaque, all sections experienced WSS higher than 0.4 Pa while by increasing the percentage of the occlusion, their calculated WSS was dropped to values lower than cut off point. Branch steal in the presence of a MCx plaque made MLAD a safe region. In (0, 1, 0) and all multi vessel configurations, the WSS on most of the sections was below the cut off value making them prone to develop atherosclerotic lesions.

6.5 Conclusion

This chapter aimed to investigate the mechanism of interaction between multiple coronary lesions with varying severities located on different coronary vessels and improve the understanding of the formation and development of coronary plaques. It was different from all the recent works in the sense that the using the fluid-structure interaction model of the aortic root with inclusion of anatomically inspired aortic cusps and coronary structures introduced notion of globality to the study which could give better insight into hemodynamic of multi-vessel plaques to improve the current strategies and devices. The results indicated that occlusion of the LMS could lead to significant difficulties and considerable alteration of WSS in downstream regions. Furthermore, the branch steal was observed to be an important phenomenon in the setting of either a single lesion in downstream branches or a LMS plaque concomitant with a downstream lesion which could lead to further development of atherosclerotic lesions by alteration of WSS.

Chapter 7: 3D global fluid-structure interaction model of the aortic valve incorporating the thoracic aorta and coronary arteries

7.1 Overview

Cardiovascular diseases such as aortic valve impairment, coronary heart diseases, aortic aneurysm and aortic dissection are still the leading causes of death in the developed world. The decline in the mortality rate associated with the circulatory system diseases is accredited to development of new diagnostic and prognostic tools. It is well known that there is an inter relationship between the abnormalities of the aortic valve and pathologies of the thoracic aorta and coronary vessels. However, due to the limitations of the current tools, the possible link is not elucidated. In this chapter, the 3D global model will be developed by incorporating the healthy thoracic aorta anatomy including aortic arch and its main branches. This model is different from the previous studies in the sense that the inclusion of the coronary structures and thoracic aorta into the natural aortic valve introduces the notion of globality into the model enabling us to explore the possible link between the regional pathologies. The calculated hemodynamic variables from the solid and fluid domains of the simulated global model were assessed qualitatively and quantitatively.

7.2 Introduction

Cardiovascular diseases are the leading causes of death in the developed world [150]. In addition to making considerable difficulties for patients and affecting their life quality, these diseases have a significant economic cost through missed work and lower productivity [167]. Diseases of the aortic valve, coronary arteries and the thoracic aorta, are responsible for more than 80 percent of circulatory system deaths. Hence, more emphasis should be placed on developing the means to enhance our understanding of the initiation and progression of disease in these parts of the body. The decline in the mortality rate associated with the circulatory system diseases is attributed to medical and engineering advances to develop new diagnostic and prognostic tools using in-vivo, in-vitro and numerical investigations. Numerical studies have gained considerable attention in assessing the homodynamic condition associated with cardiovascular disease as they are less expensive and more flexible in applying more geometrical and hemodynamic variations.

The evolution of thoracic aorta simulations has followed a path similar to the coronary arteries and the aortic valve as discussed in sections 2.2 and 4.2 . Earlier attempts used idealized geometries such as a simple curved conduit of constant radius [168, 169]. Development of higher accuracy medical imaging led to the employment of the geometries with a larger degree of anatomic realism in the numerical studies. Recently, numerous investigations have been performed to understand the vascular hemodynamics in the thoracic aorta due to the aortic dissection and aneurysm using the patient specific models. [170-172]. As discussed in Chapter 5:, the pathologies of the aortic valve are thought to affect coronary blood flow. Furthermore, it is well established that abnormal aortic valve can give rise to pathologies of the thoracic aorta such as aortic dissection and aneurysm [173-175]. However, due to some limitation either using medical imaging modalities or numerical simulation, the underlying mechanisms in disease initiation and development due to regional hemodynamic conditions is not fully elucidated. As a result, in spite of clinical demand, so far none of the carried out investigations was successful in incorporating these adjacent structures into one numerical model. Hence, the goal of this chapter is to further develop the global model by including anatomically faithful thoracic aorta geometry including the aortic arch and its main branches. The notion of globality is introduced into the model because it enables investigating the hemodynamic changes in a global anatomy due to the regional pathologies.

7.3 The anatomical geometry of the thoracic

In order to include the most accurate geometrical model of the thoracic aorta in the global model, the Zygote Solid 3D Circulatory System (Zygote Media Group, Inc.) model was used which was discussed in section 4.3. This model was edited to include the particular parts and branches of the thoracic aorta. These structures were later added to the global model as descried in Chapter 4:.

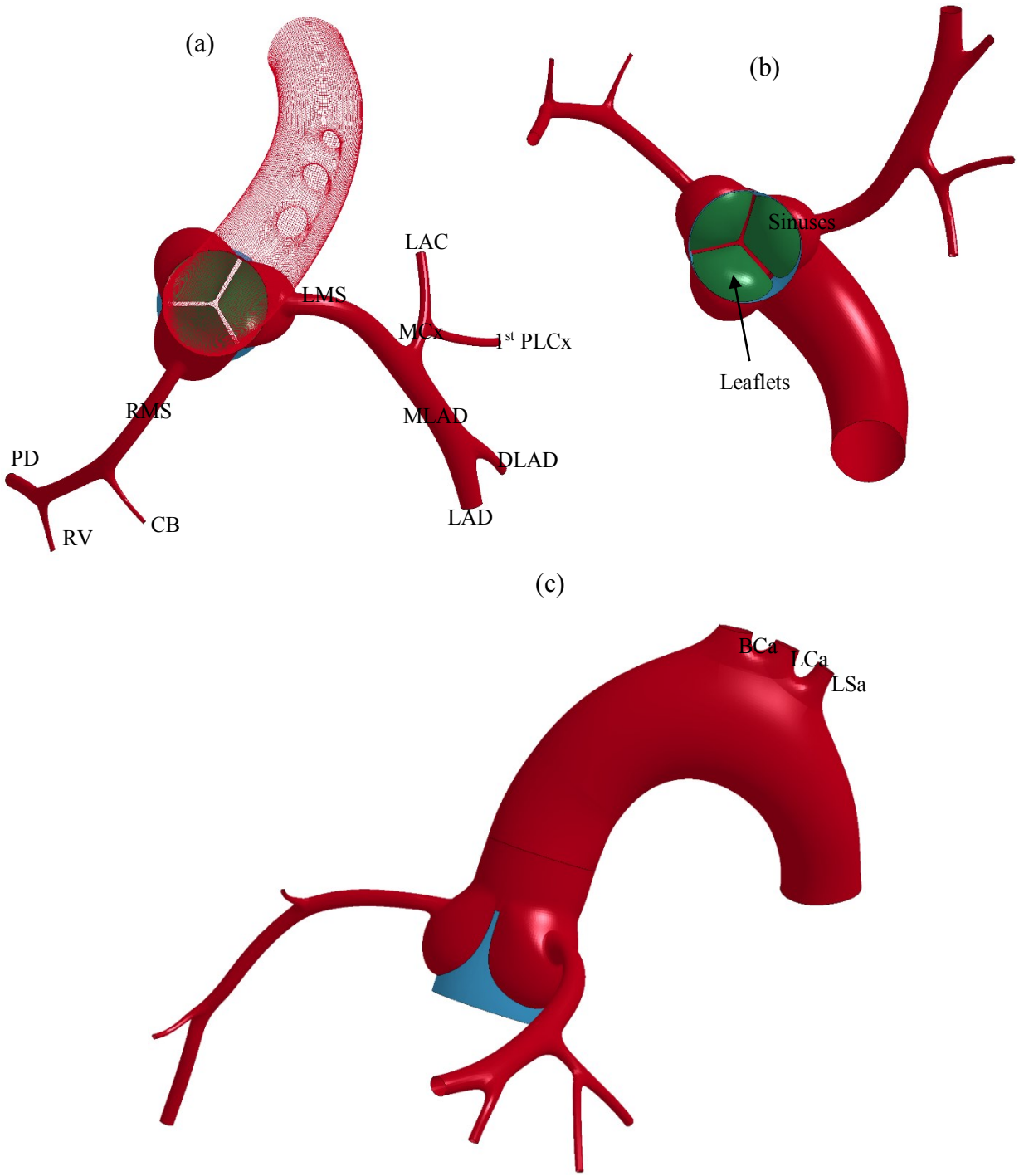

Figure 7.1:Schematic of the developed model seen form the: (a) position of the ascending aorta back towards the left ventricle, (b) position of the left ventricle back towards the aorta, (c): isometric view. To be noted that apparent gap between the cusps corresponds to the shell thickness. In the first frame, the ascending aorta is presented in transparent form in order to visualize the whole components of the model.

To illustrate the non-planar curvature and branching of the simulated thoracic aorta and the coronary structures, schematics of the solid domain of the model seen form different views is presented in Figure 7.1. The brachiocephalic artery (BCa), the left carotid artery (LCa) and the left subclavian (LSa) artery which branch off the aortic arch to feed the brain and arms were the simulated arteries on the thoracic aorta. As for the geometry of the fluid domain, the presented fluid domain in section 4.4 was expanded by fusing the geometry of the thoracic aorta with the same dimension as the solid domain. Dimension of the various components of the model are presented in Table 7.1. It should be noted that cross sectional area is measured at the outlet ring level of each artery.

Table 7.1: Dimension of the various compoentns of the thoracic aorta

Physical location	brachiocephalic artery	left carotid artery	left subclavian artery	Descending aorta
Cross sectional area (cm^2)	0.331	0.235	0.150	1.838

7.4 Finite element model

Similar to the normal aortic valve model, the constructed geometry was imported into a preprocessing software to be divided into separate parts and then be discretized for implementation of finite element analysis. The preprocessing steps were performed on the solid and fluid domains separately which are discussed in the following.

For the solid domain, the selected element type was the same as for the developed model in section 2.3.2.a. Mesh independency tests were performed to ensure convergence and obtain the minimum allowable element size. As a result, 45,721 quadrilateral elements were used for modeling the solid domain. The material property of the leaflets aortic wall and the coronaries was similar to the global model, section 4.4.1, and the same material property as the aortic wall was assigned to thoracic aorta. Furthermore, the blood on the fluid domain modeled using the selected material property for the normal aortic valve model which was discussed in section 2.3.3.b. In addition to the applied constraints to the global model in section 4.4.2, all outlets were fully constrained to restrict the motion and rotation in any direction to prevent rigid body motion and avoid unrealistic motions.

The fluid domain was composed of 830,846 unstructured elements which was observed to be adequate after performing mesh independency tests. Furthermore, the blood on the fluid domain modeled using the selected material property for the normal aortic valve model which was discussed in section 2.3.3.b. On the fluid domain, four sets of boundary conditions, including the time dependent physiological values of blood speed at the ventricular inlet corresponding to the cardiac flow of 5.07 L/min (Figure 7.2) as well as the difference between the transient physiological blood pressure waveforms corresponding to the outlets of the model, Figure 7.2, and the aortic pressure was imposed on the outlets [128, 176]. The duration of the simulated cardiac cycle is 0.85 s corresponding to a heart rate of 70 beats per minute.

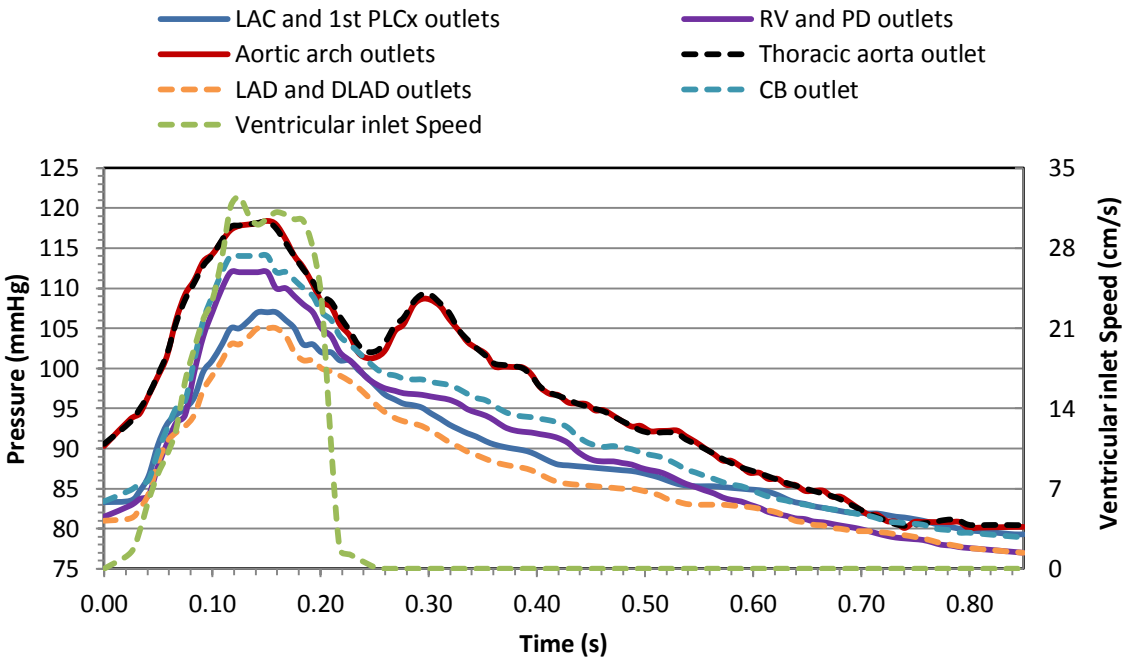

Figure 7.2:The physiological values of the blood speed and pressure various locations of the global model

7.5 Results of the global aortic root model including the thoracic aorta

Significant amount of temporal and spatial data can be generated with the proposed FSI model. However, in this study only the key results for the hemodynamics of the aortic valve, coronary arteries and the aorta are presented. Furthermore, the presented results are separated into structural and fluid sections.

7.5.1 The solid domain

Since the leaflets are more prone to pathologies such as tearing and calcification, Most of the clinical and engineering studies have placed their emphasis on the leaflets. Hence, the most accurate and available data exist for this component of the aortic valve region in solid domain. Hence, for verification on the solid domain, the leaflet morphologies, leaflet velocities, and leaflet stresses are chosen as the main relevant engineering parameters.

Figure 7.3 presents the computed leaflets morphologies at six discrete opening and closing times of the cardiac cycle. In this figure the vascular tissue is shown in transparent form to clearly see the valve configuration. The valve opens to 69% of the cross-sectional area of the aortic ring. Also, the calculated commissural expansion was 14.6% compared to the natural values of 12% showing good agreement with previous studies [86].

For a more quantitative assessment of the developed model, some clinical aspects of the leaflets tip velocity histories including the rapid valve opening time (RVOT), rapid valve opening velocity (RVOV), rapid valve closing time (RVCT), rapid valve closing velocity (RVCV), and ejection time (ET) were calculated. These parameters are commonly used for the clinical assessment of the outcome of the valve surgical procedures and the durability of the different prosthetics which could be quantified by echocardiography studies [87].

In Table 7.2, the derived values of the leaflets tip velocity histories are compared to those determined by echocardiography studies in healthy conditions (120/80 mmHg: $\Delta P = 40$ mmHg). The calculated results in terms of the leaflet dynamics as well as the valve motion pattern are in good agreement with the results of previous investigation and pulse duplicator observation [84, 130-132]. Compared to the normal aortic valve and the global model including only the coronaries, the valve opens slower which can be the results of imposing boundary conditions of the coronary structures. Furthermore, the observed leaflets stress distribution was similar to the normal healthy model.

Table 7.2: Comparison between the global model and echocardiography leaflets tip velocity histories

	RVOT (ms)	RVOV (cm/s)	RVCT (ms)	RVCV (cm/s)	ET (ms)
Global model	67.1	21.3	50.0	22.4	274
Echocardiography values	57.5 ± 11.3	29.2 ± 8.7	47.0 ± 11.1	23.6 ± 7	324 ± 70

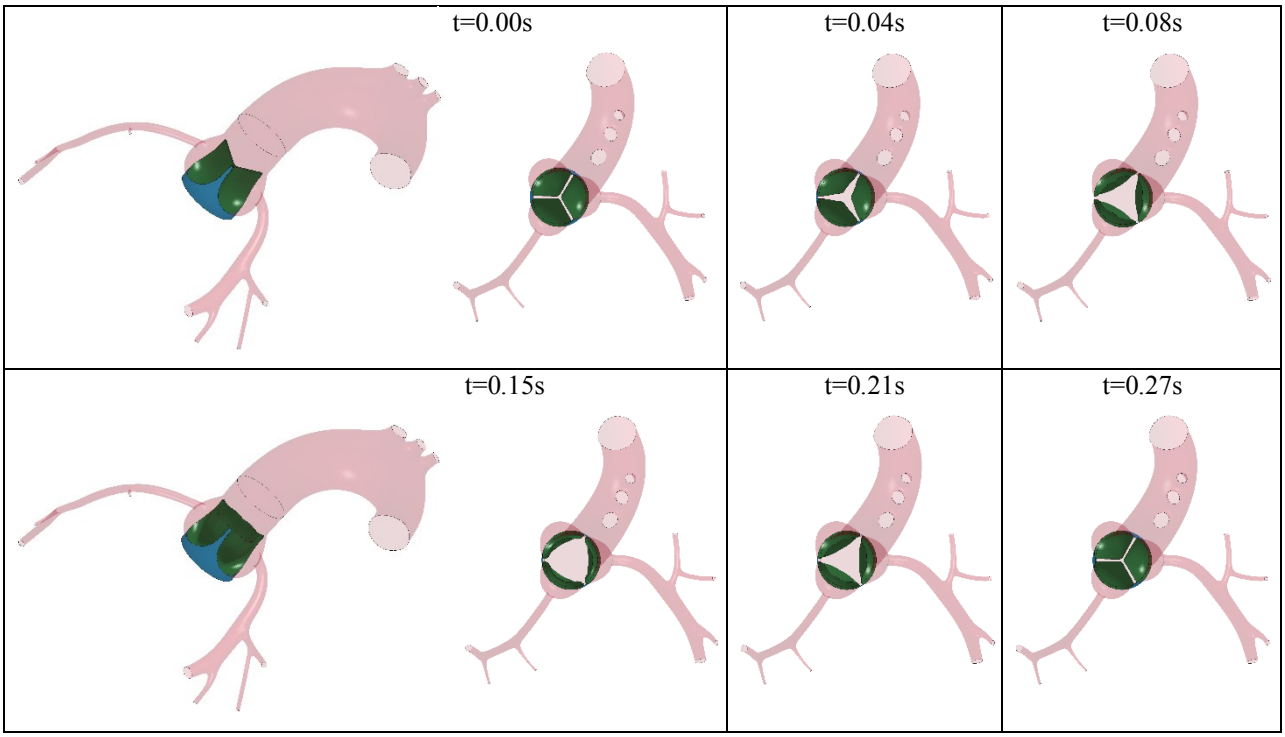

Figure 7.3: The computed leaflets morphologies, seen from aorta. The initial and maximum opening configuration of the valve is also shown in isometric view to better capture the shape of the valve (Note that at time t = 0.0 s, the leaflets are in full contact. And the apparent gap is due to the shell thickness)

7.5.2 Fluid domain

Verification of the fluid medium results can be accomplished to a certain degree by comparing the calculated results to known physiological data. In Figure 7.4, the resulted blood flow is visualized on isosurfaces form in mid-diastole when blood is ejected from the left ventricle to supply the myocardium and body through the coronary arteries and aorta.

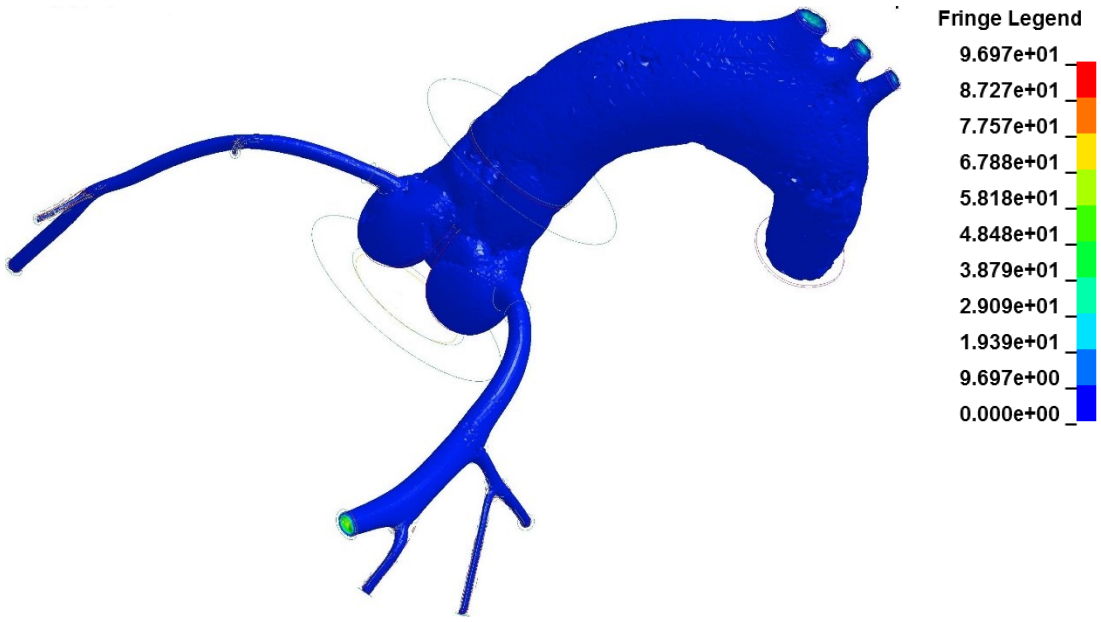

Figure 7.4: Visualized blood flow through the model in mid diastole (The unit of velocity is cm/s).

The axial blood velocities were sampled in the model at three locations: sinotubular junction (center of cross section 1 in Figure 7.6.a), ascending aorta (center of cross section 3 in Figure 7.6.a) and descending aorta (center of cross section 9 in Figure 7.6.a) which are presented in Figure 7.5.a. Moreover, the measured flow waveforms in coronary arteries as well as the aortic arch vessels are presented in Figure 7.5.b. Comparison to clinical data can be done over the entire cardiac cycle using the temporal distribution and total ejected flow. Although for the coronary and aortic arch branches flow the shape of the waveform is less precisely known, certain aspects, such as the total flow and the general shape, have been documented. The blood velocity in aorta reaches its peak value of 109.7 cm/s, a value in good agreement with the reported physiological peak velocity 135 ± 35 cm/s, during the systolic phase of the cycle and return to a magnitude very near zero during the diastolic phase. Moreover, the measured velocity of the blood during the maximum flow at the inlet level of the left coronary artery and right coronary artery was 29.7 cm/s 15.7 cm/s respectively [47, 134].

(a)

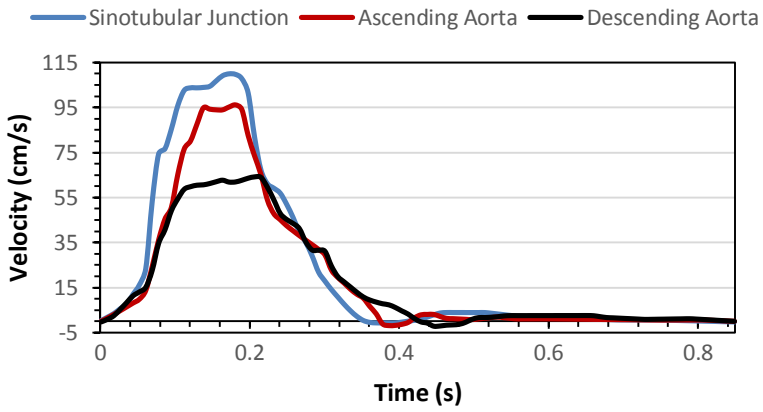

(b)

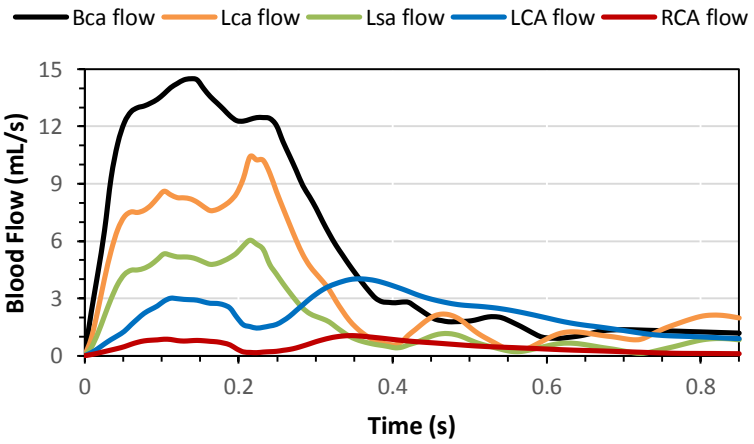

Figure 7.5: (a) The computed time dependent waveform of the blood velocity and blood flow (b) at various locations of the model

To visualize the velocity pattern at various locations of the model, a total of seventeen cross-sections (CSs) are defined as shown in Figure 7.6.a. It should be noted that the cross sections on thoracic aorta are seen in the direction of the blood flow. The visualized cross sectional blood velocity along the thoracic aorta corresponding to peak systole and coronary arteries corresponding to coronary peak flow on the selected cross sections are demonstrated in Figure 7.6.b and Figure 7.6.d while in Figure 7.6.c, to visualize the pattern of the blood flow leaving the aortic arch

to the brain and arms, its vector is used. The normal velocity vectors on the wall in this figure, are induced due to the wall deformation.

7.6 Discussion

Due to the prevalence of the pathologies of the aortic valve, coronary artery and thoracic aorta, these regions have been the main focus of many studies during the recent years. Some clinical investigations have recently reported a simultaneous structural and hemodynamic variation in the coronaries, the aortic root and thoracic aorta regions due to localized pathologies [140-142, 173, 175]. As the clinical studies are limited to explain these observed behaviors, numerical simulations have gained a considerable attention in assessing the homodynamic condition associated with cardiovascular diseases to elucidate the possible link between the regional cardiovascular pathologies and such global variations. Considering the interaction between the cardiac tissue and the blood is critical in investigating aortic root region. However, the inherent complexity associated with FSI modeling of the aortic root specially dealing with large deformation of the leaflets, has limited the studies undertaken in this area and there is a clear lack of a global representation of the aortic valve region incorporating the coronary arteries and thoracic aorta. To overcome this obstacle, in this study, a 3D global fluid-structure interaction model of the aortic valve including the anatomically realistic coronary vessels and thoracic aorta was developed. In order to reduce the numerical instabilities associated with low inertia vascular tissue in the blood domain, a strongly coupled strategy using implicit LS-DYNA was adopted. Furthermore, to stabilize the model to support the large deformation of the leaflets and generating precise results in the interface of the solid and fluid domain, combined fictitious domain (FD) and remeshing was selected to implement the interaction between the cardiac tissue and blood flow.

Results were obtained for the structural and the fluid domain separately. According to Figure 7.3, the leaflets opening during the systolic phase was associated with ballooning and tip fluttering, which was similar to clinical and physiological observations [61]. The maximum opening happened at $t = 0.15s$ into the cardiac cycle. These large deformations are the main source of complexity related to FSI modeling of the aortic root. Following the maximum opening of the leaflet, diastolic phase starts by closure of the valve and returning to its initial configuration. Since after complete closure, there was no variation observed in the leaflets morphology the remaining images of the valve related to the rest of the cardiac cycle were not included in Figure 7.3. Using

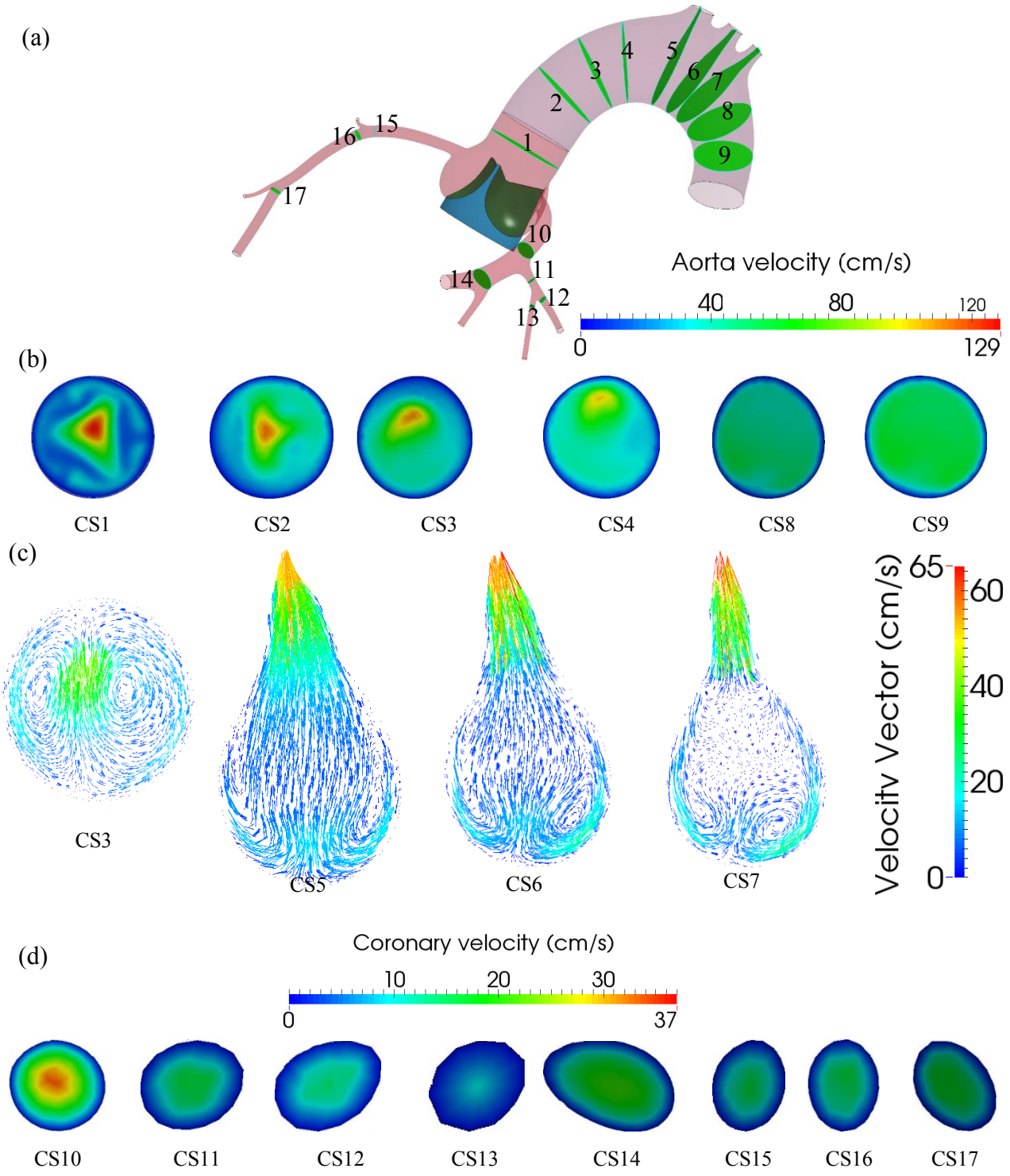

Figure 7.6: (a) Cross-sections at which velocity patterns are visualized and the corresponding numbering system used for identification. Crosse sectional blood velocity pattern observed along thoracic aorta at peak systole (b) and coronary arteries during their maximum flow (d). Axial and planar blood velocity pattern on the selected cross sections on aortic arch at peak systole (c)

the general morphology of the leaflets and aortic root during the cardiac cycle, relevant clinical indices including RVOT, RVOV, RVCT, RVCV and ET were calculated. These key clinical metrics quantify the opening and closing patterns of the leaflets. As presented in Table 7.2, the calculated values showed good agreements with clinical observations. Leaflet stresses and their distribution patterns were other verification aspects which were calculated at peak systole and diastole which were similar to the results of the normal model.

As for the fluid domain, perfusion level into the coronary ostia and aortic arch branches as well as the blood velocity in the aortic root and thoracic aorta were the parameters of interest which are provided in Figure 7.5. The waveform of the blood velocity at three points located progressively further from the left ventricle were sampled. These points correspond to the center of cross section 1 in the sinotubular junction, cross section 3 in ascending aorta and cross section 9 in descending aorta. The fluid displayed acceleration followed by a deceleration and then returned to a magnitude very near zero during the diastolic phase which is known to be the case physiologically. As depicted in Figure 7.5.a, at sinotubular junction level there was no negative values of flow indicating inexistence of backflow into the ventricular chamber due to the full contact between the leaflets during the diastolic phase of the cardiac cycle. A peak velocity of 109.7 m/s occurred during systole at the sinotubular junction level while as progressing along the thoracic aorta, this peak value was decreased indicating a good agreement with previous reports [47, 177]. The temporal waveforms of blood flow leaving the aorta to supply the myocardium and the superior regions of the body are illustrated in Figure 7.5.b. Out of 5.06 L/min pumped blood from the left ventricle about five percent was delivered to the coronaries while this value for BCa, LCa and LSa was 13.97, 8.69 and 4.81 respectively. The measured values and their temporal trend during a cardiac cycle were consistent with the average clinical observations [13, 110]

As can be seen from Figure 7.6, the maximum velocity of the flow occurred at the level of sinotubular junction (CS 1) along the aorta and in CS 10 before the first bifurcation of LCs among the defined CSs. Variations in velocity profile are enhanced as a result of artery curvature along the aorta and coronaries. At cross sections with no apparent curvatures, the velocity profiles were more uniform (CS1 and most of the defined CSs along the coronaries). While due to the existing abrupt curvatures in the aortic arch and its proximal and downstream regions, (CSs 2-8) the observed patterns in the velocity profile were not uniform. By decreasing the radius of curvature, the

maximum velocity shifted toward the outer curvature and a secondary peak was occurred along the inner curvature [178]. As the blood flow enters a curvature, since it should follow the bend, the radial pressure gradient between the inner and outer walls of the curved artery is generated which will lead to the development of the secondary flow a presented in Figure 7.6.c for the three CSs 3-7. Hemodynamic changes due to these curvatures is thought to link to development of localized cardiovascular disease [89, 170].

7.7 Conclusion

The developed model in this study was verified by comparing the calculated hemodynamic variables in both the solid and fluid domains with clinical and physiological observations. It is different from all the previous studies in the sense that inclusion of the coronary structures and thoracic aorta into the natural aortic valve introduces the notion of globality enabling us to explore the possible link between the regional pathologies which was impossible with previous models.

Chapter 8: Discussion and conclusion

In this chapter, the original contributions of this study is highlighted and the general conclusion and discussion of the obtained results is provided. In addition, the limitations and assumptions of our research as well as some recommendations for the possible future work is discussed.

8.1 Original contributions

The hypothesis and all objectives defined in the beginning of this study are addressed. The achieved original contributions are summarized as the following:

- To the best of the author's knowledge, the developed global model is the first three dimensional, FSI model of the aortic valve incorporating the natural leaflet, coronary structures and thoracic aorta. It is different from all the previous studies in the sense that inclusion of the coronary structures and thoracic aorta into the natural aortic valve introduces the notion of globality enabling to explore the possible link between the regional pathologies which was not possible with previous models.
- A global index to assess the regional hemodynamic conditions in the aortic root based on surrogate variables was derived. The proposed model allows a distinction between cases with similar low flow conditions but with different wall compliance. Indeed, the proposed dynamic biomechanical model incorporates the dynamic effects of the arterial compliance while current models do not take into account these effects.
- The clinically observed link between valvular pathologies and coronary flow was assessed and confirmed. The results revealed that in patients with severe and critical aortic stenosis, coronary arteries are prone for localizing early atherosclerotic plaque and its potential is higher on the right coronary vessels.
- Multiple FFR measurement was performed to investigate the mechanism of interaction between multiple coronary lesions with varying severities located on different coronary vessels to improve the understanding of the formation and development of coronary plaques. For a functional analysis of the plaques, the impact of the lesions location as well as their severity was investigated. The branch steal was observed to be an important phenomenon in the setting of either a single lesion in downstream

branches or a LMS plaque concomitant with a downstream lesion which could lead to further development of atherosclerotic lesions by alteration of WSS.

8.2 Discussion

Circulatory system diseases are prevalent and more than 80 percent of circulatory system deaths in high income countries are due to diseases of the aortic valve, coronary arteries and the blood vessels supplying the brain. In addition to considerable difficulties for patients and affecting quality of their life caused by the diseases of the circulatory system, they have a significant economic cost. In recent clinical studies, it is proven that impairment of the aortic valve can lead to development of the atherosclerotic lesion. Furthermore, it is well established that abnormal aortic valve can give rise to pathologies of the thoracic aorta such as aortic dissection and aneurysm. However, due to the limitations of the current tools, the underlying mechanism in diseases initiation and development due to regional hemodynamic conditions is not fully elucidated. Dealing with inherent complexity associated with large deformation of the leaflets during the systolic phase of the cardiac cycle is proven to be a challenging task and fusing the thoracic aorta and coronary arteries to the aortic valve model increases this complexity. As a result in spite to clinical demand, so far none of the carried out investigations was successful in incorporating these adjacent structures into one numerical model. Hence, the goal of this study is developing an anatomically faithful 3D global FSI model incorporating the natural cusps of the aortic valve, sinuses, thoracic aorta including aortic arch and its main branches as well as the coronary arteries with their main branches. The notion of globality is introduced into the model because it enables investigating the hemodynamic changes in a global anatomy due to the regional pathologies.

The combined ALE and FD methods were implemented to strongly couple the fluid and solid domains which led to improved stability of the model under large deformations. In a first step, in Chapter 2:, the normal aortic root including two coronary ostia was created. There was no instability problem in the course of the cardiac cycle and the model was run completely without numerical problems. The obtained results were verified qualitatively and quantitatively in both domains and were in good agreement with previous numerical and clinical data. In Chapter 3:, to assess the regional hemodynamic conditions in the aortic root due to pathologies of the valve, a theoretical model of the transient viscous blood flow across the aortic stenosis taking into account

the aorta compliance was derived. The derived relation of the new TPG was expressed in terms of clinically available surrogate variables (anatomical and hemodynamic data). Then by using the developed FSI model of the aortic root, the derived relation of the new TPG was expressed in terms of clinically available surrogate variables (anatomical and hemodynamic data). The derived model was assessed using the results from the literature. The results showed that the proposed relation provides physiologically compatible results even for cases for which current models fail (low flow). This generalized model can be used to estimate the effective valve orifice area for determining the severity of the stenosis in cases where the tissue still has compliance. Reported results in the literature were obtained with models that attempt to incorporate a static estimate of the arterial compliance using indirect Doppler measurement based on an averaged ratio of the stroke index to brachial pulse pressure. With this approach, it is difficult to distinguish patients with low-flow/low gradient with true severe aortic stenosis or more moderate degrees of aortic stenosis. For diagnostic and prognostic purposes a better distinction between the two conditions would be beneficial. The proposed model allows a distinction between cases with similar low flow conditions but with different wall compliance. Indeed, the proposed dynamic biomechanical model incorporates the dynamic effects of the arterial compliance while current models do not take into account these effects. Given that the models are different, the comparison was made on the basis of the pressure gradient estimations.

Then, in Chapter 4:, the normal aortic root was further developed to include the anatomical coronary arteries and their main branches as a global model. The calculated variables in the solid domain (leaflet morphologies, Leaflets dynamics and leaflets stress) and fluid domain (blood velocity vector, blood velocity profile, coronary blood supply, wall shear stress on the coronary vessels) were assessed both qualitatively and quantitatively. This proposed model has the potential to investigate the possible causal effect of the aortic valve abnormalities on the coronary vessels pathologies, occlusion of the critical small coronary vessels and its effect on the heart muscle. Such investigations are not possible with previously developed models of the aortic root without the coronary arteries or simplified structure as the coronary vessels. To do this, in Chapter 5:, the stenosed aortic valve models were simulated by constraining the motion of leaflets tip on the global model. The results revealed significant impact on coronary hemodynamics due to the constriction of the aortic valve. And a continuous drop in WSS and blood velocity was detected with progression of the aortic stenosis. It can be concluded from the obtained results that in patients

with severe and critical aortic stenosis, coronary arteries are prone for localizing early atherosclerotic plaque and its risk is higher on the right coronary vessels. These findings confirm the recent clinical studies.

In Chapter 6:, the developed global model was used to perform multiple FFR measurement and investigate the mechanism of interaction between multiple coronary lesions with varying severities located on different coronary vessels and improve the understanding of the formation and development of coronary plaques. For a functional analysis of the plaques, the impact of the lesions location as well as their severity was investigated. Based on the Medina classification, six plaque configurations were defined and the calcified plaques were generated. Progressive lesions from mild to severe were constructed on the left coronary arteries while the severity of the all constrictions on each configuration was identical. It was different from all the recent works in the sense that the use of the global model could give better insight into hemodynamic of multi-vessel plaques to improve the current strategies and devices. The results indicated that occlusion of the LMS could lead to significant difficulties and considerable alteration of WSS in downstream regions. Furthermore, the branch steal was observed to be an important phenomenon in the setting of either a single lesion in downstream branches or a LMS plaque concomitant with a downstream lesion which could lead to further development of atherosclerotic lesions by alteration of WSS.

As the last step, in Chapter 7:, the anatomically faithful thoracic aorta including aortic arch and its main branches was fused to the developed global model. The calculated results were verified by comparing the calculated hemodynamic variables in both the solid and fluid domains with clinical and physiological observations. This model could serve as a mean to enhance our understanding of the initiation and progression of cardio vascular diseases in the corresponding regions of the body.

8.3 Conclusion

In summary, we addressed the hypothesis of this thesis which was developing a 3D global fluid-structure interaction of the aortic root with inclusion of anatomically inspired coronary vessels and the thoracic aorta to derive a global index for assessing the regional hemodynamic conditions in the aortic root based on surrogate variables and investigate the possible interaction between coronary artery pathologies and aortic valve pathologies. To the best of our knowledge, this is the first global 3D FSI model of the aortic root incorporating the natural leaflet structure, two coronary arteries and thoracic aorta. It is different from all the previous studies in the sense

that inclusion of the coronary structures and thoracic aorta into the natural aortic valve introduces the notion of globality enabling us to explore the possible link between the regional pathologies which was impossible with previous models. By means of this model, all defined objectives were met.

8.4 Limitations and future work

Dealing with a complex model like the developed global model in this thesis is always associated with assumptions and simplifications inevitably. The assumptions in this study generally can be expressed in terms of geometry construction and numerical analysis.

Due to the variability and limited available data related to aortic valve dimensions, the geometry of the root is simplified to some extent as investigating the generic behavior was the main aspect of this study not patient specific cases. Furthermore, since some structures of the root even using the high quality medical imaging modalities remain hidden interpolation is required to reconstruct those hidden areas. Hence, as discussed, the aortic root of the model presented in this thesis is constructed using the average values of key locations reported in the literature. However, a parameterized geometry of the valve is useful for aiding in surgical planning.

In addition to stability issues associated with modeling the large displacements of the aortic leaflets, computational cost is another reason for computational assumptions made in the study. Even by using massively parallel processing (MPP) capabilities of LS-DYNA to shorten the necessary time to run the model by means of the facilities of the Shared Hierarchical Academic Research Computing Network (SHARCNET: www.sharcnet.ca) and Compute/Calcul Canada, the calculation times for a single simulation would average to 6 days using 12 processors with 6 Gb of memory. In this study the linear elastic material properties was used for the cardiac tissue. However, it was shown that the nonlinear stress-strain curve of the cardiac tissue can be approximated by two linear regions: one at low strain range (below 15%) and another at high strain rates while this linearity is even more strong at low strain rates and under normal physiological conditions, the strain in the aortic root varies in the range of about 10%. Consequently, using linear material property for the numerical simulation of the cardiac tissue under physiological conditions is proven to be adequate. However, for applications like investigating the aneurism rupture process and integrating the vascular microstructures, the assumption of an isotropic material model should be generalized to anisotropic model to take into account for the large deformations.

Another simplification that was done is in the imposed pressure boundary conditions at the outlets of the model. The aortic pressure waveform was chosen as the reference and all imposed pressure waveforms were taken to be the difference between corresponding physiological pressure and the aortic pressure. This method was borrowed from literature to avoid the instabilities issues reduce extremely long computation times. Hence, due to this assumption, the entire system was under an overall smaller pressure while maintaining the pressure gradient across the valves. As a result, the calculated commissural expansions were less than the physiological values.

The coronary blood pressure and flow depend strongly on downstream resistance which is regulated by factors like myocardial oxygen demand and aortic pressure. As in this study, investigating the impact of the valvular impairment on coronary flow perturbations was the main object, maintaining outlet pressure was an adequate approach as it allows isolating a single variable at a time. Therefore, autoregulation and vasodilation/contraction of the coronaries were not incorporated into the model which needs to be addressed in future work.

As discussed, significant amount of temporal and spatial data can be generated by the developed complex FSI model. However, in this study only the most relevant results to the hemodynamics of the aortic valve, coronary arteries and the aorta especially those related to the fluidic aspect of the model are presented. While analyzing the resulted values of the stress and deformation on the cardiac tissue could be interesting for future work. The results from the simulated model were assessed using clinical and previously published data in the literature. Since the clinical validation of developed model require a significant amount of time, effort and financial support, it was out of the scope of this research. However, it could be considered in future work to perform sensitivity analysis and experimental.

References

[1] S. Whittemore, and Denton A. Cooley, M.D, The Human Body- How It Works: The Respiratory System. , 1 ed.
[2] R.J. Brewer, J.D. Deck, B. Capati, S.P. Nolan, The dynamic aortic root. Its role in aortic valve function, J. Thorac. Cardiovasc. Surg., 72 (1976) 413-417.
[3] M. Thubrikar, S.P. Nolan, L.P. Bosher, J.D. Deck, The cyclic changes and structure of the base of the aortic valve, Am. Heart J., 99 (1980) 217-224.
[4] A.S. Go, D. Mozaffarian, V.L. Roger, E.J. Benjamin, J.D. Berry, W.B. Borden, D.M. Bravata, S. Dai, E.S. Ford, C.S. Fox, S. Franco, H.J. Fullerton, C. Gillespie, S.M. Hailpern, J.A. Heit, V.J. Howard, M.D. Huffman, B.M. Kissela, S.J. Kittner, D.T. Lackland, J.H. Lichtman, L.D. Lisabeth, D. Magid, G.M. Marcus, A. Marelli, D.B. Matchar, D.K. McGuire, E.R. Mohler, C.S. Moy, M.E. Mussolino, G. Nichol, N.P. Paynter, P.J. Schreiner, P.D. Sorlie, J. Stein, T.N. Turan, S.S. Virani, N.D. Wong, D. Woo, M.B. Turner, C. American Heart Association Statistics, S. Stroke Statistics, Heart disease and stroke statistics--2013 update: a report from the American Heart Association, Circulation, 127 (2013) e6-e245.
[5] J.D. Hutcheson, E. Aikawa, W.D. Merryman, Potential drug targets for calcific aortic valve disease, Nature reviews. Cardiology, 11 (2014) 218-231.
[6] A.B.T.M. Wang, Valvular heart disease, in, Humana Press, Dordrecht; New York, 2009.
[7] Z. Wa., C.M. H., CURRENT Diagnosis & Treatment: Cardiology, 3 ed., Retrieved April 07, 2014 from http://accessmedicine.mhmedical.com/content.aspx?bookid=334&Sectionid=39690506., 2009.
[8] R.A. Nishimura, C.M. Otto, R.O. Bonow, B.A. Carabello, J.P. Erwin, R.A. Guyton, P.T. O'Gara, C.E. Ruiz, N.J. Skubas, P. Sorajja, T.M. Sundt, J.D. Thomas, 2014 AHA/ACC Guideline for the Management of Patients With Valvular Heart DiseaseA Report of the American College of Cardiology/American Heart Association Task Force on Practice Guidelines, J. Am. Coll. Cardiol., (2014).
[9] Z.M. Gertz, A. Raina, W. O'Donnell, B.D. McCauley, C. Shellenberger, D.M. Kolansky, R.L. Wilensky, P.R. Forfia, H.C. Herrmann, Comparison of invasive and noninvasive assessment of aortic stenosis severity in the elderly, Circulation. Cardiovascular interventions, 5 (2012) 406-414.
[10] E.R. Bates, Treatment options in severe aortic stenosis, Circulation, 124 (2011) 355-359.
[11] B.A. Carabello, W.J. Paulus, Aortic stenosis, The Lancet, 373 956-966.
[12] P. Pibarot, J.G. Dumesnil, Prosthetic heart valves: selection of the optimal prosthesis and long-term management, Circulation, 119 (2009) 1034-1048.
[13] M. Zamir, The physics of coronary blood flow, in, Springer, New York, 2005.
[14] T. Ramanathan, H. Skinner, Coronary blood flow, Continuing Education in Anaesthesia, Critical Care & Pain, 5 (2005) 61-64.
[15] Leading Causes of Death and Hospitalization in Canada, in, Public Health Agency of Canada, http://www.phac-aspc.gc.ca/, January 23, 2012.
[16] L. National Heart, and Blood Institute, Morbidity & Mortality: 2012 Chartbook on Cardiovascular, Lung, and Blood Diseases, 2012.
[17] P.L. Weissberg, Atherogenesis: current understanding of the causes of atheroma, Heart, 83 (2000) 247-252.
[18] I.Y. Elgendy, C.R. Conti, A.A. Bavry, Fractional Flow Reserve: An Updated Review, Clinical Cardiology, (2014) n/a-n/a.
[19] B. De Bruyne, J. Sarma, Fractional flow reserve: a review: invasive imaging, Heart, 94 (2008) 949-959.
[20] R.M.L.M.N. Berne, Cardiovascular physiology, Mosby, St. Louis, MO, 2001.
[21] J.Y. Moon, J.W. Chung, J.H. Kim, Y.K. Ahn, M.H. Jeong, Simultaneous subacute stent thrombosis of two sirolimus-eluting stents in a patient treated by ReoPro, thrombus aspiration and triple anti-platelet agents, Int. J. Cardiol., 130 (2008) e25-29.
[22] F. Dagenais, Anatomy of the thoracic aorta and of its branches, Thoracic surgery clinics, 21 (2011) 219-227, viii.
[23] D. Guo, S. Hasham, S.Q. Kuang, C.J. Vaughan, E. Boerwinkle, H. Chen, D. Abuelo, H.C. Dietz, C.T. Basson, S.S. Shete, D.M. Milewicz, Familial thoracic aortic aneurysms and dissections: genetic heterogeneity with a major locus mapping to 5q13-14, Circulation, 103 (2001) 2461-2468.
[24] E.M. Isselbacher, Thoracic and abdominal aortic aneurysms, Circulation, 111 (2005) 816-828.
[25] J.A. Cowan, Jr., J.B. Dimick, P.K. Henke, T.S. Huber, J.C. Stanley, G.R. Upchurch, Jr., Surgical treatment of intact thoracoabdominal aortic aneurysms in the United States: hospital and surgeon volume-related outcomes, J. Vasc. Surg., 37 (2003) 1169-1174.

[26] T.L.W.K.M.B. Belytschko, Nonlinear finite elements for continua and structures, Wiley, Chichester; New York, 2000.
[27] N. Qi, Y. Nie, W. Zhang, Acceleration Strategies Based on an Improved Bubble Packing Method, (2014).
[28] S. Yip, Handbook of materials modeling, Springer, Dordrecht, 2005.
[29] G. Hou, J. Wang, A. Layton, Numerical methods for fluid–structure interaction—a review, Commun Comput Phys, 12 (2012) 337-377.
[30] P.B. Ryzhakov, R. Rossi, S.R. Idelsohn, E. Oñate, A monolithic Lagrangian approach for fluid–structure interaction problems, Comput Mech, 46 (2010) 883-899.
[31] R. van Loon, P.D. Anderson, F.N. van de Vosse, S.J. Sherwin, Comparison of various fluid–structure interaction methods for deformable bodies, Computers & Structures, 85 (2007) 833-843.
[32] J.O. Hallquist, LS-DYNA THEORY MANUAL in, Livermore Software Technology Corporation, March 2006.
[33] C.W. Hirt, A.A. Amsden, J.L. Cook, An arbitrary Lagrangian-Eulerian computing method for all flow speeds, Journal of Computational Physics, 14 (1974) 227-253.
[34] J. Donea, S. Giuliani, J.P. Halleux, An arbitrary lagrangian-eulerian finite element method for transient dynamic fluid-structure interactions, Computer Methods in Applied Mechanics and Engineering, 33 (1982) 689-723.
[35] R. Glowinski, T.W. Pan, T.I. Hesla, D.D. Joseph, A distributed Lagrange multiplier/fictitious domain method for particulate flows, International Journal of Multiphase Flow, 25 (1999) 755-794.
[36] R. Glowinski, T.-W. Pan, T.I. Hesla, D.D. Joseph, J. Périaux, A distributed Lagrange multiplier/fictitious domain method for flows around moving rigid bodies: Application to particulate flow, International Journal for Numerical Methods in Fluids, 30 (1999) 1043-1066.
[37] F. Bertrand, P.A. Tanguy, F. Thibault, A three-dimensional fictitious domain method for incompressible fluid flow problems, International Journal for Numerical Methods in Fluids, 25 (1997) 719-736.
[38] R. van Loon, P.D. Anderson, J. de Hart, F.P.T. Baaijens, A combined fictitious domain/adaptive meshing method for fluid–structure interaction in heart valves, International Journal for Numerical Methods in Fluids, 46 (2004) 533-544.
[39] Z. Yu, A DLM/FD method for fluid/flexible-body interactions, Journal of Computational Physics, 207 (2005) 1-27.
[40] K.-J.r.B.K.-J.r. Bathe, Finite element procedures, Prentice Hall, Englewood Cliffs, N.J., 1996.
[41] J.N. Reddy, An introduction to the finite element method, McGraw-Hill, New York, 1993.
[42] L.A. Freitag, C. Ollivier-Gooch, Tetrahedral mesh improvement using swapping and smoothing, International Journal for Numerical Methods in Engineering, 40 (1997) 3979-4002.
[43] LSTC, Incompressible fluid solver in LS-DYNA, in, LIVERMORE SOFTWARE TECHNOLOGY CORPORATION (LSTC) February, 2013.
[44] M.P. Rossow, P.L. Gould, R.E. Clark, A simple method for estimating stresses in natural and prosthetic heart valves, Biomater. Med. Devices Artif. Organs, 6 (1978) 277-290.
[45] M. Thubrikar, W.C. Piepgrass, J.D. Deck, S.P. Nolan, Stresses of natural versus prosthetic aortic valve leaflets in vivo, Ann. Thorac. Surg., 30 (1980) 230-239.
[46] P.L. Gould, A. Cataloglu, G. Dhatt, A. Chattopadhyay, R.E. Clark, Stress analysis of the human aortic valve, Computers & Structures, 3 (1973) 377-384.
[47] A. Cataloglu, P.L. Gould, R.E. Clark, Validation of a simplified mathematical model for the stress analysis of human aortic heart valves, J. Biomech., 8 (1975) 347-348.
[48] G. Christie, I. Medland, A non-linear finite element stress analysis of bioprosthetic heart valves, Wiley, New York, 1982.
[49] H.N. Sabbah, M.S. Hamid, P.D. Stein, Estimation of mechanical stresses on closed cusps of porcine bioprosthetic valves: effects of stiffening, focal calcium and focal thinning, Am. J. Cardiol., 55 (1985) 1091-1096.
[50] H.N. Sabbah, M.S. Hamid, P.D. Stein, Mechanical stresses on closed cusps of porcine bioprosthetic valves: correlation with sites of calcification, Ann. Thorac. Surg., 42 (1986) 93-96.
[51] M.S. Hamid, H.N. Sabbah, P.D. Stein, Influence of stent height upon stresses on the cusps of closed bioprosthetic valves, J. Biomech., 19 (1986) 759-769.
[52] M.S. Hamid, H.N. Sabbah, P.D. Stein, Finite element evaluation of stresses on closed leaflets of bioprosthetic heart valves with flexible stents, Finite Elements in Analysis and Design, 1 (1985) 213-225.
[53] M.M. Black, I.C. Howard, X. Huang, E.A. Patterson, A three-dimensional analysis of a bioprosthetic heart valve, J. Biomech., 24 (1991) 793-801.
[54] J. De Hart, G.W. Peters, P.J. Schreurs, F.P. Baaijens, A two-dimensional fluid-structure interaction model of the aortic valve [correction of value], J. Biomech., 33 (2000) 1079-1088.

[55] K.S. Kunzelman, R.P. Cochran, C. Chuong, W.S. Ring, E.D. Verrier, R.D. Eberhart, Finite element analysis of the mitral valve, J. Heart Valve Dis., 2 (1993) 326-340.
[56] K.S. Kunzelman, M.S. Reimink, R.P. Cochran, Annular dilatation increases stress in the mitral valve and delays coaptation: a finite element computer model, Cardiovasc. Surg., 5 (1997) 427-434.
[57] K.S. Kunzelman, M.S. Reimink, R.P. Cochran, Flexible versus rigid ring annuloplasty for mitral valve annular dilatation: a finite element model, J. Heart Valve Dis., 7 (1998) 108-116.
[58] K.S. Kunzelman, D.R. Einstein, R.P. Cochran, Fluid-structure interaction models of the mitral valve: function in normal and pathological states, Philos. Trans. R. Soc. Lond. B. Biol. Sci., 362 (2007) 1393-1406.
[59] E.A. Patterson, I.C. Howard, M.A. Thornton, A comparative study of linear and nonlinear simulations of the leaflets in a bioprosthetic heart valve during the cardiac cycle, J. Med. Eng. Technol., 20 (1996) 95-108.
[60] G.G. Chew, I.C. Howard, E.A. Patterson, Simulation of damage in a porcine prosthetic heart valve, J. Med. Eng. Technol., 23 (1999) 178-189.
[61] J. De Hart, G.W. Peters, P.J. Schreurs, F.P. Baaijens, A three-dimensional computational analysis of fluid-structure interaction in the aortic valve, J. Biomech., 36 (2003) 103-112.
[62] J. De Hart, G.W. Peters, P.J. Schreurs, F.P. Baaijens, Collagen fibers reduce stresses and stabilize motion of aortic valve leaflets during systole, J. Biomech., 37 (2004) 303-311.
[63] H.J. Kim, I.E. Vignon-Clementel, J.S. Coogan, C.A. Figueroa, K.E. Jansen, C.A. Taylor, Patient-specific modeling of blood flow and pressure in human coronary arteries, Ann. Biomed. Eng., 38 (2010) 3195-3209.
[64] A. Ranga, O. Bouchot, R. Mongrain, P. Ugolini, R. Cartier, Computational simulations of the aortic valve validated by imaging data: evaluation of valve-sparing techniques, Interact Cardiovasc Thorac Surg, 5 (2006) 373-378.
[65] S. Nobari, R. Mongrain, E. Gaillard, R. Leask, R. Cartier, Therapeutic vascular compliance change may cause significant variation in coronary perfusion: a numerical study, Comput Math Methods Med, 2012 (2012) 791686.
[66] K. Lozsadi, A. Arvay, Comparative anatomical investigations on the heterotransplantation of the aortic valve, Acta Chir. Acad. Sci. Hung., 10 (1969) 207-214.
[67] J.L. Mercer, M. Benedicty, H.T. Bahnson, The geometry and construction of the aortic leaflet, J. Thorac. Cardiovasc. Surg., 65 (1973) 511-518.
[68] M.P. Sands, E.A. Rittenhouse, H. Mohri, K.A. Merendino, An anatomical comparison of human pig, calf, and sheep aortic valves, Ann. Thorac. Surg., 8 (1969) 407-414.
[69] M. Swanson, R.E. Clark, Dimensions and geometric relationships of the human aortic valve as a function of pressure, Circ. Res., 35 (1974) 871-882.
[70] K.S. Kunzelman, K.J. Grande, T.E. David, R.P. Cochran, E.D. Verrier, Aortic root and valve relationships. Impact on surgical repair, J. Thorac. Cardiovasc. Surg., 107 (1994) 162-170.
[71] S.J. Choo, G. McRae, J.P. Olomon, G. St George, W. Davis, C.L. Burleson-Bowles, D. Pang, H.H. Luo, D. Vavra, D.T. Cheung, J.H. Oury, C.M. Duran, Aortic root geometry: pattern of differences between leaflets and sinuses of Valsalva, J. Heart Valve Dis., 8 (1999) 407-415.
[72] D. Berdajs, P. Lajos, M. Turina, The anatomy of the aortic root, Cardiovasc. Surg., 10 (2002) 320-327.
[73] J. Abrams, The aortic valve by Mano Thubrikar Crc Press, Inc., Boca Raton (1990) 221 pages, illustrated, $97.50 ISBN: 0–8493–4771–8, Clin. Cardiol., 14 (1991) 364a-365.
[74] D. Tremblay, T. Zigras, R. Cartier, L. Leduc, J. Butany, R. Mongrain, R.L. Leask, A comparison of mechanical properties of materials used in aortic arch reconstruction, Ann. Thorac. Surg., 88 (2009) 1484-1491.
[75] M. Gur, R. Yilmaz, R. Demirbag, A. Yildiz, M. Menduh Bas, M. Polat, Relationship between impaired elastic properties of aorta with left ventricle geometric patterns and left ventricle diastolic functions in patients with newly diagnosed essential hypertension, Int. J. Clin. Pract., 60 (2006) 1357-1363.
[76] Y. Oishi, Y. Mizuguchi, H. Miyoshi, A. Iuchi, N. Nagase, T. Oki, A novel approach to assess aortic stiffness related to changes in aging using a two-dimensional strain imaging, Echocardiography, 25 (2008) 941-945.
[77] A. Beck, M.J. Thubrikar, F. Robicsek, Stress analysis of the aortic valve with and without the sinuses of valsalva, J. Heart Valve Dis., 10 (2001) 1-11.
[78] E.S. Di Martino, G. Guadagni, A. Fumero, G. Ballerini, R. Spirito, P. Biglioli, A. Redaelli, Fluid-structure interaction within realistic three-dimensional models of the aneurysmatic aorta as a guidance to assess the risk of rupture of the aneurysm, Med. Eng. Phys., 23 (2001) 647-655.
[79] G.B. Thurston, Viscoelasticity of Human Blood, Biophys. J., 12 (1972) 1205-1217.
[80] G.B. Thurston, Frequency and shear rate dependence of viscoelasticity of human blood, Biorheology, 10 (1973) 375-381.

[81] S. Chien, S. Usami, R.J. Dellenback, M.I. Gregersen, L.B. Nanninga, M.M. Guest, Blood viscosity: influence of erythrocyte aggregation, Science, 157 (1967) 829-831.
[82] S.A.G.W.L.E.R. Berger, Introduction to bioengineering, Oxford University Press, Oxford; New York, 1996.
[83] Y.C.C.S. Fung, Introduction to bioengineering, World Scientific, Singapore; River Edge, NJ, 2001.
[84] C.J. Carmody, G. Burriesci, I.C. Howard, E.A. Patterson, An approach to the simulation of fluid-structure interaction in the aortic valve, J. Biomech., 39 (2006) 158-169.
[85] V.C. Sripathi, R.K. Kumar, K.R. Balakrishnan, Further insights into normal aortic valve function: role of a compliant aortic root on leaflet opening and valve orifice area, Ann. Thorac. Surg., 77 (2004) 844-851.
[86] J. De Hart, F.P. Baaijens, G.W. Peters, P.J. Schreurs, A computational fluid-structure interaction analysis of a fiber-reinforced stentless aortic valve, J. Biomech., 36 (2003) 699-712.
[87] T. Aybek, M. Sotiriou, T. Wohleke, A. Miskovic, A. Simon, M. Doss, S. Dogan, G. Wimmer-Greinecker, A. Moritz, Valve opening and closing dynamics after different aortic valve-sparing operations, J. Heart Valve Dis., 14 (2005) 114-120.
[88] T.T.S. Kazui, Advances in understanding aortic diseases, in, Springer, Tokyo; New York, 2009.
[89] S. Nobari, R. Mongrain, R. Leask, R. Cartier, The effect of aortic wall and aortic leaflet stiffening on coronary hemodynamic: a fluid-structure interaction study, Med Biol Eng Comput, (2013).
[90] M. Handke, G. Heinrichs, F. Beyersdorf, M. Olschewski, C. Bode, A. Geibel, In vivo analysis of aortic valve dynamics by transesophageal 3-dimensional echocardiography with high temporal resolution, J. Thorac. Cardiovasc. Surg., 125 (2003) 1412-1419.
[91] M.H. Olsen, K. Wachtell, J.N. Bella, J.E. Liu, K. Boman, E. Gerdts, V. Papademetriou, M.S. Nieminen, J. Rokkedal, B. Dahlof, R.B. Devereux, Effect of losartan versus atenolol on aortic valve sclerosis (a LIFE substudy), Am. J. Cardiol., 94 (2004) 1076-1080.
[92] M.H. Olsen, K. Wachtell, J.N. Bella, E. Gerdts, V. Palmieri, M.S. Nieminen, G. Smith, H. Ibsen, R.B. Devereux, L. substudy, Aortic valve sclerosis relates to cardiovascular events in patients with hypertension (a LIFE substudy), Am. J. Cardiol., 95 (2005) 132-136.
[93] C.M. Otto, Why is aortic sclerosis associated with adverse clinical outcomes?, J. Am. Coll. Cardiol., 43 (2004) 176-178.
[94] R. Heinrich, A. Fontaine, R. Grimes, A. Sidhaye, S. Yang, K. Moore, R. Levine, A. Yoganathan, Experimental analysis of fluid mechanical energy losses in aortic valve stenosis: Importance of pressure recovery, Ann. Biomed. Eng., 24 (1996) 685-694.
[95] J. Ross Jr, Afterload mismatch in aortic and mitral valve disease: Implications for surgical therapy, J. Am. Coll. Cardiol., 5 (1985) 811-826.
[96] O.C. Shavelle D, Aortic stenosis, In: Crawford MH, Dimarco JP, editors. Cardiology, 9 (2000) 9.1–9.10.
[97] R.O. Bonow, B. Carabello, A.C. de Leon, Jr., L.H. Edmunds, Jr., B.J. Fedderly, M.D. Freed, W.H. Gaasch, C.R. McKay, R.A. Nishimura, P.T. O'Gara, R.A. O'Rourke, S.H. Rahimtoola, J.L. Ritchie, M.D. Cheitlin, K.A. Eagle, T.J. Gardner, A. Garson, Jr., R.J. Gibbons, R.O. Russell, T.J. Ryan, S.C. Smith, Jr., Guidelines for the management of patients with valvular heart disease: executive summary. A report of the American College of Cardiology/American Heart Association Task Force on Practice Guidelines (Committee on Management of Patients with Valvular Heart Disease), Circulation, 98 (1998) 1949-1984.
[98] H. Baumgartner, T. Stefenelli, J. Niederberger, H. Schima, G. Maurer, "Overestimation" of catheter gradients by Doppler ultrasound in patients with aortic stenosis: a predictable manifestation of pressure recovery, J. Am. Coll. Cardiol., 33 (1999) 1655-1661.
[99] R. Gorlin, S.G. Gorlin, Hydraulic formula for calculation of the area of the stenotic mitral valve, other cardiac valves, and central circulatory shunts. I, Am. Heart J., 41 (1951) 1-29.
[100] D.F. Young, F.Y. Tsai, Flow characteristics in models of arterial stenoses. I. Steady flow, J. Biomech., 6 (1973) 395-410.
[101] D.F. Young, F.Y. Tsai, Flow characteristics in models of arterial stenoses. II. Unsteady flow, J. Biomech., 6 (1973) 547-559.
[102] C. Clark, Relation between pressure difference across the aortic valve and left ventricular outflow, Cardiovasc. Res., 12 (1978) 276-287.
[103] P. Ask, D. Loyd, B. Wranne, Regurgitant flow through heart valves: A hydraulic model applicable to ultrasound Doppler measurements, Med. Biol. Eng. Comput., 24 (1986) 643-646.
[104] S.A. Slørdahl, J.E. Solbakken, H. Piene, B.A.J. Angelsen, O. Rossvoll, S.O. Samstad, Quantification of aortic regurgitation by Doppler echocardiography: a new method evaluated in pigs, Med. Biol. Eng. Comput., 28 (1990) 300-305.

[105] J. Bermejo, J.C. Antoranz, I.G. Burwash, J.L. Alvarez, M. Moreno, M.A. Garcia-Fernandez, C.M. Otto, In-vivo analysis of the instantaneous transvalvular pressure difference-flow relationship in aortic valve stenosis: implications of unsteady fluid-dynamics for the clinical assessment of disease severity, J. Heart Valve Dis., 11 (2002) 557-566.
[106] D. Garcia, P. Pibarot, L.G. Durand, Analytical modeling of the instantaneous pressure gradient across the aortic valve, J. Biomech., 38 (2005) 1303-1311.
[107] D.S. Miller, Internal flow systems, Cranfield : BHRA (Information Services), 1990.
[108] P.M. Gerhart, Fundamentals of fluid mechanics, 2nd ed., Reading, Mass. : Addison-Wesley Pub. Co., 1992.
[109] H. Schlichting, Boundary layer theory, 4th ed., McGraw Hill: New York, 1960.
[110] Y. Fung, . Biomechanics: Circulation, 2nd ed., Springer-Verlag, New York, 1998.
[111] P.B. Dobrin, Poststenotic dilatation, Surg. Gynecol. Obstet., 172 (1991) 503-508.
[112] T.N.E.G. Adi Ben-Israel, Generalized Inverses: Theory and Applications, 2 ed., Springer, 2003.
[113] H. Baumgartner, Low-Flow, Low-Gradient Aortic Stenosis With Preserved Ejection FractionStill a Challenging Condition□, J. Am. Coll. Cardiol., 60 (2012) 1268-1270.
[114] S.R. Cannon, K.L. Richards, M. Crawford, Hydraulic estimation of stenotic orifice area: a correction of the Gorlin formula, Circulation, 71 (1985) 1170-1178.
[115] S.K. Shanmugavelayudam, D.A. Rubenstein, W. Yin, Effect of geometrical assumptions on numerical modeling of coronary blood flow under normal and disease conditions, J. Biomech. Eng., 132 (2010) 061004.
[116] X. He, D.N. Ku, Pulsatile flow in the human left coronary artery bifurcation: average conditions, J. Biomech. Eng., 118 (1996) 74-82.
[117] V.A. Nosovitsky, O.J. Ilegbusi, J. Jiang, P.H. Stone, C.L. Feldman, Effects of curvature and stenosis-like narrowing on wall shear stress in a coronary artery model with phasic flow, Comput. Biomed. Res., 30 (1997) 61-82.
[118] S. Smith, S. Austin, G.D. Wesson, C.A. Moore, Calculation of wall shear stress in left coronary artery bifurcation for pulsatile flow using two-dimensional computational fluid dynamics, Conf Proc IEEE Eng Med Biol Soc, 1 (2006) 871-874.
[119] Y. Qiu, J.M. Tarbell, Numerical simulation of pulsatile flow in a compliant curved tube model of a coronary artery, J. Biomech. Eng., 122 (2000) 77-85.
[120] T. Frauenfelder, E. Boutsianis, T. Schertler, L. Husmann, S. Leschka, D. Poulikakos, B. Marincek, H. Alkadhi, In-vivo flow simulation in coronary arteries based on computed tomography datasets: feasibility and initial results, Eur. Radiol., 17 (2007) 1291-1300.
[121] A.K. Politis, G.P. Stavropoulos, M.N. Christolis, F.G. Panagopoulos, N.S. Vlachos, N.C. Markatos, Numerical modeling of simulated blood flow in idealized composite arterial coronary grafts: steady state simulations, J. Biomech., 40 (2007) 1125-1136.
[122] E. Gaillard, D. Garcia, L. Kadem, P. Pibarot, L.G. Durand, In vitro investigation of the impact of aortic valve stenosis severity on left coronary artery flow, J. Biomech. Eng., 132 (2010) 044502.
[123] T.N. James, Pathology of small coronary arteries, Am. J. Cardiol., 20 (1967) 679-691.
[124] A.P. Burke, A. Farb, A. Tang, J. Smialek, R. Virmani, Fibromuscular dysplasia of small coronary arteries and fibrosis in the basilar ventricular septum in mitral valve prolapse, Am. Heart J., 134 (1997) 282-291.
[125] A. Nemes, T. Forster, N. Gruber, M. Csanady, Coronary flow velocity reserve and indices describing aortic distensibility in patients after coronary angiography, Int. J. Cardiol., 96 (2004) 29-33.
[126] A. Nemes, T. Forster, C. Lengyel, M. Csanady, Reduced aortic distensibility and coronary flow velocity reserve in diabetes mellitus patients with a negative coronary angiogram, Can. J. Cardiol., 23 (2007) 445-450.
[127] N. Funabashi, Y. Kobayashi, M. Perlroth, G.D. Rubin, Coronary artery: quantitative evaluation of normal diameter determined with electron-beam CT compared with cine coronary angiography initial experience, Radiology, 226 (2003) 263-271.
[128] W.G.W. Achilles J. Pappano, Cardiovascular Physiology: Mosby Physiology Monograph Series, 10 ed., Elsevier Health Sciences, 2012.
[129] A.P. Yoganathan, Z. He, S. Casey Jones, Fluid mechanics of heart valves, Annu. Rev. Biomed. Eng., 6 (2004) 331-362.
[130] M. Higashidate, K. Tamiya, T. Beppu, Y. Imai, Regulation of the aortic valve opening. In vivo dynamic measurement of aortic valve orifice area, J. Thorac. Cardiovasc. Surg., 110 (1995) 496-503.
[131] F. Robicsek, M.J. Thubrikar, J.W. Cook, B. Fowler, The congenitally bicuspid aortic valve: how does it function? Why does it fail?, Ann. Thorac. Surg., 77 (2004) 177-185.
[132] M. Thubrikar, B.A. Carabello, J. Aouad, S.P. Nolan, Interpretation of aortic root angiography in dogs and in humans, Cardiovasc. Res., 16 (1982) 16-21.

[133] D.H. Mowat, N.E. Haites, J.M. Rawles, Aortic blood velocity measurement in healthy adults using a simple ultrasound technique, Cardiovasc. Res., 17 (1983) 75-80.
[134] Z.D. Zhang, M. Svendsen, J.S. Choy, A.K. Sinha, Y. Huo, K. Yoshida, S. Molloi, G.S. Kassab, New method to measure coronary velocity and coronary flow reserve, Am. J. Physiol. Heart Circ. Physiol., 301 (2011) H21-28.
[135] J.W. Wragg, S. Durant, H.M. McGettrick, K.M. Sample, S. Egginton, R. Bicknell, Shear stress regulated gene expression and angiogenesis in vascular endothelium, Microcirculation, 21 (2014) 290-300.
[136] K.S. Cunningham, A.I. Gotlieb, The role of shear stress in the pathogenesis of atherosclerosis, Lab. Invest., 85 (2005) 9-23.
[137] A.M. Malek, S.L. Alper, S. Izumo, Hemodynamic shear stress and its role in atherosclerosis, JAMA, 282 (1999) 2035-2042.
[138] F. Gijsen, A. van der Giessen, A. van der Steen, J. Wentzel, Shear stress and advanced atherosclerosis in human coronary arteries, J. Biomech., 46 (2013) 240-247.
[139] D. Garcia, P.G. Camici, L.G. Durand, K. Rajappan, E. Gaillard, O.E. Rimoldi, P. Pibarot, Impairment of coronary flow reserve in aortic stenosis, J. Appl. Physiol., 106 (2009) 113-121.
[140] N. Ahmadi, V. Nabavi, F. Hajsadeghi, F. Flores, S. Azmoon, H. Ismaeel, D. Shavelle, S.S. Mao, R. Ebrahimi, M.J. Budoff, Impaired aortic distensibility measured by computed tomography is associated with the severity of coronary artery disease, Int. J. Cardiovasc. Imaging, 27 (2011) 459-469.
[141] J.L. Cavalcante, J.A.C. Lima, A. Redheuil, M.H. Al-Mallah, Aortic StiffnessCurrent Understanding and Future Directions, J. Am. Coll. Cardiol., 57 (2011) 1511-1522.
[142] S. Oberoi, U.J. Schoepf, M. Meyer, T. Henzler, G.W. Rowe, P. Costello, J.W. Nance, Progression of Arterial Stiffness and Coronary Atherosclerosis: Longitudinal Evaluation by Cardiac CT, Am. J. Roentgenol., 200 (2013) 798-804.
[143] M.D. de Tullio, L. Afferrante, G. Demelio, G. Pascazio, R. Verzicco, Fluid-structure interaction of deformable aortic prostheses with a bileaflet mechanical valve, J. Biomech., 44 (2011) 1684-1690.
[144] A. Kirpalani, H. Park, J. Butany, K.W. Johnston, M. Ojha, Velocity and wall shear stress patterns in the human right coronary artery, J. Biomech. Eng., 121 (1999) 370-375.
[145] J.G. Myers, J.A. Moore, M. Ojha, K.W. Johnston, C.R. Ethier, Factors influencing blood flow patterns in the human right coronary artery, Ann. Biomed. Eng., 29 (2001) 109-120.
[146] J.F. Verhey, C. Bara, Influence on fluid dynamics of coronary artery outlet angle variation in artificial aortic root prosthesis, Biomedical engineering online, 7 (2008) 9.
[147] A.M. Nixon, M. Gunel, B.E. Sumpio, The critical role of hemodynamics in the development of cerebral vascular disease, J. Neurosurg., 112 (2010) 1240-1253.
[148] E. Cecchi, C. Giglioli, S. Valente, C. Lazzeri, G.F. Gensini, R. Abbate, L. Mannini, Role of hemodynamic shear stress in cardiovascular disease, Atherosclerosis, 214 (2011) 249-256.
[149] N.B. Wood, S.Z. Zhao, A. Zambanini, M. Jackson, W. Gedroyc, S.A. Thom, A.D. Hughes, X.Y. Xu, Curvature and tortuosity of the superficial femoral artery: a possible risk factor for peripheral arterial disease, Journal of applied physiology (Bethesda, Md. : 1985), 101 (2006) 1412-1418.
[150] A.S. Go, D. Mozaffarian, V.L. Roger, E.J. Benjamin, J.D. Berry, M.J. Blaha, S. Dai, E.S. Ford, C.S. Fox, S. Franco, H.J. Fullerton, C. Gillespie, S.M. Hailpern, J.A. Heit, V.J. Howard, M.D. Huffman, S.E. Judd, B.M. Kissela, S.J. Kittner, D.T. Lackland, J.H. Lichtman, L.D. Lisabeth, R.H. Mackey, D.J. Magid, G.M. Marcus, A. Marelli, D.B. Matchar, D.K. McGuire, E.R. Mohler, 3rd, C.S. Moy, M.E. Mussolino, R.W. Neumar, G. Nichol, D.K. Pandey, N.P. Paynter, M.J. Reeves, P.D. Sorlie, J. Stein, A. Towfighi, T.N. Turan, S.S. Virani, N.D. Wong, D. Woo, M.B. Turner, Heart disease and stroke statistics--2014 update: a report from the American Heart Association, Circulation, 129 (2014) e28-e292.
[151] Z. Sun, Y. Cao, Multislice CT angiography assessment of left coronary artery: correlation between bifurcation angle and dimensions and development of coronary artery disease, Eur. J. Radiol., 79 (2011) e90-95.
[152] S.K. Sharma, J. Sweeny, A.S. Kini, Coronary bifurcation lesions: a current update, Cardiol. Clin., 28 (2010) 55-70.
[153] B.K. Koo, K. Waseda, H.J. Kang, H.S. Kim, C.W. Nam, S.H. Hur, J.S. Kim, D. Choi, Y. Jang, J.Y. Hahn, H.C. Gwon, M.H. Yoon, S.J. Tahk, W.Y. Chung, Y.S. Cho, D.J. Choi, T. Hasegawa, T. Kataoka, S.J. Oh, Y. Honda, P.J. Fitzgerald, W.F. Fearon, Anatomic and functional evaluation of bifurcation lesions undergoing percutaneous coronary intervention, Circulation. Cardiovascular interventions, 3 (2010) 113-119.
[154] P.A. Tonino, B. De Bruyne, N.H. Pijls, U. Siebert, F. Ikeno, M. van' t Veer, V. Klauss, G. Manoharan, T. Engstrom, K.G. Oldroyd, P.N. Ver Lee, P.A. MacCarthy, W.F. Fearon, Fractional flow reserve versus angiography for guiding percutaneous coronary intervention, N. Engl. J. Med., 360 (2009) 213-224.

[155] N.H. Pijls, B. De Bruyne, G.J. Bech, F. Liistro, G.R. Heyndrickx, H.J. Bonnier, J.J. Koolen, Coronary pressure measurement to assess the hemodynamic significance of serial stenoses within one coronary artery: validation in humans, Circulation, 102 (2000) 2371-2377.
[156] S.J. Park, J.M. Ahn, N.H. Pijls, B. De Bruyne, E.B. Shim, Y.T. Kim, S.J. Kang, H. Song, J.Y. Lee, W.J. Kim, D.W. Park, S.W. Lee, Y.H. Kim, C.W. Lee, S.W. Park, Validation of functional state of coronary tandem lesions using computational flow dynamics, Am. J. Cardiol., 110 (2012) 1578-1584.
[157] P. Lanzer, Catheter-based cardiovascular interventions a knowledge-based approach, in, Springer, Berlin; New York, 2013.
[158] T. Chaichana, Z. Sun, J. Jewkes, Investigation of the haemodynamic environment of bifurcation plaques within the left coronary artery in realistic patient models based on CT images, Australas. Phys. Eng. Sci. Med., 35 (2012) 231-236.
[159] T. Chaichana, Z. Sun, J. Jewkes, Impact of plaques in the left coronary artery on wall shear stress and pressure gradient in coronary side branches, Comput Methods Biomech Biomed Engin, 17 (2014) 108-118.
[160] A.S. Yong, D. Daniels, B. De Bruyne, H.S. Kim, F. Ikeno, J. Lyons, N.H. Pijls, W.F. Fearon, Fractional flow reserve assessment of left main stenosis in the presence of downstream coronary stenoses, Circulation. Cardiovascular interventions, 6 (2013) 161-165.
[161] M.B. Iqbal, N. Shah, M. Khan, W. Wallis, Reduction in myocardial perfusion territory and its effect on the physiological severity of a coronary stenosis, Circulation. Cardiovascular interventions, 3 (2010) 89-90.
[162] D. Dash, Stenting of left main coronary artery stenosis: A to Z, Heart Asia, 5 (2013) 18-27.
[163] J. Fajadet, A. Chieffo, Current management of left main coronary artery disease, 2012.
[164] S.-J. Park, S.-J. Kang, J.-M. Ahn, E.B. Shim, Y.-T. Kim, S.-C. Yun, H. Song, J.-Y. Lee, W.-J. Kim, D.-W. Park, S.-W. Lee, Y.-H. Kim, C.W. Lee, G.S. Mintz, S.-W. Park, Visual-Functional Mismatch Between Coronary Angiography and Fractional Flow Reserve, JACC: Cardiovascular Interventions, 5 (2012) 1029-1036.
[165] K.L. Gould, R. Kirkeeide, N.P. Johnson, Coronary branch steal: experimental validation and clinical implications of interacting stenosis in branching coronary arteries, Circulation. Cardiovascular imaging, 3 (2010) 701-709.
[166] M.J. Kern, When does a left anterior descending stenosis alter flow across a left main segment?: Interpreting left main fractional flow reserve with downstream obstruction, Circulation. Cardiovascular interventions, 6 (2013) 128-130.
[167] C.S. Louis Thériault, Sabrina Browarski, The Canadian Heart Health Strategy: Risk Factors and Future Cost Implications in: Proc. The Conference Board of Canada, Ottawa, January 2010.
[168] C.A. Taylor, T.J. Hughes, C.K. Zarins, Finite element modeling of three-dimensional pulsatile flow in the abdominal aorta: relevance to atherosclerosis, Ann. Biomed. Eng., 26 (1998) 975-987.
[169] K. Perktold, M. Resch, R.O. Peter, Three-dimensional numerical analysis of pulsatile flow and wall shear stress in the carotid artery bifurcation, J. Biomech., 24 (1991) 409-420.
[170] K.M. Tse, P. Chiu, H.P. Lee, P. Ho, Investigation of hemodynamics in the development of dissecting aneurysm within patient-specific dissecting aneurismal aortas using computational fluid dynamics (CFD) simulations, J. Biomech., 44 (2011) 827-836.
[171] K. Khanafer, R. Berguer, Fluid-structure interaction analysis of turbulent pulsatile flow within a layered aortic wall as related to aortic dissection, J. Biomech., 42 (2009) 2642-2648.
[172] A. Borghi, N.B. Wood, R.H. Mohiaddin, X.Y. Xu, Fluid–solid interaction simulation of flow and stress pattern in thoracoabdominal aneurysms: A patient-specific study, Journal of Fluids and Structures, 24 (2008) 270-280.
[173] D. Juang, A.C. Braverman, K. Eagle, Cardiology patient pages. Aortic dissection, Circulation, 118 (2008) e507-510.
[174] M.B. Lewin, C.M. Otto, The bicuspid aortic valve: adverse outcomes from infancy to old age, Circulation, 111 (2005) 832-834.
[175] T.M. Tadros, M.D. Klein, O.M. Shapira, Ascending aortic dilatation associated with bicuspid aortic valve: pathophysiology, molecular biology, and clinical implications, Circulation, 119 (2009) 880-890.
[176] N.M. Pahlevan, F. Amlani, M. Hossein Gorji, F. Hussain, M. Gharib, A physiologically relevant, simple outflow boundary model for truncated vasculature, Ann. Biomed. Eng., 39 (2011) 1470-1481.
[177] C.G. Caro, The Mechanics of the circulation, Oxford University Press, Oxford; New York, 1978.
[178] S. Berger, L. Talbot, L. Yao, Flow in curved pipes, Annual review of fluid mechanics, 15 (1983) 461-512.
[179] A.A. Johnson, T.E. Tezduyar, Mesh update strategies in parallel finite element computations of flow problems with moving boundaries and interfaces, Computer Methods in Applied Mechanics and Engineering, 119 (1994) 73-94.

Appendix A: Arbitrary Lagrangian Eulerian method (ALE)

The Arbitrary Lagrangian Eulerian (ALE) method, developed by Hirt et al [33], is the best suited technique in computational analysis of problem with moving interface or experiencing large deformations. As in the Eulerian description of the fluid flow the mesh is fixed and consequently is unable to capture the emotion the boundary, the main motivation for the development of this technique was to be used for description of the fluid flow associated with moving boundary. Therefore, ALE is an appropriate approach for FSI problems. In this appendix, the impact of using ALE reference frame on the equilibrium equations of the fluid flow is briefly described.

For identification of the points in continuum, ALE method employs three distinct reference systems: spatial reference system (SRS), material reference system (MRS) and a computational reference system (CRS). The SRS is a fixed reference system which is used for Eulerian description, the MRS is connected to the material and moves with it according to Lagrangian approach and the CRS moves arbitrary according to some prescribed displacement. In the ALE approach the fluid domain is discretized in the CRS while the physical quantities in the governing equations of the solid and fluid domains are defined in MRS and SRS, respectively. Therefore, in order to perform finite element formulation of the fluid domain in CRS, it is essential to couple the quantities defined in CRS to those in SRS [34, 179].

In Figure A. 1, the motion of the material point M with respect to reference systems CRS and SRS is presented. Over an infinitesimally small time step Δt , this point has moved which is dependent on the position and time can be expressed as:

$$\begin{aligned}\frac{D\phi(x,t)}{Dt} &= \lim_{\Delta t\to 0}\frac{1}{\Delta t}[\phi(\boldsymbol{x}(t+\Delta t),t+\Delta t)-\phi(\boldsymbol{x},t)]\\ &= \lim_{\Delta t\to 0}\frac{1}{\Delta t}[\phi(\boldsymbol{x}(t+\Delta t),t+\Delta t)-\phi(\boldsymbol{x},t+\Delta t)-\phi(\boldsymbol{x},t+\Delta t)-\phi(\boldsymbol{x},t)]\\ &= \lim_{\Delta t\to 0}\frac{1}{\Delta t}[d\boldsymbol{x}.\nabla\phi]+\lim_{\Delta t\to 0}\frac{1}{\Delta t}[\phi(\boldsymbol{x},t+\Delta t)-\phi(\boldsymbol{x},t)]\\ &= \boldsymbol{v}.\nabla\phi+\frac{\partial\phi}{\partial t}\end{aligned} \qquad \text{(A. 1)}$$

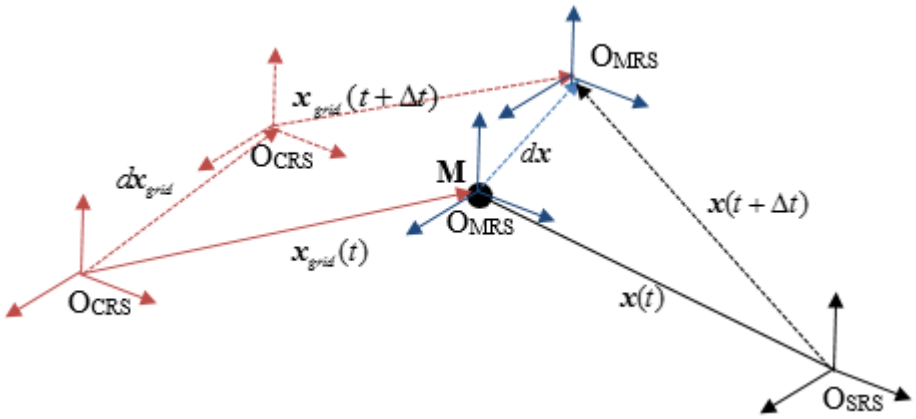

Figure A. 1: Schematic drawing of motion of material point M in coordinate systems SRS, MRS

where v denotes the velocity of the material point and ∇ the gradient operator with respect to the SRS. The first term in equation (A. 1), is the convective term corresponding to the changes due to motion of the material while the second term is an inertia term, which incorporates the change of variable depending only on time. The above equation is written in SRS which is fixed according to Eulerian approach. In order to express it in CRS which corresponds to ALE method, it should be taken into account that the CRS is also moving with respect to SRS during the time step Δt, Figure A. 1. Therefore, the position of M measured in CRS at time $t+\Delta t$ is defined as:

$$\boldsymbol{x}_{grid}(t+\Delta t) = \boldsymbol{x}_{grid}(t) + d\boldsymbol{x} - d\boldsymbol{x}_{grid} \tag{A. 2}$$

Hence, replacing $\boldsymbol{x}(t)$ by $\boldsymbol{x}_{grid}(t)$ and $d\boldsymbol{x}$ by $d\boldsymbol{x} - d\boldsymbol{x}_{grid}$ in equation (A. 2) gives:

$$\frac{D\phi(x,t)}{Dt} = (\boldsymbol{v} - \boldsymbol{v}_{grid}).\nabla\phi + \frac{\partial\phi}{\partial t}|_{x_{grid}} \tag{A. 3}$$

where $\boldsymbol{v}_{grid}$ refers to the grid velocity and the inertial term is now defined in grid point $\boldsymbol{x}_{grid}(t)$ .Therefore, the ALE formulation is equivalent to Eulerian if $\boldsymbol{v}_{grid} = 0$ and the Lagranigan formulation can be easily retained form ALE equations, if the gird moves with the same velocity as the material, i.e., $\boldsymbol{v}_{grid} = \boldsymbol{v}$.

Appendix B: Nomenclature

A_d	Flow cross sectional area downstream of the stenosis, cm^2
A_u	Flow cross sectional area upstream of the stenosis, cm^2
a	Vessel radius, cm
C	Vessel compliance, $cm/barye$
$\boldsymbol{C}$	Stiffness tensor of the vessel wall material, $Barye$
$\boldsymbol{D}_f$	Rate-of-deformation tensor in the fluid domain, s^{-1}
E	Young's modulus of the vessel, $Barye$
EOA	Flow effective orifice area, cm^2
$\vec{F}$	Body and surface force vector, $dyne$
$\boldsymbol{F}$	Material deformation tensor at the current configuration
$\boldsymbol{f}_f$	Body force applied on the fluid domain, $dyne$
$\boldsymbol{f}_s$	Body force applied on the solid domain, $dyne$
G	Shear modulus of the solid domain, $Barye$
$g(\frac{A_d}{EOA})$	Function of the areas ratio, dimensionless
h	Vessel thickness, cm
I	Second-order unit tensor, dimensionless
k_c	Empirical constant in the convective pressure loss term, dimensionless
k_p	Empirical constant in the pressure loss term due to the vessel compliance, $Barye$
k_v	Empirical constant in the viscous pressure loss, dimensionless
L_{23}	Distance between two referenced positions downstream and upstream of the stenosis, cm
$\vec{n}$	Outward pointing normal unit vector to the body surface, dimensionless
p	Blood flow pressure, $Barye$

p_f Hydrostatic pressure in the fluid domain, $Barye$

p_s Hydrostatic pressure in the solid domain, $Barye$

Q Volume flow rate, cm^3/s

t Time, s

u Blood flow velocity, cm/s

$\boldsymbol{v}_f$ Fluid domain velocity vector, cm/s

$\boldsymbol{v}_s$ Solid domain velocity vector, cm/s

$\boldsymbol{v}_{grid}$ Velocity vector of the moving fluid grid, cm/s

W_v Space of the acceptable solutions for the velocity vector

W_o Trial functions space

λ Parameter defined as $\frac{L_{23}}{A_d}+\int_{x_1}^{x_2}\frac{dx}{A}$, cm^{-1}

ζ Empirical constant, dimensionless

ρ Blood density, g/cm^3

ρ_f Fluid domain density, g/cm^3

ρ_s Solid domain density, g/cm^3

μ Dynamic viscosity of blood, $g/cm\,s$

η Dynamic viscosity of the fluid domain, $g/cm\,s$

υ Kinematic viscosity of blood, cm^2/s

ω Heart frequency, Hz

τ Vessel wall shear stress, $Barye$

Δp Pressure gradient across stenosis, $Barye$

Δp_C Convective component of the pressure gradient across stenosis, $Barye$

Δp_{Co} Pressure gradient component due to the vessel distensibility, $Barye$

Δp_L Pressure gradient component due to the local inertia, $Barye$

Δp_V	Viscous component of the pressure gradient across stenosis, *Barye*
σ_{ij}	Cauchy stress tensor, *Barye*
Ω_f	Fluid domain
Ω_s	Solid domain
Ω	Entire computational domain
$\partial\Omega_s$	Fuid-Structure interface
∇	Gradient operator with respect to the current configuration
$\nabla_\circ$	Gradient operator with respect to the initial configuration